

A169971

3

FINAL REPORT

(Grant No. AFOSR-82-0238)

on

DTIC
ELECTE
JUL 24 1986
S D D

HOT ISOSTATIC PRESSING OF
CERAMIC POWDER COMPACTS

to

AIR FORCE OFFICE OF SCIENTIFIC RESEARCH

February 7, 1986

by

J. K. McCoy and A. J. Markworth

BATTELLE
Columbus Division
505 King Avenue
Columbus, Ohio 43201

AIR FORCE OFFICE OF SCIENTIFIC RESEARCH (AFOSR)
NOTICE OF TRANSMITTAL TO DTIC
This technical report has been reviewed and is
approved for public release ISW AFR 190-12.
Distribution is unlimited.
MATTHEW J. KERRER
Chief, Technical Information Division

 **Battelle**
Columbus Division
505 King Avenue
Columbus, Ohio 43201
Telephone (614) 424-6424
Telex 24-5454

February 13, 1986

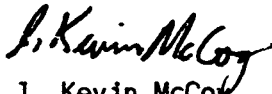
Major Joseph W. Hager, USAF
Program Manager
Electronic and Materials Sciences Directorate
AFOSR/NE
Bolling Air Force Base, DC 20332

Dear Major Hager:

AFOSR Contract 82-0238

Enclosed are sixteen (16) copies of the final report on the above-mentioned contract. If you have any questions regarding the report, please feel free to call me at 614-424-4050.

Sincerely,



J. Kevin McCoy
Research Scientist
Physical Metallurgy Section

JKM:taj

Encs. (16)

TABLE OF CONTENTS

	<u>Page</u>
I. INTRODUCTION	1
II. SUMMARY OF RESEARCH.	2
III. CONCLUSIONS.	6
IV. RECOMMENDED RESEARCH	7
V. PRESENTATIONS.	8
VI. PUBLICATIONS	9
APPENDIX A	
A RATIONAL METHOD FOR CALCULATING MECHANISM MAPS (reprint) . . .	A-1
APPENDIX B	
DILATOMETER TECHNIQUE FOR HOT ISOSTATIC PRESSING (reprint) . . .	B-1
APPENDIX C	
CONTINUOUS MONITORING OF VOLUMETRIC CHANGES IN CERAMIC POWDER COMPACTS DURING HOT ISOSTATIC PRESSING (reprint).	C-1
APPENDIX D	
INTERFACE-REACTION-CONTROLLED KINETICS IN THE HOT ISOSTATIC PRESSING OF SUBMICROMETER ALUMINA POWDER (reprint) . .	D-1
APPENDIX E	
DISCUSSION OF "PRACTICAL APPLICATIONS OF HOT-ISOSTATIC PRESSING DIAGRAMS: FOUR CASE STUDIES" (reprint)	E-1
APPENDIX F	
DENSIFICATION BY INTERFACE-REACTION CONTROLLED GRAIN-BOUNDARY DIFFUSION (preprint).	F-1
APPENDIX G	
COMPUTER SIMULATION OF EFFECTS OF THE PORE SIZE DISTRIBUTION ON THE KINETICS OF PRESSURE-ASSISTED FINAL-STAGE DENSIFICATION OF A POROUS SOLID (preprint)	G-1

UNCLASSIFIED

SECURITY CLASSIFICATION OF THIS PAGE (When Data Entered)

REPORT DOCUMENTATION PAGE		READ INSTRUCTIONS BEFORE COMPLETING FORM
1. REPORT NUMBER AFOSR-TR- 86-0348	2. GOVT ACCESSION NO.	3. RECIPIENT'S CATALOG NUMBER
4. TITLE (and Subtitle) Hot Isostatic Pressing of Ceramic Powder Compacts		5. TYPE OF REPORT & PERIOD COVERED 01 JUN 84- Final 31 DEC 85
7. AUTHOR(s) J. K. McCoy and A. J. Markworth		6. PERFORMING ORG. REPORT NUMBER
9. PERFORMING ORGANIZATION NAME AND ADDRESS Battelle Columbus Laboratories 505 King Avenue, Columbus, Ohio 43201		8. CONTRACT OR GRANT NUMBER(s) AFOSR- 82-0238
11. CONTROLLING OFFICE NAME AND ADDRESS Major Hager AFOSR/NE Bolling AFB DC 20332-6448		10. PROGRAM ELEMENT, PROJECT, TASK AREA & WORK UNIT NUMBERS 2306/A2
14. MONITORING AGENCY NAME & ADDRESS (if different from Controlling Office)		12. REPORT DATE January 15, 1986
		13. NUMBER OF PAGES
		15. SECURITY CLASS. (of this report) UNCLASSIFIED
		15a. DECLASSIFICATION/DOWNGRADING SCHEDULE
16. DISTRIBUTION STATEMENT (of this Report) unlimited, (statement "A" of AFR 80-44) Approved for public release; distribution unlimited.		
17. DISTRIBUTION STATEMENT (of the abstract entered in Block 20, if different from Report)		
18. SUPPLEMENTARY NOTES		
19. KEY WORDS (Continue on reverse side if necessary and identify by block number) Hot Isostatic Pressing, Alumina, solute diffusion, interface controlled		
20. ABSTRACT (Continue on reverse side if necessary and identify by block number) MICROSTRUCTURE The densification of aluminum oxide in hot isostatic pressing has been studied in detail. Methods for calculating maps of densification rate as function of temperature and applied pressure have been developed. A new mechanism, interface-reaction-controlled grain-boundary diffusion, has been found which describes the densification of high-purity, fine-grained (grain radius of 0.7 μm) aluminum oxide powder at temperatures up to 1423 K. Theoretical models have been developed for this mechanism.		

UNCLASSIFIED

FINAL REPORT
on
HOT ISOSTATIC PRESSING OF CERAMIC POWDER COMPACTS

(Grant No. AFOSR-82-0238)

to
AIR FORCE OFFICE OF SCIENTIFIC RESEARCH

by
J. K. McCoy and A. J. Markwortf

from
BATTELLE
Columbus Division

February 14, 1986

INTRODUCTION

This report contains a summary of research carried out under AFOSR contract No. 82-0238, "Hot Isostatic Pressing of Ceramic Powder Compacts", the period of performance of which was June 15, 1982 to January 15, 1986. The major results obtained under this program have been, or are currently being, published in the open literature. The pertinent reprints and preprints are included as appendices, and these contain complete descriptions of both methods and results. A brief summary of the research is presented in the next section, with references made to the detailed discussions in the appendices.

SUMMARY OF RESEARCH

The objective of this research was to investigate the potential of theoretical models for describing and predicting the densification behavior of ceramics in hot isostatic pressing (HIP). As a test material, we selected Reynolds RC-HP-DBM, a fine-grained, high-purity alumina powder. The kinetics of densification for this material were studied at temperatures of 1273 K to 1423 K and pressures of 34 MPa to 103 MPa. The primary novel feature of the experiments was that a dilatometer was used to obtain a continuous record of sample density. Use of the dilatometer provided a very detailed view of the kinetics of densification, and allowed us to critically evaluate theoretical models for densification.

At the outset of this work we expected that we would be performing a large number of simple hot isostatic pressing experiments and correlating them with a number of theories of densification. Accordingly, we developed a system of computer programs for the calculation of densification mechanism maps. These programs are self-contained and intended to be readily adapted to various densification mechanisms or even to different problems such as creep. The programs are also designed to be "portable", that is, able to be run readily on a variety of computer systems. It is expected that the programs would run on many computer systems with changes to only the few routines that form the interface with the plotter. A description of the algorithms used in the program is found in Appendix A.

Study of the densification maps for alumina indicated that, for applied gas pressures of up to 100 MPa and temperatures up to at least 1473 K, the dominant mechanism of densification would be grain-boundary diffusion for the material under study. Specifically, the predictions based on standard theories of densification were that transport of aluminum ions would be rate-limiting, that aluminum ions would move primarily by grain-boundary diffusion, and that charge compensation would occur primarily by diffusion of oxygen ions through the lattice.

Near the end of the first year of the project, development of the HIP dilatometer was completed. This offered us a choice of two experimental strategies: we could perform a large number of relatively inexpensive, uninstrumented HIP experiments, or we could perform a smaller number of more expensive experiments using the dilatometer to monitor changes in sample geometry, and keeping continuous records of temperature and applied pressure. A few tests made it clear that the latter choice was more effective due to the large volume of data which could be collected from a single experiment. In addition, when taking data with the dilatometer, we could study the effects of changing HIP conditions without considering sample-to-sample and run-to-run variations. A discussion of the principles of the dilatometer and the benefits of its use is found in Appendix B.

Methods of data analysis were developed for the dilatometer. The dilatometer measures the diameter of an encapsulated cylindrical sample, but the fractional density of the sample is desired. It was necessary to develop a model for geometrical changes in the sample and capsule occurring during densification and their effect on the measured diameter. The effects of densification, thermal expansion, and changes in the length-to-diameter ratio of the sample were included. Details of the data analysis are described in Appendix C.

As mentioned above, a HIP experiment using the dilatometer provides a great deal of information, while an ordinary HIP experiment gives only the initial and final density. In particular, the dilatometer provides a much clearer and more detailed description of the kinetics of HIP than is ordinarily available. To accommodate this new look at HIP, we found that it was more appropriate to consider theoretically calculated plots of density as a function of time than it was to use densification maps. Accordingly, we developed programs to solve the differential equation for densification. This approach is complementary to the use of maps: the maps provide qualitative information regarding changes of densification rate in response to temperature and pressure, while integration of the densification rate gives the details of the density history resulting from a specific HIP treatment. The programs

for calculating density histories were designed so that experimental records of pressure and temperature could be used with theoretical models of densification. As a result, we could readily plot and compare the experimental and theoretical densification histories. This provided a very graphic means for evaluating the theory.

The most instructive of these calculations was for experiments in which we changed the pressure during densification. In standard theories of densification by diffusion, the densification rate varies linearly with the applied gas pressure. As discussed in Appendix D, we found that our data could not be reconciled with such a model. However, the data were consistent with a model in which the densification rate varies approximately with the square of the applied gas pressure. The densification maps calculated early in the project were incomplete in that no mechanism with such a pressure dependence had been included.

This discovery led us to review the theoretical basis of models for a wide variety of densification mechanisms. As part of this review, we uncovered an error in a published model of densification. A description of the correction of the error is found in Appendix E.

The second-power dependence of the densification rate on applied pressure forms an unusual intermediate between the models of densification by diffusion, which predict a first-power dependence, and models of densification by dislocation motion, which predict third- or higher-power dependence. We found, however, that interface-reaction-controlled grain-boundary diffusion had been proposed as a mechanism for creep deformation, and that this mechanism resulted in a second-power dependence of creep rate on applied stress. By changing the grain geometry, we were able to adapt the model to describe densification rather than creep. Two versions of the model were developed: one with impinging spherical particles for the initial stage of densification and one with isolated spherical pores for the final stage. A complete development of the model and comparisons of experimental and theoretical results are found in Appendix F.

The model of densification by interface-reaction-controlled grain-boundary diffusion was found to fit the data well for fractional

densities up to 0.9, but the densification rate was overestimated at higher densities. Since the final stage of densification is important in determining the mechanical properties of high-performance ceramics, this situation was thought to deserve closer study. We found that both our model and standard models of densification by diffusion predict that densification will proceed rapidly to completion. This is in marked contrast to our experimental data showing a gradual decrease in densification rate and to the common observation that it is often difficult to achieve full density.

One possible reason for the discrepancy between theory and experiment is that standard theories assume a single pore size. Since it is assumed that all the pores start at the same size at the beginning the final stage of densification, they all remain the same size, shrink together, and finally vanish simultaneously. This is hardly a plausible picture. A more reasonable approach is to assume that there is a distribution of pore sizes, with small pores vanishing rather quickly while large pores are more persistent. Such a description of final-stage densification is given in Appendix G. It is found that even a distribution of pore sizes with a modest variance can produce a much more gradual approach toward full density.

CONCLUSIONS

The following conclusions may be drawn from this research:

The use of a dilatometer can provide a detailed record of density during a HIP experiment. This amount of information obtained in this way is so much larger than that produced from an ordinary HIP experiment that it is possible to reduce greatly the number of experiments and total cost to identify densification mechanisms or characterize densification behavior.

While densification maps provide a good summary of a large body of densification data, they are less useful for analysis of experimental kinetic data. With data from a dilatometer, it is more appropriate to compare plots of the recorded density history with a theoretically calculated density history.

It has been shown that models using a single particle size can provide an adequate description of densification at fractional densities up to 0.9. At higher densities, models using single pore and particle sizes predict excessive densification rates. A detailed description of the microstructure, especially of the pore size distribution, is necessary for adequate predictions of final-stage densification kinetics.

RECOMMENDED RESEARCH

As mentioned above, models of densification which use a single grain size and pore size do not provide an adequate description of densification at fractional densities above 0.9. Unfortunately, the mechanical properties of high-performance ceramics depend sensitively on density in this range. In order to improve the predictive capabilities of theoretical models to the point at which they can be used effectively to reduce the cost of developing new ceramic materials, it is recommended that additional study of the final stage of densification be performed. Since it has been found that the final stage of densification is significantly affected by the distribution of pore sizes, it is appropriate to perform detailed quantitative metallography to determine the pore size distribution functions and to attempt to relate these functions to powder properties such as particle size distribution and degree of agglomeration.

PRESENTATIONS

The following presentations have been given as part of work on this project:

J. K. McCoy, "A Coherent Method for Calculating Mechanism Maps", Basic Sciences Division of the American Ceramic Society, Fall Meeting, Columbus, Ohio, October 30–November 2, 1983.

R. R. Wills and J. K. McCoy, "Hot Isostatic Pressing Densification Maps", Basic Sciences Division of the American Ceramic Society, Fall Meeting, Columbus, Ohio, October 30–November 2, 1983.

R. R. Wills and J. K. McCoy, "Hot Isostatic Pressing of Al_2O_3 Powder: Theory vs. Experiment", Basic Sciences Division of the American Ceramic Society, Spring Meeting, Pittsburgh, Pennsylvania, April 29–May 3, 1984.

R. R. Wills, L. E. Muttart, and J. K. McCoy, "Continuous Monitoring of Densification and Phase Changes During Hot Isostatic Pressing", Basic Sciences Division of the American Ceramic Society, Fall Meeting, San Francisco, California, October 28–31, 1984.

J. K. McCoy and R. R. Wills, "Dilatometer Technique for Hot Isostatic Pressing", Ninth Annual Conference on Composites and Advanced Materials, Cocoa Beach, Florida, January 20–23, 1985.

R. R. Wills and J. K. McCoy, "Interface-Controlled Kinetics in the Hot Isostatic Pressing of Alumina Powder", American Ceramic Society, 87th Annual Meeting, Cincinnati, Ohio, May 5–9, 1985.

PUBLICATIONS

The following papers have been written as part of work on this project. Texts of these papers are found in the appendices.

J. K. McCoy, "A Rational Method for Calculating Mechanism Maps", *Scripta Metallurgica*, vol. 17, pp. 563-568 (1983).

J. K. McCoy and R. R. Wills, "Dilatometer Technique for Hot Isostatic Pressing", *Ceramic Engineering and Science Proceedings*, vol. 6, pp. 1146-1150 (1985).

J. K. McCoy, L. E. Muttart, and R. R. Wills, "Continuous Monitoring of Volumetric Changes in Ceramic Powder Compacts During Hot Isostatic Pressing", *American Ceramic Society Bulletin*, vol. 64, pp. 1240-1244 (1985).

R. R. Wills and J. K. McCoy, "Interface-Reaction-Controlled Kinetics in the Hot Isostatic Pressing of Submicrometer Alumina Powder", *Journal of the American Ceramic Society*, vol. 68, pp. C95-C96 (1985)

J. K. McCoy, "Discussion of 'Practical Applications of Hot-Isostatic Pressing Diagrams: Four Case Studies'", *Metallurgical Transactions*, vol. 16A, pp. 1903-1904 (1985).

J. K. McCoy and R. R. Wills, "Densification by Interface-Reaction Controlled Grain-Boundary Diffusion", submitted to *Acta Metallurgica*.

A. J. Markworth and J. K. McCoy, "Computer Simulation of Effects of the Pore Size Distribution on the Kinetics of Pressure-Assisted Final-Stage Densification of a Porous Solid", submitted to *Materials Science and Engineering*.

APPENDIX A

A RATIONAL METHOD FOR CALCULATING
MECHANISM MAPS

Reprinted from

Scripta Metallurgica, vol. 17, pp. 563-568 (1983)

A RATION' METHOD FOR CALCULATING MECHANISM MAPS

J. Kevin McCoy
Battelle, Columbus Laboratories
Columbus, Ohio 43201

(Received February /, 1983)

INTRODUCTION

Since the introduction of mechanism maps by Weertman and Weertman (1) and their subsequent development by Ashby (2), there has been a great and growing interest in the construction and use of such maps. They have been used to describe the kinetics of creep (2,3), hot pressing (4), sintering (5), and fracture (6). In addition, potential-pH diagrams (7), which are constructed in a similar way, have been used to describe the corrosion behavior of a large number of materials. The discussion in this paper is couched in terms of deformation modeling, but the methods may be applied readily to other problems.

A variety of algorithms have been used in the construction of these maps, but for the present discussion, it will suffice to classify them as "linear" or "point-by-point". The linear methods rely on the use of straight lines to represent the contours and boundaries in the map, with, in some cases, the use of a change of variables to produce the necessary linearization (8). The point-by-point methods, on the other hand, avoid the assumption of linearity by making an exhaustive scan of the whole map. The point-by-point approach is often thought of as being inefficient because past programs required the evaluation of rates at a large number of points, while linear methods involve the treatment of a linear system at relatively few points. For metallurgical processes, however, it is not clear that linearization is always possible, so it is natural to choose the more general point-by-point approach.

Unfortunately, the point-by-point programs which were available to us were less than inspiring. They did not meet modern standards of modularity, documentation, or user convenience, and they appeared to be slipshod in their use of data. A review of the literature further suggested that no study had been made of the methods necessary for systematic calculation and plotting of mechanism maps. Accordingly, we set out to develop methods which make careful use of all data and which could be used to plot maps in essentially final form. Besides the intended advantage of producing finished maps, we also found that our algorithm is surprisingly efficient and requires far fewer points than other point-by-point methods.

Calculation of Boundaries

Let us state the problem of the construction of a mechanism map in abstract terms. We have n functions f_i , $i=1, n$, each of which is dependent on two variables. At any point (x,y) , the value $f_i(x,y)$ is the rate of deformation via the i th mechanism. The map describes a rectangular region $x_{\min} \leq x \leq x_{\max}$, $y_{\min} \leq y \leq y_{\max}$. The first step in the construction of the map is to divide the map into one or more regions where $f_i(x,y) > f_j(x,y)$ for all $j \neq i$. Such a region will be called a region of dominance of mechanism i . The second step is to find a set of contour lines for each of the regions. The third step is to plot the boundaries of the regions and the contours in a smooth and efficient manner. In the remainder of this paper we will discuss each of these three steps in sequence. Finally, we will present examples which illustrate the efficiency of the algorithm.

To make the problem tractable, a regular grid is superimposed on the map, dividing the area of the map into rectangles. The density of the grid will vary from one map to another, based on the complexity of the map, the desired level of smoothness of the curves, and the need for computational speed.

In calculating the map, each rectangle is treated separately, and the portion of any boundary or contour which lies within the rectangle is represented by a line segment. The

general efficiency of the algorithm may be improved by careful storage of the data. It is desirable to evaluate the functions f_i only once at each grid point and to save the results of the analysis of individual sides of a rectangle for subsequent use in analysis of adjacent rectangles.

Since each rectangle is treated separately, let us consider the determination of the boundaries of the regions of dominance which fall within one rectangle. We will first discuss the topology of the boundaries, then investigate how the topology and positions of the boundaries may be calculated.

Figure 1 shows four topologically distinct arrangements of boundaries between regions of dominance in one rectangle of the map. We have found that real mechanism maps very rarely require more complex topologies.

In calculating the positions of the boundaries, no data are used except the values of the functions f_i at the four corners of the rectangle. All boundaries within the rectangle are assumed to be line segments.

Rather than analyzing the rectangle as a whole, we study each side individually, then combine the results for the four sides. We assume that the rates of the various mechanisms vary linearly along the sides of the rectangle. Therefore, if one mechanism is dominant at both ends of a side, it is dominant over the entire side. If two different mechanisms are dominant at the two ends, there are two or three dominant mechanisms on the side, and the points where the boundary or boundaries intersect the side may be calculated using a linear interpolant. Sides with four or more dominant mechanisms can be ignored because of the assumption that only the four topologies of Figure 1 are present.

The topology of the rectangle may be determined by simply adding the number of points where boundaries intersect the four sides of the rectangle. Plotting is trivial if there are zero or two such points. If the boundaries intersect the sides of the rectangle at four points (two nonintersecting boundaries), it is only necessary to draw the boundaries between appropriate pairs of points. If the boundaries intersect the sides of the rectangle at three points (three intersecting boundaries), plotting cannot be done until the location of the intersection is found. In this case, we temporarily treat the rectangle as if only two dominant mechanisms were present, so that the boundary goes all the way across the rectangle. The three line segments obtained will intersect at three points, the centroid of which is used as the intersection of the three boundaries. This procedure is illustrated in Figure 2. The point of intersection could be calculated directly by using a bilinear interpolant and solving for the point at which all three mechanisms have equal rates.

Calculation of Contours

Let us now consider the methods used in calculating the positions of the contours of constant deformation rate. First we will consider the case where the entire rectangle lies within a single region of dominance, then we will see how the procedure must be modified to treat cases in which the rectangle is divided between two or more regions of dominance.

In either case, the first step in contouring is to find out which contours will pass through the rectangle. To do this, we must find the minimum and maximum rates of the dominant mechanism(s). If a single mechanism is dominant throughout the rectangle, it is only necessary to check for extrema at the four corners. If there are two or more dominant mechanisms, it is also necessary to check the rates at the points where the boundaries intersect the sides of the rectangle and, if there is such a point, where three boundaries intersect. Given the minimum and maximum rate, the minimum and maximum contour levels follow immediately.

For the case in which a single mechanism is dominant throughout the rectangle, we first search all four sides of the rectangle for points where the rate of the dominant mechanism is the same as a contour level. There will be either two or four such points. If there are two points, the contour is taken to be the line segment which connects the points. If there are four points, a more or less arbitrary criterion must be used to decide which pairs of points will be connected by contours.

For the case in which two or more mechanisms are dominant in different portions of the rectangle, each mechanism is contoured individually as if it were dominant throughout the rectangle. The contour segments are then "cut to length" by truncating them at the point where they enter a different region of dominance.

Sorting and Plotting

If the methods described above are applied to every rectangle in the map, the boundaries and contours will be completely calculated, at least in principle, ready to be plotted. To avoid inefficient use of the plotter and to assure a smooth appearance, however, it is necessary to sort the line segments.

It is clear that standard algorithms for sorting a list of numbers cannot be used. All of the efficient sorting algorithms (Shell sort (9), quick sort (10), heap sort (11)) make use of the fact that, if two numbers are chosen at random from the list, it is possible to tell which of the two will precede the other when the sort has been completed. With a list of line segments, however, it is usually not possible to tell if two randomly chosen line segments are even part of the same curve.

The simplest approach to this problem would be to compare the position of the last known point on the curve with each endpoint of each line segment in the list. Segments which have been plotted would be marked in some way to prevent subsequent replotting. Such an approach would work, but it would be very slow if the list were long.

The efficiency of the basic algorithm described above can be improved in two ways: First, we can restrict our definition of a curve, and second, we can exploit the existing order in the list of line segments.

Since we are dealing with a list of line segments, the "curves" which we have been discussing are in fact polygonal paths. Usually, each side of these polygonal paths corresponds to a single line segment. Let us now define a "directed curve" as a polygonal path in which each side points to the right or straight up. Figure 3 shows a curve and its dissection into directed curves.

From the definition of a directed curve, it follows that each of the line segments in a directed curve has a definite starting point and a definite ending point. The x coordinate of the starting point is less than the x coordinate of the ending point, and if these are equal, the y coordinate of the starting point is less than the y coordinate of the ending point. Also, each line segment in a directed curve except the first and the last has a unique predecessor and a unique successor.

The use of directed curves has two practical consequences for the sorting and plotting of a list of line segments. First, as Figure 3 makes clear, complicated curves may be broken up into several directed curves which are plotted separately. This is not desirable, but it has little impact upon the preparation of mechanism maps since it rarely occurs. Second, when searching for a successor to the current line segment, the position of the ending point of the current line segment need only be compared to the starting points of the potential successors; the ending points may be ignored. This cuts the length of the search in half.

Let us now investigate how the search time can be cut further by exploiting the existing order in the list of line segments. When we calculate a map, we scan the map in columns of rectangles, working from the left edge of the map to the right edge. Within each column, we scan from the bottom of the column to the top. Within each rectangle, we sort the list of line segments according to the y coordinate of the starting point of the segment. Since the rectangles do not overlap, the ordering of the y coordinate extends throughout the column. The list of line segments is, therefore, highly ordered: it is divided into columns; the segments in one column are ordered from bottom to top; each segment points to the right or straight up.

From this, it is clear that the successor to a given line segment must be either in the current column (the column which contains the current line segment) or in the column just to the right of the current column. Therefore, it is only necessary to search two columns when looking for the successor rather than the whole list. If no successor is found in these two columns, the curve ends.

Further gains in efficiency can be realized by using the fact that the segments are ordered on the y coordinate of their starting points. When searching the current column, the search may start at the current line segment and stop as soon as the y coordinate of a potential successor is so large or so small that segments which are further up or down the column cannot possibly join up with the current segment. A similar strategy may be used in searching the column just to the right of the current column.

Examples

Figure 4 shows two mechanism maps which were calculated and plotted by the methods described here. The same data and constitutive equations were used for both maps, but grids of two different densities were used. It has been claimed (3,8) that a typical map requires the evaluation of deformation rates at 4000 to 6000 points, and maps have been published with at least 6900 evaluation points (12). By contrast, Figure 4a used evaluations at 441 points, and irregularities in the curves are barely perceptible. Only 169 evaluations were used in the preparation of Figure 4b. The resulting irregularities in the map are visible but hardly objectionable. Clearly, careful use of the data results in a dramatic improvement in efficiency.

Acknowledgment

This work was supported by the Air Force Office of Scientific Research under Contract AFOSR-82-0238.

References

1. J. Weertman and J. P. Weertman, in R. W. Cahn (ed.) *Physical Metallurgy*, North-Holland, Amsterdam, p. 793 (1965).
2. M. F. Ashby, *Acta Met.*, 20, 887 (1972).
3. T. G. Langdon and F. A. Mohamed, *Mater. Sci. Eng.*, 32, 103 (1970).
4. P. A. Urlick and M. A. Notis, *J. Am. Ceram. Soc.*, 56, 570 (1973).
5. F. B. Swinkels and M. F. Ashby, *Acta Met.*, 29, 259 (1981).
6. C. Gandhi and M. F. Ashby, *Acta Met.*, 27, 1565 (1979).
7. P. B. Linkson, B. D. Phillips and C. D. Rowles, *Corros. Sci.*, 19, 613 (1979).
8. T. G. Langdon and F. A. Mohamed, *J. Mater. Sci.*, 13, 1282 (1978).
9. D. L. Shell, *Comm. ACM*, 2, No. 7, 30 (1959).
10. C.A.R. Hoare, *Comm. ACM*, 4, 321 (1962).
11. J.W.J. Williams, *Comm. ACM*, 7, 347 (1964).
12. A. Mohan, N. C. Soni and V. K. Moorthy, *J. Nucl. Mater.*, 79, 312 (1979).

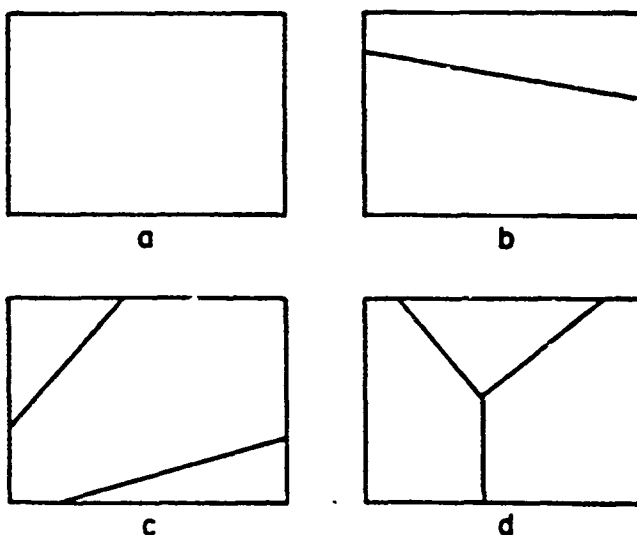


FIG. 1

Four Possible Topologies for Boundaries in One Rectangle of the Map

- a. No boundaries, b. One boundary,
- c. Two nonintersecting boundaries,
- d. Three intersecting boundaries.

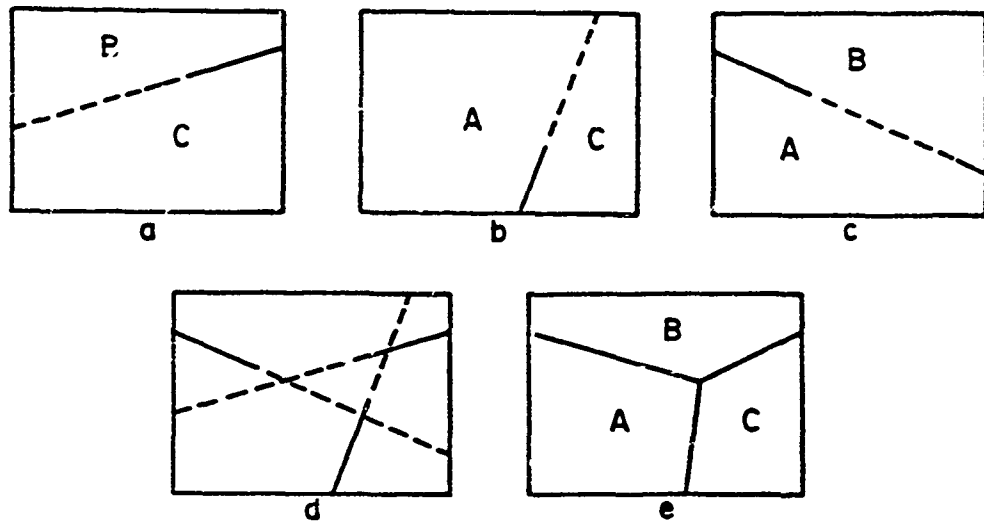


FIG. 2

Treatment of Three Intersecting Boundaries: a,b,c. Location of single boundary if third mechanism were absent. Dotted portion of boundary will be cut off by third mechanism. d. Superposition of a, b, and c. Due to approximations, boundaries do not intersect at a single point. e. Composite map with regions of dominance labeled. Intersection is drawn at centroid of middle triangle in d.

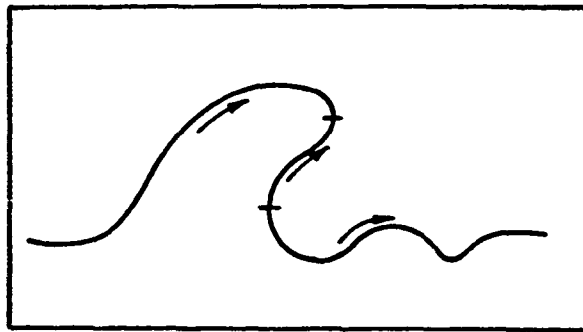
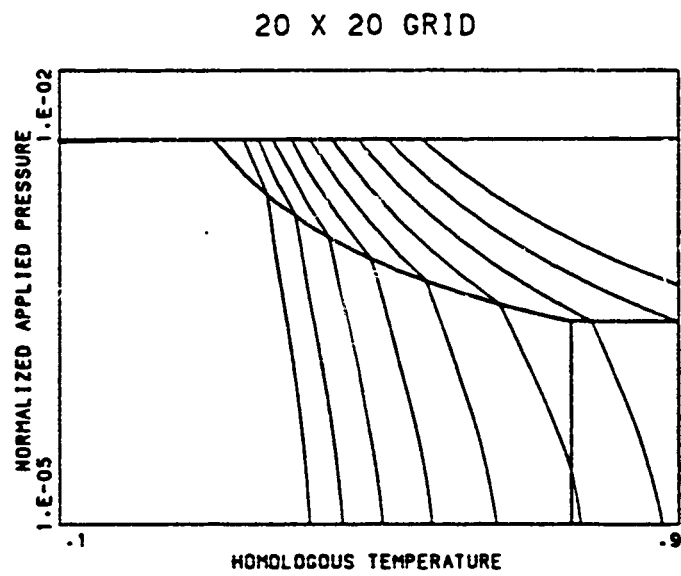
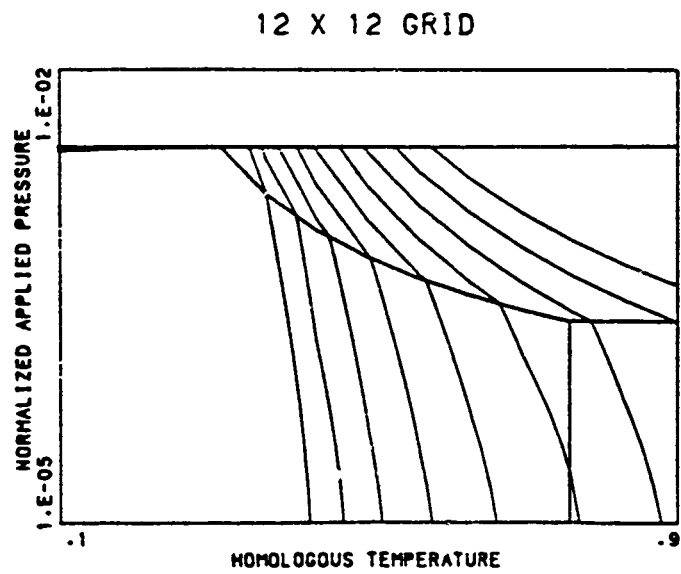


FIG. 3

A Typical Curve and Its Dissection Into Three Directed Curves



(a)



(b)

FIG. 4

Typical Mechanism Maps, Calculated at Two Grid Densities

APPENDIX B

DILATOMETER TECHNIQUE FOR
HOT ISOSTATIC PRESSING

Reprinted from

Ceramic Engineering and Science Proceedings,
vol. 6, pp. 1146-1150 (1985)

Dilatometer Technique for Hot-Isostatic Pressing*

J. KEVIN MCCOY AND ROGER R. WILLS*

Battelle Columbus Laboratories
505 King Avenue, Columbus, OH 43201-2693

A dilatometer technique is described for hot isostatic pressing (HIP) that provides far more data from each HIP experiment than can be obtained by conventional HIP practice. The design, data analysis, and typical results obtained with the dilatometer are described.

Introduction

Before hot isostatic pressing (HIP) can be applied in the production of a ceramic component, it is necessary to determine an appropriate HIP cycle for developing the desired properties, such as a given level of density. Those who are involved in cycle development for HIP know that this is frequently a long, difficult, trial-and-error process. This paper describes a dilatometer technique for HIP that provides far more data from each HIP experiment than can be obtained by conventional HIP practice. Because more information is collected from each experiment, the amount of work necessary for cycle development is greatly reduced. The dilatometer technique was developed at Battelle-Columbus with support from the Air Force Office of Scientific Research. To explain how this method works, we will first describe the design of the dilatometer, then the data analysis, and finally give an example of typical results obtained by this method.

Procedure

The design of the dilatometer is shown schematically in Fig. 1. A cylindrical sample, shown end-on in the figure, is heated in a cylindrical furnace. The sample temperature is monitored by a thermocouple. From the cold zone, well outside the furnace, two tungsten rods run up to the sample. The rods are attached to pivots, which are shown as triangles, and are held in contact with the sample by a spring, which is not shown. The bottom ends of the tungsten rods are attached to a linear variable differential transformer (LVDT). The entire apparatus is enclosed in an autoclave.

The thermocouple and LVDT provide a continuous record of the temperature and diameter of the sample as functions of time. These data are subsequently used to calculate a record of density as a function of time. To understand how they are used, it is necessary to take a closer look at the sample geometry. Figure 2 shows a cutaway view of the sample. The sample proper is a ceramic cylinder; it is encased in a close-fitting, airtight, cylindrical metal capsule. Strictly speaking, the dilatometer provides a record of the capsule outside diameter rather than a

record of the diameter of the sample itself. Therefore, the computational procedure may be summarized as follows: We assume some fractional density, then calculate the corresponding capsule diameter, using the treatment described below. If the calculated diameter agrees with the value reported by the dilatometer, then the assumed fractional density is correct. If not, a new fractional density is chosen and the process is repeated.

There is an apparent weakness in this computational procedure: The dilatometer gives only the diameter of the capsule, but the length will also affect the calculated density. This difficulty is handled in the following way. As the sample densifies, its length changes from its initial value L_i , through some intermediate value L , to a final value L_f .

Similarly, the diameter changes from its initial value D_i , through some intermediate value D , to a final value D_f . The initial dimensions can be determined before the sample is placed in the capsule, and the final dimensions can be determined after HIP by removing the capsule. It is then assumed that the current length of the sample is related to the current diameter by the equation

$$\frac{L}{L_i} = \left(\frac{D}{D_i}\right)^k \quad (1)$$

The value of the constant k is obtained by inserting the final values of L and D , and solving for k . Given Eq. 1 and the initial density and initial dimensions of the sample, the length and diameter of the sample can be calculated for any specified density. Typical values of k are about 0.85, so changes in the length/diameter ratio are relatively small.

Changes in the geometry of the sample naturally give rise to changes in the geometry of the capsule: as densification proceeds, there is a distinct thickening of the capsule sidewall. This effect is treated by applying the law of conservation of matter. It is assumed that any matter in the sidewall at the beginning of HIP stays in the sidewall, and that matter from the capsule ends does not transfer to, or from, the sidewall. It is also assumed that the capsule stays in close contact with the sample, so the inside diameter of the capsule equals the diameter of the sample, and the length of the capsule sidewall equals the length of the sample.

The computational procedure given above can now be described in greater detail. A fractional density is assumed for the sample, and from this the sample dimensions at 20°C are calculated. The coefficient of thermal expansion is then used to determine the sample dimensions at the actual HIP temperature. From the initial sidewall mass, the sidewall volume at 20° C is calculated, and the coefficient of thermal expansion for the capsule material is used to determine the sidewall volume at temperature. The sample dimensions and capsule sidewall volume are then used to calculate the capsule sidewall thickness, and the capsule outside diameter is just the sample diameter plus twice the sidewall thickness. If the calculated capsule diameter is equal to the diameter reported by the dilatometer, then the assumed density is correct; otherwise, it is necessary to try a different fractional density.

Results

The type of results obtained by this method is shown in Fig. 3. During most of the heatup of the sample, essentially no densification occurs.

While the sample was held at 1050°C and 34 MPa, it densified to about 80% of its theoretical density. At this point, the pressure was then increased to 100 MPa in order to speed up densification. These conditions were maintained until the sample density reached 91% of theoretical density. Another increase in densification rate was then obtained by increasing the temperature to 1150°C. Under these conditions, the sample reached a density of 97%. All this information was obtained from a single experiment. If we had used conventional HIP practice, one experiment would have given us only the initial and final densities. To obtain a density vs time curve of the type shown here would have required many experiments. To make matters worse, there would have been sample-to-sample and run-to-run variations, which would have greatly complicated data analysis. With the dilatometer, however, a single plot is obtained which clearly shows the response of the system to changes in temperature and pressure, and that is vital information in developing an appropriate HIP cycle.

Conclusions

In summary, the primary feature of this dilatometer technique is that it provides a continuous record of density as a function of time during HIP. The large amount of information provided by the method is the key to its principal benefit: much faster development of HIP cycles.

*A more detailed version of this work has been accepted for publication in the *American Ceramic Society Bulletin*.

Now at TRW, Inc., Cleveland, OH.

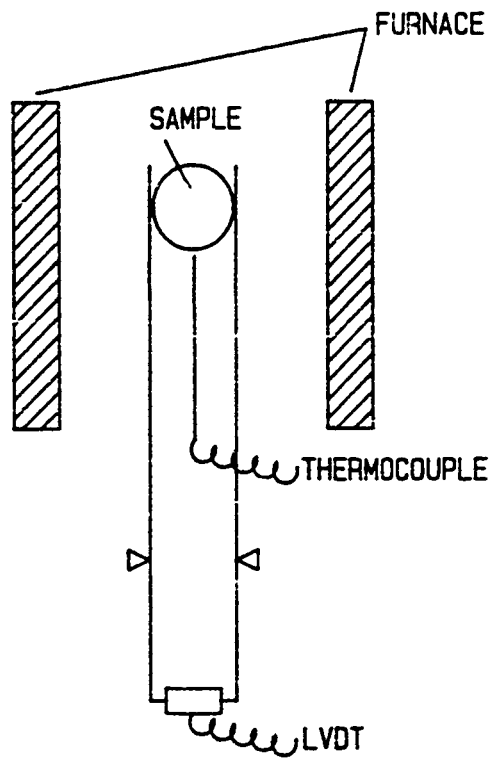


Fig. 1. Design of dilatometer.

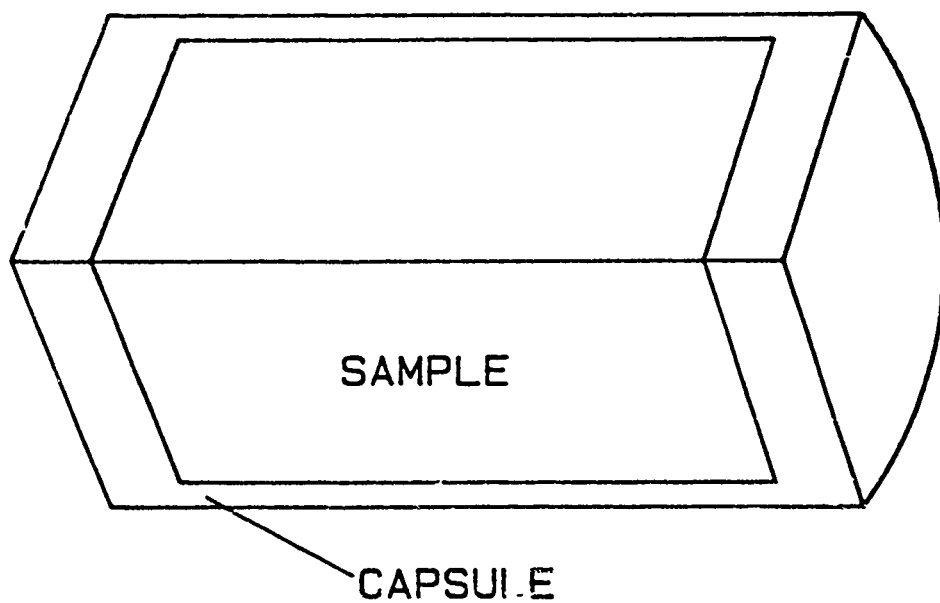


Fig. 2. Sample geometry.

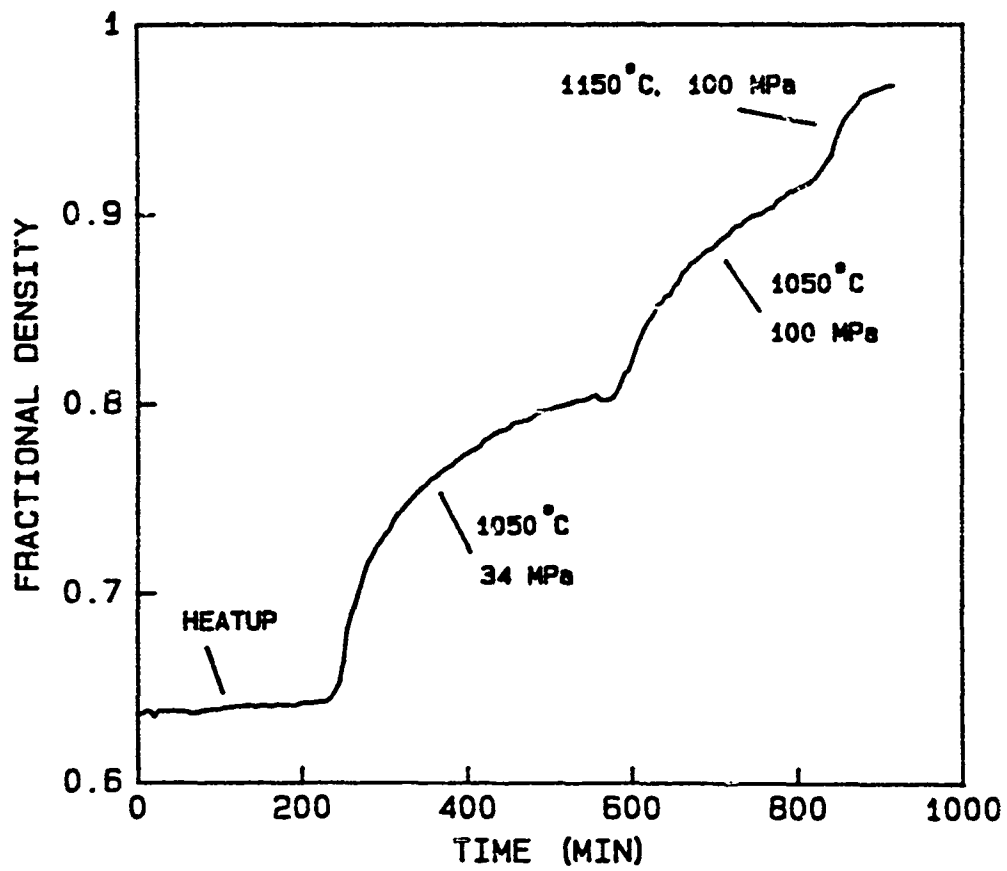


Fig. 3. Results of typical HIP experiment.

APPENDIX C

CONTINUOUS MONITORING OF VOLUMETRIC CHANGES IN
CERAMIC POWDER COMPACTS DURING HOT ISOSTATIC PRESSING

Reprinted from

American Ceramic Society Bulletin,
vol. 64, pp. 1240-1244 (1985)

Continuous Monitoring of Volumetric Changes in Ceramic Powder Compacts During Hot Isostatic Pressing

J. KEVIN McCOY, LARRY E. MUTTART,
and ROGER R. WILLS*

Battelle Labs, Columbus, OH 43201-2693

The hot isostatic pressing (HIP) of ceramic powder compacts consists of several sequential steps. These are: 1) green preform preparation in a pressure-transmitting membrane, capsule, or "can"; 2) actual HIPing by exposing the encapsulated powder compact to a high-pressure gas (typically 100 to 200 MPa) at elevated temperature; and 3) removing the encapsulant surrounding the HIPed powder compact.

Research in this area is usually performed on a trial-and-error basis by analyzing information obtained on samples before and after HIPing in an effort to determine the optimum HIP conditions needed to achieve either complete densification or to produce a ceramic with a specific fractional density (the ratio of the volume of solid in a material to the total volume of material including pores). The process is iterative and sometimes lengthy.

The technique described herein allows volumetric changes to be monitored continuously. Data are collected throughout the HIP cycle, consequently the temperature and pressure processing parameters can be changed if the selected parameters do not appear to be achieving the desired objective (usually full density). Data output is corrected for thermal expansion effects to obtain exact density changes as a function of time. This paper briefly describes the apparatus and the error-correction routine. The use of the equipment is demonstrated in HIPing submicron alumina powder in a stainless steel capsule.

Apparatus

HIP equipment consists of gas storage tanks, compressors, and a water-cooled autoclave containing the furnace and heat shield package. The furnace is usually loaded through the top and the electrical connections lead from the bottom of the vessel. A 10.16-cm diameter, 11.68-cm high molybdenum furnace capable of operating at 1750°C was modified to contain a pedestal and a two-probe dilatometer (see Fig. 1) attached to a linear variable differential transformer (LVDT). The 3.175-mm diameter tungsten probes are in close contact with a stainless steel capsule containing

A two-probe dilatometer, fitted into a molybdenum furnace, permits continuous recording of the volumetric changes occurring inside a metal-encapsulated ceramic powder compact during hot isostatic pressing. The effects of thermal expansion of the metal capsule and the ceramic compact are deleted from the raw data by a computer program, and the nonlinear shrinkage relation between the capsule diameter and length is allowed for. Use of the equipment is demonstrated in the hot isostatic pressing of a submicrometer alumina powder enclosed in a stainless steel capsule.

a close-fitting cylindrical alumina powder compact. Two thermocouples monitor the temperature, one in contact with the tungsten probes supporting the specimen, the other slightly above the specimen.

An asbestos-based, ceramic insulating plate below the base heater and radiation baffles attached to the tungsten probes maintain the operating temperature at 180°C during HIPing of alumina at 1200°C. The LVDT range of 0.254 cm is linear to within 0.25%. Preliminary experiments were performed using a molybdenum disk to determine the accuracy of the probe/LVDT equipment under HIP conditions. A multichannel chart recorder monitored the LVDT output, temperature, and pressure. The measured thermal expansion of this disk at 1300°C and 1600°C differed from the published data¹ by 0.5%.

Experimental

Cylindrical specimens, 26-mm diameter by 102 mm long, were formed from submicron, alumina* powders by isostatic pressing at 345 MPa. These specimens were then bisque fired at 1120°C and ground to final 22-mm diameter and 39.68 mm length. This procedure was adopted to ensure that the alumina specimens closely fit the stainless steel capsules. The specimens and capsules were then dried and vacuum outgassed at 1000°C for 1 hour. Each specimen was weighed, and the initial dimensions of each specimen and

Table I. Physical Measurements of Samples and Capsules for Hot Isostatic Pressing Required for Data Manipulation

Dimension (mm)	Experiment No.					
	1	2	3	4	5	6
Initial sample* length	39.67	39.68	39.70	39.66	39.67	39.68
Initial capsule length	51.32	52.24	49.90	50.91	50.82	52.45
Final capsule length	46.82	47.90	45.28	49.04	46.35	48.22
Initial total end plug length	11.10	11.13	9.45	10.97	11.10	12.76
Final total end plug length	11.69	11.60	10.08	11.16	11.79	13.57
Initial sample diameter	22.00	22.00	22.00	22.00	22.01	22.01
Initial capsule diameter	25.39	25.37	25.33	25.36	25.37	25.38
Final capsule diameter	23.28	23.85	23.33	24.53	23.11	23.25
Initial capsule wall thickness	1.57	1.57	1.57	1.57	1.66	1.66
Final capsule wall thickness	2.12	1.98	2.08	1.83	2.18	2.72
Initial fractional density	0.6552	0.6556	0.6556	0.6549	0.6370	0.6368

*Member, the American Ceramic Society
*Reynolds RC-HP-DBM Alumina, Reynolds Metals Co., Bauxite, AR

Received October 9, 1984, revised copy received February 1, 1985, approved March 26, 1985

*Sample refers to ceramic compact

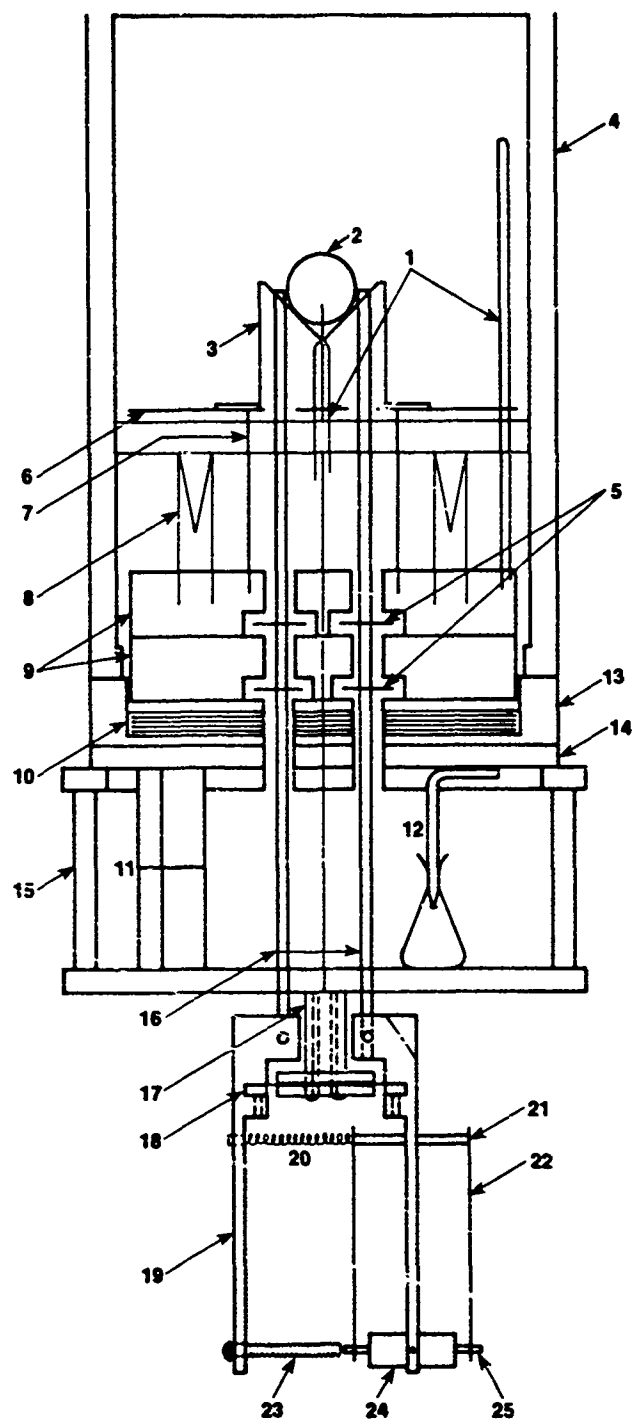


Fig. 1. Schematic of dilatometer and furnace for hot isostatic pressing. Key: 1. encased thermocouples (W/Re6); 2. specimen; 3. specimen trough; 4. thermal barrier and cover; 5. radiation and gas flow baffles; 6. perforated moly hearth; 7. moly-tubular pedestal; 8. moly ribbon heater; 9. alumina base plates; 10. radiation shields; 11. couple connection; 12. power connection; 13. furnace base; 14. transite base; 15. frame; 16. tungsten probes; 17. inverted pedestal; 18. spring steel hinge each end; 19. extension of probe arms; 20. very light compressive spring; 21. yoke; 22. spring steel yoke arms; 23. physical zero adjust screw; 24. LVDT; 25. core.

capsule taken with a micrometer. Figure 2 shows the measured dimensions and actual values are listed in Table I. The capsules were then sealed under vacuum by electron beam welding.

After each sample was placed in contact with the tungsten probes, adjustments were made to the LVDT and the chart recorder was adjusted to zero. The zero position on the chart recorder was

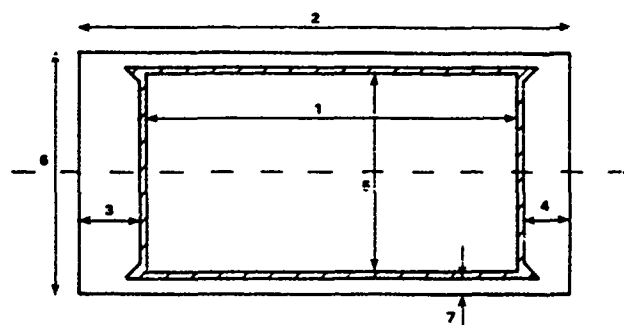


Fig. 2. Cross section of capsule and sample for hot isostatic pressing, showing measurements. (1) Sample length, (2) capsule length, (3,4) end plug length, (5) sample diameter, (6) capsule diameter, (7) capsule wall thickness. Gap between capsule and sample (shaded area) is exaggerated; dashed line is axis of capsule.

set to accommodate initial contraction of the capsule diameter. Each HIP cycle involved: 1) initial gas pressurization, 2) heating at 400°C per hour to the desired temperature under a constant pressure, 3) HIPing under the required temperature/pressure conditions, and 4) allowing the specimen to cool to room temperature. The final dimensions of the capsule (diameter and length) and the thickness of the capsule end plugs were determined with a micrometer (see Table I). While seven measurements are necessary to describe the initial capsule and sample geometries, only five are required after HIPing since there is no longer a gap between the sample and the capsule. The immersion technique was used to determine the sample density after the capsule was removed.

During the HIP cycle, changes in the position of the probes are registered in the LVDT output recorded by the chart recorder. Several factors are responsible for this movement. Initial pressurization of the autoclaves caused some small movement, but, after pressure equilibration, the chart reading returned to the zero position. During heatup, capsule deformation results in a thickened capsule wall and both the stainless steel capsule and the alumina powder compact expand. All of these effects give rise to a decrease in the value registered by the chart recorder. Densification results in a decreased capsule diameter, and the chart pen moves in the opposite direction. The actual point recorded by the chart pen at any one time is the sum of these effects.

Conversion of LVDT Output to Fractional Density Data

Data from several sources are combined to produce density as a function of time. The thermocouples and LVDT provide the temperature of the sample and the outside diameter of the capsule as a function of time. The dimensions of the sample and capsule at the beginning and end of the HIP cycle are also needed to calculate the density. These data are then processed by a program that compensates for thermal expansion and thickening of the capsule wall.

Data reduction starts by keying temperature, pressure, and capsule-shrinkage data from the strip chart recorders into a computer. Data points are chosen so that discrete points will provide a good description of the actual experiment. Since the time interval between data points is small, linear interpolation is used between the readings. Physical dimensions and initial density data are inserted at the beginning of the file.

The data are converted to fractional densities by a FORTRAN computer program. Before discussing the algorithm, it is appropriate to describe the underlying assumptions used in deriving the algorithm and to estimate the error incurred. Using the example of an alumina powder compact encapsulated in a stainless steel capsule, the integrated thermal expansions of alumina and stainless steel are:

$$\alpha_{Al_2O_3} = 7.2978E - 6(T - 293) + 7.8486E - 10(T - 293)(T - 800) \quad (1A)$$

$$\alpha_{304SS} = 1.7751E - 5(T - 293) + 5.0423E - 9(T - 293)(T - 800) \quad (1B)$$

Table II. Capsule Sidewall Masses Determined by Various Methods

Experiment No	Sidewall mass (g)		
	Method 1	Method 2	Method 3
1	37.440	36.929	39.186
2	38.233	36.903	39.034
3	37.634	36.932	38.619
4	37.125	36.872	39.139
5	38.883	38.843	39.169
6	38.714	38.704	38.582

In these equations, which are integrals of the ordinary coefficients of linear thermal expansion, E denotes multiplication by the specified power of 10, following the standard computational convention. The temperature T is given in degrees Kelvin. These equations were obtained by fitting a quadratic to data compiled by Touloukian.¹ Several other thermal effects might be anticipated. First, the probe rod's length will change both above and below the pivots. Second, the pivots themselves may move due to thermal expansion. Third, the sample may be displaced as its supporting structure expands. Finally, when the temperature gradient has a component normal to the axis of the probe rods, the rods will deflect. It is not feasible to perform an accurate calculation of all thermal expansion effects. Our calculations have used a simple approach by assuming that all thermal expansions except those of the sample and the capsule have a negligible net effect on the measured capsule diameter. The validity of this assumption is supported by the good agreement between the measured thermal expansion of the molybdenum disk and the literature data.

During the HIP cycle, the thickness of the capsule sidewall changes due to thermal expansion of the encapsulant and densification of the sample. In determining sample density, it is necessary to consider both effects and to make some assumptions regarding redistribution of matter in the sidewall. We have assumed that the sidewall does not slip axially along the capsule. Thus, changes in length or diameter of the sample or the capsule are assumed to be taken up by wall thickening, rather than by moving matter to or from the ends of the capsule. This assumption should be realistic since the capsule is always being forced against the sample by the applied gas pressure. Although the assumption may be somewhat inaccurate near the ends of the sample, our measurements of capsule diameter are made near the middle of the sample, well removed from end effects.

The importance of the correction for thermal expansion can be seen from the following example. Using the final dimensions from experiment No. 1, the combined thermal expansion of the sample and the capsule upon heating from 20° to 1150°C is 0.378 mm in diameter if the fractional density of the sample remains constant. To produce this large a change in size at constant temperature would require a change of 0.08 in the fractional density of the sample.

Another important consideration is the effect of temperature and densification on the shape of the sample. We have assumed that the thermal expansion of alumina is isotropic for a fixed fractional density. However, the length-to-diameter ratio of the sample at the beginning of the HIP cycle is different from that at the end, so a

Table III. Comparison of Final Densities as Determined by Calculation from Probe Data and by Direct Measurement

Experiment No	Final fractional density		Difference
	Calculated	Measured*	
1	0.9576	0.960	-0.002
2	0.8712	0.876	-0.005
3	0.9678	0.952	0.016
4	0.7697	0.758	0.012
5	0.9678	0.984	-0.016
6	0.9617	0.970	-0.008

*Determined by liquid immersion technique

change in shape accompanies the density change. The capsule's diameter is recorded continuously, but its length is measured only at the beginning and end of the HIP cycle. It is therefore necessary to assume some relationship between the length and diameter during the HIP cycle. It is assumed that:

$$\frac{L(\rho, 20)}{L(\rho_i, 20)} = \left(\frac{d(\rho, 20)}{d(\rho_i, 20)} \right)^k \quad (2)$$

where $d(\rho, 20)$ and $L(\rho, 20)$ denote the sample diameter and length, respectively, at the fractional density in question and corrected to 20°C. The subscript i denotes an initial value. The exponent k is set by the initial and final measured lengths and diameters of the sample. A typical value for k is 0.85. The assumption of Eq. (2) is essentially arbitrary, and other relations might be suggested, e.g.,

$$\frac{L(\rho, 20) - L(\rho_f, 20)}{L(\rho_i, 20) - L(\rho_f, 20)} = \frac{d(\rho, 20) - d(\rho_f, 20)}{d(\rho_i, 20) - d(\rho_f, 20)} \quad (3)$$

where the subscript f denotes a final value. The maximum difference in calculated sample lengths given by Eqs. (2) and (3), for any sample length, is about 0.013 mm. This corresponds to an error in density of less than 0.04%. This is considered negligible in our experiments.

The initial gap between the sample and the capsule vanishes during HIP. Thus the final sample diameter is the final outside capsule diameter minus twice the final capsule wall thickness, and the final sample length is the final capsule length minus the thickness of the end plugs. This assumption is supported by sample examination after HIPing. No gaps were found after HIPing. A thin 0.2-micron reaction layer consisting of oxides of iron, aluminum, chromium, and nickel was detected between the alumina sample and the stainless steel capsule. An error in density of less than 0.05% results from ignoring this layer.

Putting all these factors together, the program proceeds in the following way. Pressure, temperature, and shrinkage are measured for a given time, and the diameter of the capsule is calculated by subtracting the shrinkage from the original size. Then the problem is attacked from the other direction. A fractional density is assumed for the alumina sample, and the diameter and length of the sample at 20°C are calculated using Eq. (2) and the mass of the sample. The dimensions of the sample at temperature are then calculated using Equation (1A). The volume of the capsule sidewall at 20°C is corrected for temperature by converting the linear expansion of Equation (1B) to a volume expansion, and the necessary wall thickness to produce that volume is calculated. For the assumed density, the outside diameter of the capsule will be the sample diameter plus twice the wall thickness. The program repeats this process with different values of density until it finds an outside diameter equal to the actual diameter of the capsule. The output of the program is a table consisting of five columns of data: temperature, pressure, time, capsule shrinkage, and fractional density.

One difficulty with this approach is that there are several methods for treating the sidewall. For any of these methods, the mass of the sidewall is constant since it is assumed that the sidewall does not slip over the sample during densification, and the mass is given by

$$M = \pi w(D - w)L\rho \quad (4)$$

where w is the sidewall thickness, D is the outside diameter of the capsule, L is the length of sidewall, and ρ is the absolute density of the capsule material. The sidewall mass can be obtained in three ways: 1) w is assumed to be the initial capsule wall thickness, D the initial outside diameter of the capsule, and L the initial capsule length minus the initial length of the end plugs; 2) w is assumed to be the initial capsule wall thickness, D the final outside diameter of the capsule, and L the initial sample length; and 3) w is assumed to be the final capsule wall thickness, D the final outside diameter of the capsule, and L the final sample length. The length L used in Method 1 is longer than that used in Method 2, the difference being the length of the gaps between the sample and the end plugs (see Fig. 2). Method 3 differs from the other two since

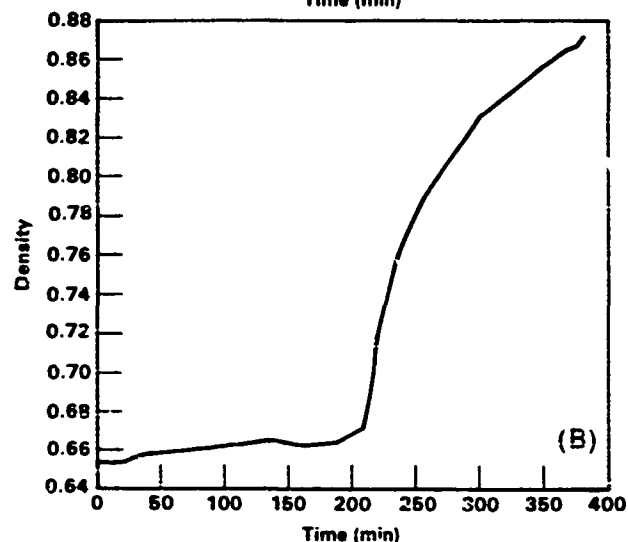
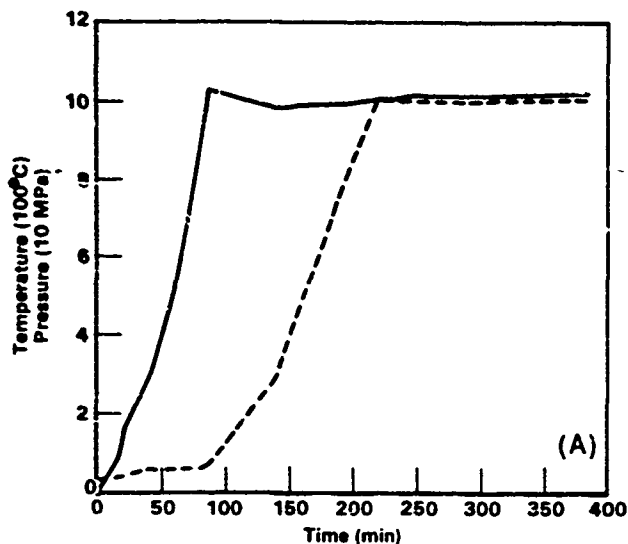


Fig. 3. Data for experiment No. 2. (A) Pressure (solid line) and temperature (dashed line) vs time. (B) Relative density calculated from temperature and capsule shrinkage for alumina at 1000°C and 102 MPa

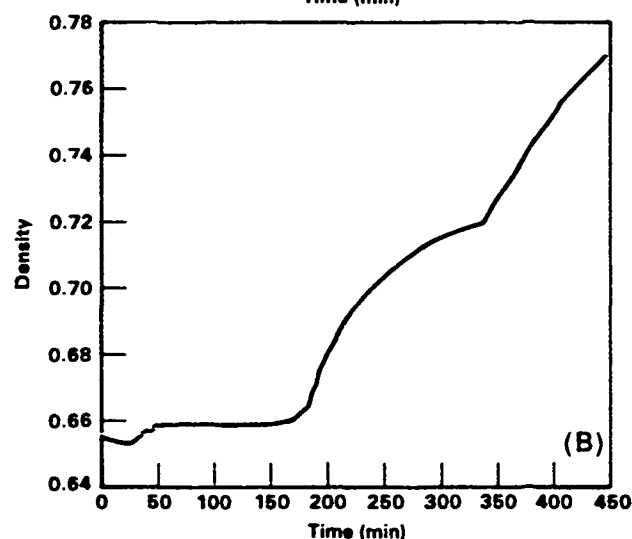
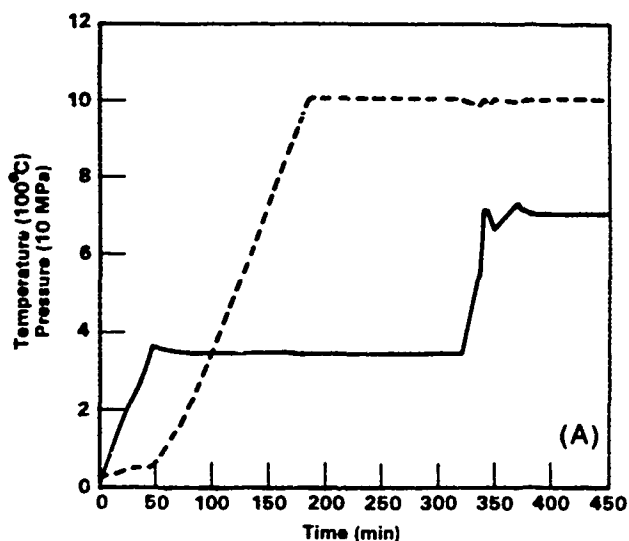


Fig. 4. Data for experiment No. 4. (A) Pressure (solid line) and temperature (dashed line) vs time. (B) Relative density calculated from temperature and capsule shrinkage. Density curve clearly shows effect of changing pressure from 34 to 70 MPa at 330 min.

it uses final measurements instead of initial ones. Table II shows the sidewall masses determined by these three methods. As expected, the masses calculated by Method 2 are consistently smaller than those given by Method 1, since Method 2 assumes a slightly longer sidewall. The choice of sidewall mass affects the density value calculated from the capsule shrinkage data. Fractional densities can differ by as much as 4.6%. Method 1 can probably be discounted since all samples, including those that exhibited a small density increase during HIPing, were bonded to the capsule. It is likely that significant capsule deformation occurred prior to shrinkage of the alumina compact and removed the gap between the sample and the capsule.

We have used Method 3 to obtain the sidewall mass since it does not require any assumption regarding the nature of the deformation of the capsule. In Table III, we show the final densities as calculated from the probe data and determined directly by the immersion technique. The root-mean-square difference between the calculated and measured densities is 1.2%. Among the various possible sources of error, the following are probably the most significant. First, there is some uncertainty in the measurements of the initial and final densities. These errors are estimated at about 0.2% each. Second, there are significant variations in the reported values of the coefficients of thermal expansion, particularly for alumina. If the coefficient of linear thermal expansion for alumina is in error by 15%, the calculated fractional density will be in error by 0.3%. A

5% error in the thermal expansion of stainless steel would also cause an error of about 0.3%. Third, we have assumed that the sample remains cylindrical during densification, but this is not quite correct. After HIP, the sides of the sample flare slightly toward the ends, and the end surfaces become slightly domed. The magnitude of the effects of this shape change on the calculated final density is unknown. Finally, if there are variations of density with position in the bisque-fired sample, the dilatometer may be providing data on a portion of the sample which is not typical of the entire sample. If the fractional density in the vicinity of the dilatometer probes differs from the average for the entire sample by 0.5%, the calculated final density will also be in error by 0.5%. In light of these considerations, the calculated and measured densities appear to be in reasonable agreement.

Application

The dilatometer and computer software program enables volumetric changes to be determined inside the autoclave. Thus, we can obtain quantitative data about density changes and phase changes occurring during the HIP cycle. Reaction kinetics data may also be obtained by measuring densification rates as a function of density, temperature, and pressure and altering the temperature and/or pressure during the cycle. Examples of the use of the dilatometer are given in Figs. 3 and 4. Figures 3(B) and 4(B) show typical density-time plots for the densification of alumina at 1000°C and



J. Kevin McCoy



Lawrence E. Muttart



Roger R. Wills

J. Kevin McCoy is a research scientist in the Physical Metallurgy Section at Battelle, Columbus Labs, Columbus, OH. He received a B.S. Met. E. in 1975, an M.S. Met. E. in 1977, and a Ph.D. in materials science in 1980, all from Purdue University. Most of his research efforts have involved classical and atomistic modeling of materials behavior.

Lawrence E. Muttart is a research scientist in Battelle's Physical Metallurgy Section. A graduate of the University of

Toledo, he earned a B.E. in 1946 and an M.S. in glass technology in 1951. He has held positions with Owens-Illinois, Inc., Owens Corning Fiberglas, A. P. Green Refractories Co., Ohio State University, and Plymouth Locomotive Works. His interests include material characterization and processing of ceramics and metals.

Roger R. Wills is manager of advanced ceramic components at TRW, Inc., Cleveland, OH. He graduated from Manchester University, England, with a B.Sc. in chemistry in 1965 and a Ph.D. in metallurgy in 1968. Prior to joining TRW, he was with Lucas Co., England, Aerospace Research Labs at Wright-Patterson AFB, Systems Research Labs, and Battelle. He is interested in the dynamic compaction of ceramics, laser processing of ceramics, and high strength ceramic composites.

Figures 3(A) and 4(A) show the changes in temperature and pressure for these two HIP cycles during pressurization, heat up, and HIPing at 1000°C. Figure 3(B) shows that significant densification does not occur until the temperature approaches 1000°C, at which temperature the densification rate initially increases rapidly. The densification rate subsequently falls with increasing fractional density as expected. In experiment No. 4 (see Fig. 4) the pressure was changed from 34 MPa to 70 MPa during the HIP cycle. The change in gradient of the density-time plot (Fig. 4(B)) at a fractional density of 0.72 shows that the HIP densification of alumina is pressure dependent. The densification rate is proportional to the square of the pressure.² The initial drop in density shown in Fig. 4(B) is not a real effect. We believe it was due to a temporary movement of the probe arms during initial gas pressurization. It was not observed in any of the other experiments.

From a practical standpoint, considerable time and cost savings are achieved using the dilatometer. More experimental data can be obtained in one cycle, and the optimum conditions for HIPing powder compacts to full density can be determined quickly by altering the processing conditions during the HIP cycle. This approach virtually removes the costly iterative trial-and-error method commonly used. While the equipment has been used mainly to examine the densification of powder compacts it can also be used to monitor changes occurring in sintered ceramics (e.g., densification, swelling, and phase changes).

In our work the HIP conditions have been controlled manually, but extension to real-time process control should be possible. A primary obstacle to achieving real-time control is that a value of k is necessary in calculating density from Eq. (2), and k is determined from the final dimensions of the sample. Therefore, it is necessary to HIP at least one sample to determine k before real-time control is possible. This appears to be a reasonable strategy since our work indicates that k does not vary strongly from sample to sample.

To date, the equipment has been used only at relatively low temperatures ($\leq 1200^\circ\text{C}$) to study the densification of alumina. The stainless steel capsules can be used up to 1400°C, but if molybdenum or tantalum were used as the capsule material, the equipment could be used up to 1750°C. The furnace would have to be modified in order to operate above 1800°C.

Acknowledgments

The authors would like to thank Mr. L. G. McCoy for his guidance and enthusiasm in the installation of the dilatometer, Mr. G. Mead for performing the hot isostatic pressing experiments, and the Air Force Office of Scientific Research for supporting the major part of this work.

References

- Y. S. Touloukian, *Thermophysical Properties of High Temperature Solid Materials*, Vol. 3, pp 211-212, Vol. 4, pp 22-25, Macmillan, New York, 1967
- R. R. Wills and J. K. McCoy, "Interface Reaction Controlled Kinetics in the Hot Isostatic Pressing of Submicrometer Alumina," *J Am Ceram Soc*, **68** [4] C-95-C-96 (1985)

APPENDIX D

INTERFACE-REACTION-CONTROLLED KINETICS IN THE HOT
ISOSTATIC PRESSING OF SUBMICROMETER ALUMINA POWDER

Reprinted from

Journal of the American Ceramic Society,
vol. 68, pp. C95-C96 (1985)

Reprinted from the Journal of the American Ceramic Society, Vol 68 No 4 April 1985
Copyright 1985 by The American Ceramic Society

J. Am. Ceram. Soc., 68 [4] C-95-C-96 (1985)

Interface-Reaction-Controlled Kinetics in the Hot Isostatic Pressing of Submicrometer Alumina Powder

ROGER R. WILLS* AND JOHN KEVIN MCCOY

Battelle's Columbus Laboratories, 505 King Avenue, Columbus, Ohio 43201-2693

The kinetics of densification of alumina powder compacts at 1000° to 1200°C were studied by using a dilatometer to monitor volumetric changes during hot isostatic pressing. The densification rate is proportional to the square of the applied pressure, and densification does not occur below a threshold pressure. Results are interpreted in terms of an interface-controlled reaction mechanism involving the movement of grain-boundary dislocations.

AN EMPIRICAL approach is generally used to determine the optimum conditions for hot isostatic pressing of ceramic powder compacts to full density. We have attempted to remove this empiricism by examining mechanisms responsible for densification during hot isostatic pressing. Furthermore, by comparing the predictions of various constitutive equations with experimental data, we have attempted to show that optimum hot isostatic pressing conditions can be forecast if certain information about the powder is known. Alumina oxide was selected for study since there is a wealth of data on this ceramic. The present communication presents evi-

dence to indicate that, under hot isostatic pressing conditions, the densification of undoped alumina is controlled by an interface reaction involving the movement of grain-boundary dislocations. We believe that this is the first time that this mechanism has been observed to be active in the densification of a ceramic powder compact.

Previous research¹⁻² suggested that the mechanism of densification of submicrometer alumina powder was probably grain-boundary diffusion. After the initial stage of particle rearrangement, densification proceeds by grain-boundary diffusion, causing the average number of contacts per particle to increase. Arzt *et al.*³ expressed this stage of densification mathematically as

$$\frac{dD}{dt} = \frac{12\delta D_b \Omega Z P^*}{r^3 h(D) kT} \quad (1)$$

where δ is the effective grain-boundary thickness, D_b the grain-boundary diffusion coefficient, Ω the atomic volume, P^* the driving pressure for densification, k is Boltzmann's constant, T temperature, Z

the particle coordination number, $h(D)$ a geometric factor depending on density, and r the particle radius. The equation predicts that the rate of densification is proportional to the driving pressure P^* . This is related to the externally applied pressure as follows:

$$P^* = \frac{4\pi^2 P}{\alpha Z D} + P_s - P_i \quad (2)$$

where P is the externally applied pressure, P_s the effective contact pressure resulting from surface tension, P_i the internal pore pressure, D the fractional density of the compact, and α the average neck area. Since powder compacts are outgassed before hot isostatic pressing, P_i is =0. Furthermore, P_s can be considered to be negligible in comparison with the first term in Eq. (2), particularly in view of the relatively high pressures usually used in pressing. At constant density, the net driving pressure is consequently proportional to the applied pressure. Thus, by varying the pressure during the hot isostatic pressing cycle, the dependency of the rate of densification on the external pressure can be determined. Figure 1 shows the effect of changing the pressure from 34 to 70 MPa on the densification of a powder compact encapsulated in a stainless-steel capsule. Assuming that the rate of densification is proportional to P^m , m is =2.1. However, if grain-boundary diffusion is controlling the densification rate, the exponent should be equal to unity (see Eq. (1)). One possible explanation for the value of the pressure exponent is that a combination of mechanisms is operative during hot isostatic pressing. For example, a dislocation-glide mechanism gives a pressure exponent of 3,⁴ and consequently, if it operated in conjunction with grain-boundary diffusion, a pressure exponent of 2.1 might result. This explanation can be discounted since the climb or glide of lattice dislocations is unlikely to occur in the temperature range 1000° to 1200°C. Another

CONTRIBUTING EDITOR—W R CANNON

Presented at the Pacific Coast Regional Meeting, the American Ceramic Society, San Francisco, CA, October 31, 1984 (Basic Science Division No 146-B-84P). Received October 26, 1984; revised copy received January 4, 1985; approved January 7, 1985.

Supported by the Air Force Office of Scientific Research

*Member, the American Ceramic Society

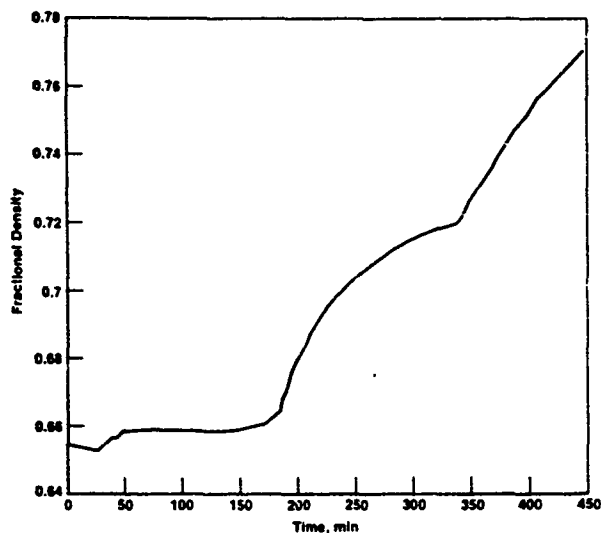


Fig. 1. Effect of changing applied pressure from 34 to 70 MPa on densification of alumina at fractional density of 0.725 (1000°C).

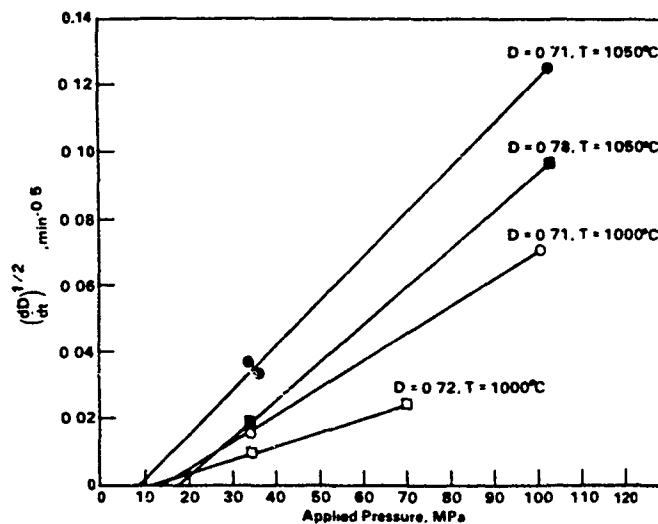


Fig. 2. Densification rate vs applied pressure for fractional densities indicated.

Table I. Threshold Stress Values at Different Temperatures and Fractional Densities

D	Temperature (°C)	n	P _i (MPa)	P _{th} (MPa)
0.71	1050	6.2478	24.435	80.66
0.78	1050	2.9318	8.564	61.33
0.71	1000	6.2478	38.645	132.35
0.72	1000	5.4152	36.403	101.38

er possibility is that basal-plane slip is responsible for densification. This mechanism may contribute, but it could not be the only factor since it does not enable mass transport to occur in all directions.

One mechanism that would explain the results is interface-reaction-controlled grain-boundary diffusion. It is considered to be operative in many creep experiments at low temperatures and small grain sizes where it has been suggested that the grain boundaries do not act as perfect sources or sinks of point defects,⁵ and the rate of the interface reaction that creates and annihilates vacancies controls creep. Ashby³ suggested that vacancy creation and annihilation occur by the climb of grain-boundary dislocations. Burton⁶ assumed that spiral dislocation climb sources maintained the dislocation density as creep proceeded and dislocations migrated along the grain boundary.

Adapting the treatment of Arzt *et al.*⁷ to densification, one finds that the densification rate is proportional to the square of the driving pressure and that the expression for the driving pressure is modified by the addition of a threshold term, P_{th} . Below this threshold pressure, there is insufficient stress to cause dislocation motion. Modifying Eq. (1) for the hot isostatic pressing of powder compacts gives:

$$P^* = \frac{4\pi^2 P}{aZD} + P_i - P_{th} \quad (3)$$

The existence of a threshold stress can be shown from the experimental data. At constant density, temperature, and grain size

$$dD/dt = QP^{*2} \quad (4)$$

where Q is a constant. Equation (3) indicates that densification can only occur by this interface mechanism if P^* is >0 or $(4\pi^2 P/aZD + P_i) > P_{th}$. When no external pressure is applied, densification is not observed. Thus, P_{th} must be greater than or equal to P_i , otherwise some densification would be observed in this sintering regime. Now

$$dD/dt = QP^{*2} = Q \left[\frac{4\pi^2 P}{aZD} + P_i - P_{th} \right]^2 \quad (5)$$

Putting $n = 4\pi^2/aZD$, and $P_i = P_{th} - P_s$,

$$(dD/dt)^{1/2} = nQ^{1/2} \left(P - \frac{P_i}{n} \right) \quad (6)$$

If the square root of the densification rate is plotted against applied pressure, the graph should intercept the positive x-axis. Figure 2 shows the graphs for four conditions: (1) $D=0.71$, $T=1050^\circ\text{C}$, (2) $D=0.78$, $T=1050^\circ\text{C}$, (3) $D=0.71$, $T=1000^\circ\text{C}$, and (4) $D=0.72$, $T=1000^\circ\text{C}$. At zero densification rate, the plots intercept the pressure axis as predicted. Since the intercept value is equal to $(P_{th} - P_i)/n$, exact values for P_{th} cannot be obtained from these data without knowledge of P_i for these four conditions. These were calculated using the equations derived by Arzt and co-workers.^{3,8} Table I shows the values for the threshold stress. As expected, these values decrease with both increasing fractional density and increasing temperature.

Interface-controlled diffusional creep has been found in Al_2O_3 ,⁹ UO_2 ,¹⁰ Fe_2O_3 ,¹¹ and MgO .¹² For example, Cannon *et al.*⁹ reported a threshold stress of 13.8 MPa for

1.2- μm grain size Al_2O_3 doped with 0.25% MgO . The strain rate also varied with the square of the stress for both pure and MgO -doped Al_2O_3 at strain rates below 10^{-3} s^{-1} . These data suggest that the mechanism of densification may also be interface-controlled in the latter stage of the densification ($D > 0.90$) of alumina and therefore could be the rate-controlling mechanism over most of the densification range ($D = 0.65$ to 1.0).

ACKNOWLEDGMENTS

The authors wish to thank Dr. A. J. Markworth for helpful technical discussions and M. L. E. Muttart for performing the experimental work.

REFERENCES

- M. P. Harmer and R. J. Brook, "The Effect of MgO Additions on the Kinetics of Hot Pressing in Al_2O_3 ," *J. Mater. Sci.*, **15**, 3017-24 (1980).
- A. E. Paladino and R. L. Coble, "Effect of Grain Boundaries on Diffusion-Controlled Processes in Aluminum Oxide," *J. Am. Ceram. Soc.*, **46** [3] 133-36 (1963).
- E. Arzt, M. F. Ashby, and K. E. Easterling, "Practical Applications of Hot Isostatic Pressing Diagrams: Four Case Studies," *Metall. Trans. A*, **14A**, 211-21 (1983).
- W. R. Cannon, "Mechanisms of Creep in High Temperature Alumina", Ph. D. Thesis, Stanford University, 1971.
- M. F. Ashby, "On Interface Reaction Control of Nabarro-Herring Creep and Sintering," *Scr. Metall.*, **3** [11] 837-42 (1969).
- B. Burton, "Interface Reaction Controlled Diffusional Creep: A Consideration of Grain Boundary Dislocation Climb Sources," *Mater. Sci. Eng.*, **10** [1] 9-14 (1972).
- E. Arzt, M. F. Ashby, and R. A. Verrall, "Interface Controlled Diffusional Creep," *Acta Metall.*, **31** [12] 1977-89 (1983).
- E. Arzt, "The Influence of Increasing Particle Coordination on the Densification of Spherical Powders," *Acta Metall.*, **30**, 1883-90 (1982).
- R. M. Cannon, W. H. Rhodes, and A. H. Heuer, "Plastic Deformation of Fine Grained Alumina I," *J. Am. Ceram. Soc.*, **63** [1-2] 46-53 (1980).
- B. Burton and G. L. Reynolds, "Diffusional Creep of Uranium Dioxide: Its Limitation by Interfacial Processes," *Acta Metall.*, **21** [8] 1073-78 (1973).
- A. G. Crouch, "High Temperature Deformation of Polycrystalline Fe_2O_3 ," *J. Am. Ceram. Soc.*, **55** [11] 558-63 (1972).
- E. M. Passmore, R. H. Duff, and T. Vasilos, "Creep of Dense Polycrystalline Magnesium Oxide," *J. Am. Ceram. Soc.*, **49** [11] 594-600 (1972).

APPENDIX E

DISCUSSION OF "PRACTICAL APPLICATIONS OF HOT-ISOSTATIC
PRESSING DIAGRAMS: FOUR CASE STUDIES"

Reprinted from

Metallurgical Transactions, vol. 16A,
pp. 1903-1904 (1985)

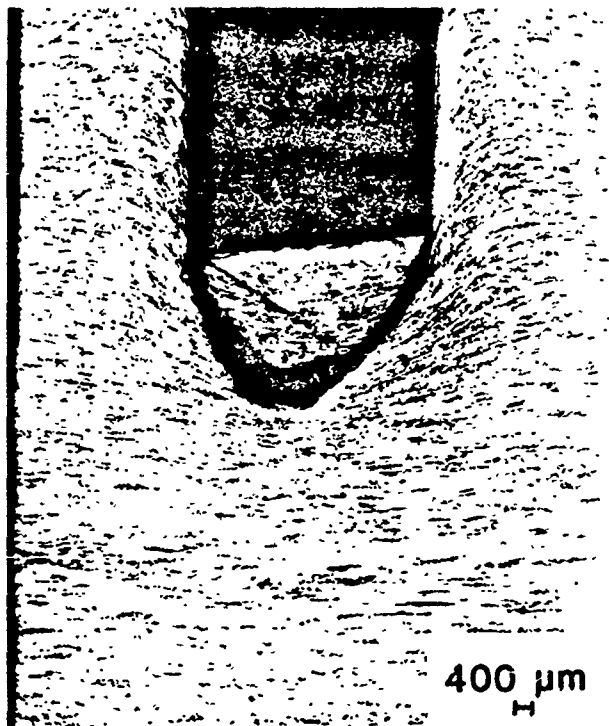


Fig 9—Metallographic section of impacted semi-infinite plate of hardness 150 HV. Impact velocity 325 ms^{-1} . Magnification 6.8 times.

formation of a dead zone below the compressed region. In comparing Figures 1 and 9, it is apparent that a prerequisite for shear band initiation was some degree of acceleration of the section of plate between the advancing projectile and the distal boundary of the target, consistent with the slip line field model proposed by Backman and Finnegan² which employed a minimum plastic strain rate criterion for shear band formation. The shear stress concentrating effect of the projectile geometry was therefore not in itself sufficient for shear band initiation.

This work was carried out at the Materials Research Laboratories, Maribyrnong, Victoria, Australia.

REFERENCES

- 1 G B Olson, J F Mescall, and M Azrin in *Shock Waves and High Strain Rate Phenomena in Metals*, M. A. Meyers and L E Murr, eds., Plenum Publishing Co., New York, NY, 1981, ch. 4
- 2 M E Backman and S A Finnegan in *Metallurgical Effects at High Strain Rates*, R. W Rohde, B M Butcher, J. R. Holland, and C. H. Kames, eds., Plenum Publishing Co., New York, NY, 1973, pp 531-41
- 3 H. C. Rogers *Ann. Rev. of Materials Science*, 1979, vol 9, pp 283-311
- 4 H C Rogers "Material Factors in Adiabatic Shearing and the Implications for Analysis," in *Proc. Symposium on Adiabatic Shear*, Materials Research Laboratories, Australia, 1979, pp 1-26
- 5 J F. Velez and G W Powell *Wear*, 1981, vol 66, pp 367-78.
- 6 Y Me-Bar and D. Shechtman *Materials Science and Engineering*, 1983, vol 58, pp 181-88
- 7 A L Wingrove *Metall Trans*, 1973, vol 4, p 1829
- 8 R L Woodward, B.J. Baxter, and N V Scarlett in *Third Oxford Conference on the Mechanical Properties of Materials at High Strain Rates*, University of Oxford, England, April 1984, p 525
- 9 J A Zukas in *Impact Dynamics*, J A Zukas, T Nicholas, H F Swift, B Greszczuk, and D R Curran, eds., John Wiley and Sons, New York, NY, 1982, ch. 5, p 162.
- 10 T A Stock and K R L Thompson *Metall Trans*, 1970, vol 1, p 219

Discussion of "Practical Applications of Hot-Isostatic Pressing Diagrams: Four Case Studies"*

J. KEVIN McCOY

A recent paper by Arzt, Ashby, and Easterling¹ describes a theory of densification by hot-isostatic pressing. The purpose of this note is to point out an error that was made early in the mathematical development which affected some of the subsequently obtained results.

Arzt, Ashby, and Easterling use two distinct geometrical descriptions of densification. Since these two descriptions are mathematically equivalent, Arzt *et al.* switch from one to the other as best suits the aims of clarity and mathematical convenience. However, it is necessary to keep firmly in mind which description is currently in use.

The first description I will call the "growing-sphere model". This is a relatively new approach, having been pioneered by Arzt.² The growing-sphere model is illustrated in Figure 1: a group of spherical particles is assumed to grow around fixed centers. As the particles grow, they will impinge on one another. Arzt² has treated this effect in two ways; following Arzt, Ashby, and Easterling,¹ I will discuss only one of these. In this model, it is assumed that matter is forced out of the contact region to form a localized neck, while away from necks, the particle radius and spherical geometry are unaltered. Therefore, if the particles grow from a radius R to a radius R' , the volume of each particle increases from $4\pi R^3/3$ to $4\pi R'^3/3$. Since the particles grow around fixed centers, the relative density increases from its initial value D_0 to D , where

$$\frac{D}{D_0} = \left(\frac{R'}{R}\right)^3 \quad [1]$$

This is equivalent to Eq. [1] of Arzt, Ashby, and Easterling.

The second description I will call the "colliding-sphere model". This is the standard description of densification, used, for example, by Wilkinson and Ashby.³ The colliding-sphere model is illustrated in Figure 2. In this treatment, the spherical particles are assumed to have fixed volume, but the particle centers are assumed to move so that each particle approaches every other particle. One might say that the particle volumes remain constant while space shrinks. This wording points out the mathematical equivalence of the growing-sphere and colliding-sphere models; they differ only by a dilatation of space.

Using the colliding-sphere model, suppose that densification reduces the center-to-center distance of two initially tangent particles from $2R$ to 2γ while increasing the relative density from D_0 to D . Since the colliding-sphere model assumes a uniform contraction of the group of particles,

*E. ARZT, M. F. ASHBY, and K. E. EASTERLING *Metall Trans A*, 1983, vol 14A, pp 211-21

J. KEVIN McCOY is Research Scientist, Battelle-Columbus Laboratories, 505 King Avenue, Columbus, OH 43201-2693

Discussion submitted April 18, 1985

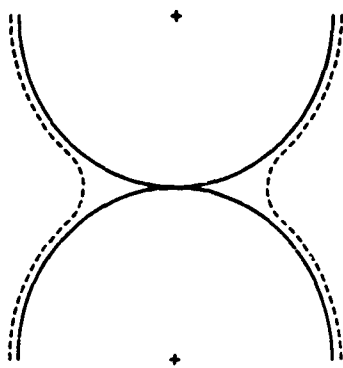


Fig 1—Expanding-sphere model. Two initially tangent particles (solid lines) expand about fixed centers, impinging on one another and forcing matter out of the contact region to form a neck (dotted lines)

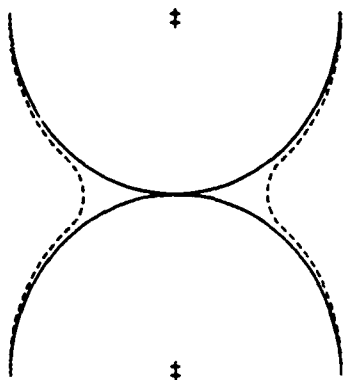


Fig 2—Colliding-sphere model. Two initially tangent particles (solid lines) move toward each other. Matter is forced out of the contact area to form a neck.

one obtains

$$\frac{D}{D_0} = \left(\frac{R}{y}\right)^3 \quad [2]$$

Of the variables in Eq. [2], only y and D change during the densification process. Therefore, differentiation of Eq. [2]

with respect to time produces

$$\frac{1}{D_0} \frac{dD}{dt} = -3R^3 y^{-4} \frac{dy}{dt} \quad [3]$$

where t is time. Applying Eq. [2] and rearranging terms, one may conclude that

$$\frac{dD}{dt} = \frac{-3D}{R} \left(\frac{D}{D_0}\right)^{1/3} \frac{dy}{dt} \quad [4]$$

In contrast, Eq. [2] of Arzt, Ashby, and Easterling is

$$\frac{dD}{dt} = \frac{3(D^2 D_0)^{1/3}}{R} \frac{dy}{dt} \quad [5]$$

Integrating Eq. [5] gives

$$\frac{D}{D_0} = \left(\frac{y}{R}\right)^3 \quad [6]$$

rather than Eq. [2] above. Use of Eq. [6] produces a result that is incorrect in both sign and functional form. Upon comparison of Eqs. [1] and [6], one is tempted to speculate that the error resulted from a confusion between the colliding-sphere and growing-sphere models.

This error appears to be propagated through the paper. Since the paper contains several parallel derivations, however, the effects are apparently limited to Arzt, Ashby, and Easterling's Eq. [16] and the various figures. Apart from the incorrect sign, the quantitative effects of the error are rather small; the magnitudes of the densification rates given by Eq. [4] and by Arzt, Ashby, and Easterling's Eq. [2] never differ by more than about 30 pct.

Support of this work by the Air Force Office of Scientific Research is gratefully acknowledged.

REFERENCES

- 1 E. Arzt, M. F. Ashby, and K. E. Easterling *Metall. Trans. A*, 1983, vol. 14A, pp. 211-21.
- 2 E. Arzt *Acta Metall.*, 1982, vol. 30, pp. 1883-90.
- 3 D. S. Wilkinson and M. F. Ashby *Acta Metall.*, 1975, vol. 23, pp. 1277-85.

APPENDIX F

DENSIFICATION BY INTERFACE-REACTION CONTROLLED
GRAIN-BOUNDARY DIFFUSION

Submitted to
Acta Metallurgica

DENSIFICATION BY INTERFACE-REACTION CONTROLLED GRAIN-BOUNDARY DIFFUSION

J. KEVIN McCOY and ROGER R. WILLS

Battelle, 505 King Avenue, Columbus, Ohio 43201-2693, USA

Abstract--The densification of a fine-grained, high-purity aluminum oxide powder under hot isostatic pressing (HIP) has been found to occur by interface-reaction controlled grain-boundary diffusion. We discuss geometries and dislocation mechanics for this process for both the initial and final stages of densification and develop constitutive equations for densification rate as a function of density, materials constants, and experimental parameters. The model is used to explain the results of several HIP experiments at pressures of 34 to 102 MPa and temperatures of 1273 to 1423 K. Sources of variation from sample to sample are discussed. An analysis is made of the sensitivity of the model to its adjustable parameters. Alternative explanations for the experimental data are discussed and found to be inadequate.

1. INTRODUCTION

A number of mechanisms have been proposed to describe densification during sintering and hot isostatic pressing (HIP). Most of the theoretical treatments invoke either a simple diffusion or dislocation mechanism for material transport. When we analyzed densification data

for aluminum oxide from a series of HIP experiments in which both temperature and pressure were monitored, we found that the data could not be adequately explained in terms of either theory, but that they could be explained in terms of interface-reaction controlled grain-boundary diffusion [1]. Both dislocation and diffusion elements are contained in this mechanism in that mass transport occurs by diffusion but is limited by the mobility of grain-boundary dislocations. The concept of interface-reaction controlled grain-boundary diffusion is not particularly new, having been proposed by Burton [2] in 1972 and given a thorough development in a recent review by Arzt, Ashby, and Verrall [3], but it has apparently been applied only to creep or deformation.

In this paper, we apply the theory of interface-reaction controlled grain-boundary diffusion to describe densification of a porous solid. Following standard practice [4], we divide densification into two stages. The initial stage is described as a random packing of spherical particles; this model is applied at fractional densities of 0.64 to 0.9. The final stage is described by an isolated spherical pore centered in a spherical shell; this model is used for fractional densities greater than 0.9. We develop appropriate geometries for both stages of densification and then briefly review the dislocation kinetics associated with the mechanism. The model is expressed in a form suitable for fitting to experimental data and applied to explain the densification kinetics of a high-purity aluminum oxide for a range of temperatures, pressures, and specimen porosities.

2. INITIAL STAGE

In this section, we develop a model for the initial stage of densification. We begin by describing the geometry of a neck between two particles and use the results to calculate the driving force for densification. Finally, the driving force and the mechanism of interface-reaction controlled grain-boundary diffusion are used to calculate the densification rate.

The most important geometrical quantities for the description of an interparticle neck are illustrated in Fig. 1: R is the particle radius, $2y$ is the particle center-to-center distance, x is the neck radius, and w is the axial radius of curvature of the neck. These quantities reflect a standard model of neck geometry: two spherical particles impinge upon each other, and matter is transferred from the contact area to a localized neck while the remainder of the surface of the spheres remains unaltered. The surface of the neck is assumed to be a portion of a circular torus that is tangent to both spheres. The minor radius of the torus is w and the major radius is $x+w$. For given values of R and y , x and w are specified by the solution to two equations. The first equation follows from the Pythagorean theorem:

$$y^2 + (x+w)^2 = (R+w)^2 \quad (1)$$

or

$$w = \frac{x^2 + y^2 - R^2}{2(R-x)} \quad (2)$$

The second equation for x and w specifies that the volume of matter removed from the spheres must equal the volume of matter deposited in

the neck. It is a straightforward exercise in calculus to show that this equation is

$$\begin{aligned} \frac{2}{3}(R-y)^2(2R+y) = & \quad (3) \\ & R^2w\cos^2\theta\sin\theta - w\sin\theta(R^2-y^2) \\ & + w^3\sin^3\theta - 2(x+w)w^2(\theta - \cos\theta\sin\theta) \end{aligned}$$

where

$$\theta = \arctan[y/(x+w)]. \quad (4)$$

Due to the complexity of equation (3), Arzt [5] has proposed the approximation

$$x^2 = n(R-y)R \quad (5)$$

where n is a numerical constant. Arzt suggested the value $n = 11$, but we have chosen to use $n = 11.4$ since this value gives a slightly better fit. We have used equations (2) and (5) to provide a description of torus geometry. As evidence of the accuracy of equation (5), we give in Fig. 2 a comparison of the values of x and w obtained by using the rigorous treatment of equation (3) and the approximation of equation (5). The agreement between the two treatments is probably better than that between either treatment and physical reality.

With this description of neck geometry, we can find p^* , the effective contact pressure between the two particles for the initial stage, which produces a climb force on grain-boundary dislocations and thus acts as the driving force for densification. Following Molerus [6] and Arzt, Ashby, and Easterling [7], we write the effective contact pressure as

$$p^* = \frac{4\pi R^2 \rho}{aZD} + p_s - p_{th} \quad (6)$$

where p is the externally applied pressure, a is the average neck area, Z is the coordination number, D is the fractional density, p_s is the contact pressure due to surface tension, and p_{th} is a threshold pressure for the motion of grain-boundary dislocations. In our experiments, the sample was thoroughly outgassed before encapsulation, and the capsules were welded in vacuum, so the effect of gas trapped in the pores is not included in equation (6).

To evaluate the effects of coordination number and contact area in equation (6), it is mathematically convenient to use the approach of Arzt [5]. Arzt describes densification not as a packing of spheres that approach each other but as a packing of stationary spheres that grow fictitiously. If the spheres grow from a radius R to a radius R' , the increase in the volume of the spheres will cause the fractional density to increase from its initial value D_0 to a new value D , where

$$D/D_0 = (R'/R)^3 \quad (7)$$

As the spheres grow, two types of geometrical changes occur. First, the initial contact points grow into necks as the growing spheres impinge on each other. We have assumed that all displaced material remains in the necks, while, away from the necks, the particles remain spherical with radius R' . Second, as sphere growth continues, the spheres also begin to form contacts with additional spheres that they did not touch in the original packing. Using radial distribution functions for a random dense packing developed by Scott [8] and Mason [9], Arzt developed the following approximate equation for the coordination

number

$$Z = Z_0 + c(R'/R - 1) \quad (8)$$

where $Z_0 = 7.3$ and $c = 15.5$. Using this radial distribution function and equation (5) for the area of a neck, the average neck area is [5]

$$a = n(Z_0(R'-R)R + c(R'-R)^2/2)R/ZR'. \quad (9)$$

Equation (9) includes a correction so that it is applicable to spheres of radius R rather than R' . Using equations (8) and (9), the effect of external pressure in equation (6) may be evaluated.

Following Arzt, Ashby, and Easterling [7], the contact pressure due to surface tension is

$$P_s = \gamma \left[\frac{1}{w} + \frac{1}{x} \right] \quad (10)$$

where γ is the surface tension. The average neck area is known from equation (9), so the average neck radius is

$$x = \sqrt{a/\pi} \quad (11)$$

while the axial radius of curvature of the neck is given by equation (2).

The threshold pressure for motion of a grain-boundary dislocation is uncertain, since it depends on the Burgers vector of the dislocations and the type of dislocation source. We have chosen to use the approach of Arzt, Ashby and Verrall [3]. Following their treatment, the threshold stress for grain-boundary dislocation motion is

$$P_{th} = \frac{\sqrt{2}\alpha_0 G b_b}{2x} \quad (12)$$

where $\alpha_0 = 0.2$ is a constant that reflects the relative amount by which

the length of a dislocation fluctuates as it moves.

The presence of an effective contact pressure will cause densification and produce changes in the neck geometry. As densification proceeds, the center-to-center distance of two initially tangent particles will change with rate $d2y/dt$. As discussed below in the section on dislocation mechanics, a change in y results from the motion of grain-boundary dislocations; the passage of one dislocation across the entire neck reduces the center-to-center distance $2y$ by b_n where b_n is the component of the Burgers vector normal to the grain boundary. For the case in which several dislocations are moving together, the number of dislocations that will pass a given point on the grain boundary in unit time is $v\rho$. Thus the rate of change of the center-to-center distance of two particles is

$$\frac{d2y}{dt} = -v\rho b_n. \quad (13)$$

The final step of the model is to obtain the densification rate. If it is assumed that the sample starts as a packing of tangent spherical particles and that the particles approach each other as densification proceeds, it is clear from geometry that [10]

$$D = D_0 (R/y)^3 \quad (14)$$

where D_0 is the initial fractional density and D is the current fractional density. By differentiating equation (14), one obtains

$$\frac{dD}{dt} = -\frac{3D}{2R} \left[\frac{D}{D_0} \right]^{1/3} \frac{d2y}{dt}. \quad (15)$$

An expression for dD/dt in terms of experimental variables is given in equation (27).

3. FINAL STAGE

As a material approaches full density, it is no longer appropriate to describe interparticle contacts in terms of distinct necks, and it becomes appropriate to describe the porosity in terms of isolated pores. In this section, we develop a model for this stage of densification. We first describe the geometry of the grains and pores, then determine the driving force for densification, and finally obtain the densification rate.

The geometry of the pores and grains is similar to that used by Arzt, Ashby, and Easterling. It is assumed that the grains take the shape of truncated octahedrons with spherical pores of radius r located at each vertex. Each truncated octahedron has 24 vertices, and four grains meet at each vertex so there are, on the average, six pores per grain. The volume of each grain is assumed to be $4\pi R^3/3$, as in the initial stage. Since there are six pores per grain, the density, pore radius and equivalent spherical grain radius are related by

$$1-D = \frac{6r^3}{R^3+6r^3}. \quad (16)$$

Following Coble [11], we may simplify the geometry for the purposes of calculating densification rate by taking a spherical shell of material around each pore. We assign a volume of matter $2\pi R^3/9$ (1/6 of a grain) to each pore, so the shell radius R_s is given by

$$R_s^3 = \frac{R^3}{6} + r^3. \quad (17)$$

The effective pressure or driving force for densification may be obtained by balancing the forces imposed on the shell against the stresses in the shell. Suppose that we make an imaginary cut through the center of the shell on the xy plane. The total force on one hemisphere in the z direction is

$$\pi R_s^2 p + 2\pi r\gamma - \pi(R_s^2 - r^2)\sigma_{\theta\theta} = 0. \quad (18)$$

The first term is due to the externally applied pressure, the second is from the surface tension of the pore, and the third results from the tangential stress within the sphere which balances the forces applied to the surface of the sphere. Note that $\sigma_{\theta\theta}$ is treated as a constant in equation (18). This is justified if we assume that the motion of dislocations is at steady state. As discussed below, the density and speed of the dislocations are both proportional to the driving force. But at steady state, v_p is independent of position, so $\sigma_{\theta\theta}$ is also independent of position.

In addition to the tangential stress, the driving force for densification also involves a threshold term, just as for the initial stage. For hot isostatic pressing, this is [3]

$$p_{th} = \frac{\sqrt{2} \alpha_0 G b_p}{2R} \quad (19)$$

and the net driving force is

$$p^* = \sigma_{\theta\theta} - p_{th}. \quad (20)$$

Differentiating equation (16) with respect to time, we obtain

$$\frac{dD}{dt} = \frac{-3D(1-D)}{r} \frac{dr}{dt}. \quad (21)$$

Furthermore,

$$\frac{dr}{dt} = \frac{1}{4\pi r^2} \frac{dV}{dt} \quad (22)$$

where V is the volume of a pore and $-dV/dt$ is the rate at which matter is removed from the grain boundaries and deposited in the pore:

$$dV/dt = -v\rho b_n \pi (R_S^2 - r^2) n_b, \quad (23)$$

that is, the product of the dislocation flux, the component of the Burgers vector normal to the grain boundary, the area of one planar grain boundary intersecting the pore, and the effective number of boundaries. An expression for dD/dt in terms of experimental variables is given in equation (30).

4. DISLOCATION MECHANICS

In both the initial and final stages, the applied pressure results in a climb force on the grain-boundary dislocations. In this section, we discuss dislocation effects that are common to both stages.

Following Arzt, Ashby, and Verrall [3], the rate at which an individual grain boundary dislocation climbs is

$$v = MF = M\rho^* b_n. \quad (24)$$

Here F is the force per unit length on the dislocation and M is the dislocation mobility. From elementary dislocation theory, it follows that the force on the dislocation is the product of the driving force ρ^* and the component of the Burgers vector normal to the grain boundary b_n .

Applying the results of Cottrell and Jaswon [12] and Cottrell [13], Arzt, Ashby, and Verrall obtained the following expression for grain-boundary dislocation mobility limited by solute drag:

$$M = \frac{D_s \Omega}{\beta k T b_b^2 C_0} \quad (25)$$

In this equation, C_0 is the concentration of solute in the lattice, and the concentration in the solute atmosphere of the dislocation is increased by a factor of β to βC_0 . D_s is the diffusivity of the solute in the lattice, Ω is the effective atomic volume of the solute, kT has its usual meaning, and b_b is the Burgers vector of the grain-boundary dislocation.

To complete the description of a grain-boundary with dislocations we need only an expression for the density of dislocations. This problem has been studied by Burton [2] and by Arzt, Ashby, and Verrall [3]. Although different approaches were used, their results are in substantial agreement. The result of Arzt et al. is

$$\rho = \frac{C_1 p^*}{G b_b} \quad (26)$$

where C_1 is a constant (about 0.5), G is the shear modulus, and b_b is the length of the Burgers vector.

5. EXPERIMENTAL RESULTS

The development of the theory of densification presented above was prompted by failure of standard theories to explain the data

reported below. The experimental technique used in obtaining the data has been described in detail elsewhere [14], so only a brief summary will be given here. Cylindrical samples of Reynolds RC-HP-DBM alumina were encased in close-fitting AISI 316 stainless steel capsules. The samples were subjected to HIP at temperatures ranging from 1273 K to 1423 K and at pressures ranging from 34 MPa to 102 MPa. Throughout densification, continuous records of temperature and pressure were kept. In addition, a two-probe dilatometer was used to produce a continuous record of the diameter of the sample. The records of temperature and diameter, along with a description of the changes in geometry of the sample, were used to calculate a record of density as a function of time during HIP. This procedure produces far more information from each experiment than does conventional HIP practice, which provides only a final density. In addition to providing a much larger body of data, the dilatometer technique provides the additional advantage that all the data obtained from a given experiment can be compared to theory without consideration of sample-to-sample or run-to-run variations. To further increase the amount of information produced during each experiment, the temperature and/or pressure were often changed during an experiment. This allowed us to determine activation energies and pressure exponents from a single experiment.

For the purposes of fitting the theory to the experimental data, it is convenient to collect the variables that are essentially constant throughout the experiment. If this is done, we may combine equations 14, 16, and 24 to 26 and write for the initial stage

$$\frac{dD}{dt} = D \left[\frac{D}{D_0} \right]^{1/3} \frac{p^* \exp(-E_s/RT)}{GT} f \quad (27)$$

where

$$f = \frac{3}{2R} \left[\frac{b_n}{b_b} \right]^2 \frac{C_1 D_s^0 \Omega}{b_b \beta k C_0} \quad (28)$$

and the solute diffusivity is assumed to be given by

$$D_s = D_s^0 \exp(-E_s/RT) \quad (29)$$

Similarly, we may combine equations 21 to 26 and write for the final stage

$$\frac{dD}{dt} = \left[\frac{3}{4} \right]^{1/3} D^{4/3} (1-(1-D)^{2/3}) p^* \frac{\exp(E_s/RT)}{GT} n_b f \quad (30)$$

using the same definition for f . The following data were used with equations (27) and (30). The surface energy was taken to be $\gamma = 1 \text{ J/m}^2$ [7]. The activation energy for solute diffusion E_s was determined experimentally by changing the temperature during the course of the run. A value of $E_s = 290000 \text{ J/mol}$ was measured. Values of the shear modulus G were obtained from the equation

$$G = 12.382 \times 10^9 (1838.5 - T)^{1/3} \text{ Pa}, \quad (31)$$

where T is the temperature in kelvins, which provides a good fit to the data of Ryshkewitch [15]. The value of n_b , the effective number of grain boundaries meeting at a pore, was derived from the assumption that the grain shape is a truncated octahedron. In this geometry, four regular hexagonal faces and two square faces meet at each vertex, so the total of the angles of all the faces meeting at the vertex is 660° . Since a single planar grain boundary corresponds to an angle of 360° , n_b

= 11/6.

With these data, it is possible to use the temperature and pressure records to integrate the kinetic equations for densification to obtain a theoretical record of density as a function of time. Results of such calculations are given in Figs. 3-6. We present records of temperature, pressure, and density for six experiments, and we compare the experimental records of density with the results of theoretical calculations. Equation (27) was used for fractional densities up to 0.90, while equation (30) was used for higher densities. The abrupt change in equations corresponds to an abrupt change in the geometry of the model, from highly connected open porosity to closed porosity, and a marked discontinuity in the densification rate might be expected. In fact, the discontinuity is small, and, as shown in Figs. 3-6, it is usually quite difficult to see in plotted results. The small size of the discontinuity suggests that there is little to be gained by modeling an intermediate stage of densification in which "cylindrical pores" predominate. Neglecting the intermediate stage is in accord with the practice of Swinkels, Wilkinson, Arzt, and Ashby [4], who have argued against the use of an intermediate stage model.

The integration was carried out numerically, using an adaptive third-order Runge-Kutta method [16]. From tests with varying step sizes, it is estimated that the absolute global error in the theoretical value of D due to the integration is never larger than 0.0001, which is much smaller than the expected error in experimental values of D .

The only adjustable parameters were the initial value of the density and the kinetic factor f . For each experiment, a value of f was

chosen to provide a good fit between theoretical and experimental density histories, while the initial fractional density was taken as the value measured by immersion, which is not exactly equal to the density given by the dilatometer, due to experimental error. In some cases, the immersion density was smaller than that of a random dense packing of spheres, D_0 , and numerical integration starting at the immersion density was not possible due to a singularity in equation (27) at $D = D_0$. In those cases, an initial fractional density of 0.641 was used.

The exact value of the initial density used in integration actually has a only very small effect on the calculated density record, since, in the low density range, the densification rate drops rapidly as density increases. As an illustration of this, consider two samples that are being HIPped under identical, unchanging conditions, and assume that the two samples are identical except that the initial density of one sample is higher than that of the other. It will take a certain amount of time for the less dense sample to reach the initial density of the denser sample. Since the samples are densifying under identical conditions, the densities of the samples will be the same function of time except for the time offset just mentioned. Although the time offset remains constant, the densification rate drops so that the difference between the densities of the two samples decreases as time goes on. As a qualitative illustration of the effect of changing the initial density, consider the results shown in Fig. 7. The calculated density history of Fig. 3 is replotted, along with the results of a calculation that differed only in the value of the initial density. It is clear that the rather large initial difference in density quickly

becomes negligible. Note also that since the temperature and pressure were not constant in this calculation, so the time offset between the two curves is not constant.

6. DISCUSSION

In the preceding discussion, the values of f used in fitting the theoretical equations to the data were presented without any justification that the values are reasonable. To show that the values are indeed reasonable, let us estimate the values of the variables that comprise f . From scanning electron photomicrographs [17], it is estimated that $R = 0.35 \times 10^{-6} \text{ m}$. Following Arzt, Ashby, and Verrall [3], we may take $b_b/b_{11} = \sqrt{2}$, $C_1 = 0.5$, $\beta = 10$, and $b_b = 1.59 \times 10^{-10} \text{ m}$, where the value of b_b is one third of the Burgers vector for slip on the $\{0001\} \langle 11\bar{2}0 \rangle$ basal system. A reasonable estimate of the effective atomic volume of the solute is $\Omega = 2.15 \times 10^{-29} \text{ m}^3$, which is half the volume of the formula unit. Although the solute that controlled densification was not identified, chemical analysis of the powder revealed several impurities for which it is reasonable to use an atom fraction of solute of $C_0 = 3 \times 10^{-7}$. The value of D_S^0 is unknown, since it is not known what solute might be responsible for controlling the motion of grain-boundary dislocations. However, by combining the estimates above with $f = 3 \times 10^4 \text{ KPa}^{-1} \text{ s}^{-1}$, a typical value obtained by curve-fitting, one obtains a value of $D_S^0 = 9 \times 10^{-10} \text{ m}^2/\text{s}$. This is within the range of values of preexponential factors for solute diffusion in alumina as com-

piled by Freer [18], so we may conclude that the values of f are also reasonable.

From the captions of Figs. 3-6, it will be observed that the values of f used in fitting theory to experiment vary by a factor of seven. As in illustration of the effect of a large change in f , in Fig. 8 we have replotted the theoretical curve of Fig. 5 along with a similar curve for a value of f five times as large. The two curves are markedly different.

Since the variation in f may seem to be larger than might have been expected, it is appropriate to discuss possible causes of variation in f . There is no evident correlation between the value of f and the experimental conditions, so we have attributed the variation in f to differences between samples. The two factors in f that would appear to be subject to the greatest variation are C_0 and D_S^0 . Since the powder was blended before being formed into samples, it is not expected that sample-to-sample variation of C_0 would explain all of the variation in f . However, variations in D_S^0 are expected to be much larger, since solute diffusivities in ceramics often depend very sensitively on the concentrations of other impurities. Besides C_0 and D_S^0 , large variations in f may also arise from relatively small variations in E_s . In our calculations, we used a single activation energy for all samples. If the actual value of E_s for the sample differed from the value used in the calculation, the inaccuracy would show up, greatly enlarged, in $\exp(E_s/RT)$. However, since f was the only kinetic fitting parameter, changes in $\exp(E_s/RT)$ would appear as changes in f . The effects of a change in activation energy can be quite significant; a variation of 9%

in E_s (with D_s^0 held constant) would not be considered large, but it would be sufficient to explain the entire range of values of f . Therefore, we conclude that sample-to-sample variations are sufficient to explain the variation on f .

In Figs. 3-6, it will be observed that the theoretical and experimental curves are generally in excellent agreement up to a fractional density of about 0.9 but that the theory overestimates the densification rate beyond this point. One possible explanation for this fact is that the mechanism of densification changes at this density. But the densification mechanism is determined primarily by the temperature and the driving force, and at high densities the driving force is a weak function of density. Therefore, it is unlikely that the mechanism would change, under constant temperature and applied pressure. A more plausible but less welcome explanation is that the pore-and-shell model described above does not adequately describe the final stage of densification. This hypothesis is supported by the fact that similar overestimates of the densification rate occur in pore-and-shell models of the final stage for other mechanisms. Additional work on this question is in progress.

While the agreement between theory and experiment is generally excellent except at high density, it is appropriate to ask if some other densification mechanism could also explain the data. Considering the low temperature and small grain size of this material, it might be supposed that a simple grain-boundary diffusion mechanism might explain the data. However, this mechanism has a pressure exponent of 1: the densification rate is linearly dependent on the driving force for

densification, and analysis of data from experiments with changing pressure, such as that presented in Figs. 5 and 6, shows a pressure exponent of about 2 [1]. Another hypothesis might be that some lattice dislocation mechanism is responsible for densification, but models of dislocation plasticity generally give stress exponents of at least 3 [19]. Also, most of the experiments were performed at temperatures of 1273 to 1323 K. It is expected that significant slip could occur only on the basal systems at these temperatures [20], and it is difficult to imagine how significant densification could result with only two active independent slip systems. Furthermore, the activation energy for power-law densification, which is generally thought to have a dislocation mechanism, is 477 kJ/mol [21], while the observed activation energy was 290 kJ/mol. This discrepancy is too large to be explained by experimental error. A third possible explanation of the data is that two (or more) simultaneous mechanisms are at work, and that the observed pressure exponent of 2 is the result of two mechanisms with pressure exponents of (say) 1 and 3. Such an argument would be difficult to defend. Theoretical models of densification that give rise to pressure exponents of 3 or more generally invoke lattice dislocation mechanisms, and, as argued above, lattice dislocations can contribute little to densification at the temperatures used in the experiments since only basal slip can occur. It is therefore concluded that a model of densification by interface-reaction controlled grain boundary diffusion provides the most plausible explanation of the data.

ACKNOWLEDGEMENT

Support of this work by the Air Force Office of Scientific Research is gratefully acknowledged.

REFERENCES

1. R. R. Wills and J. K. McCoy, J. Am. Ceram. Soc. 68, C-95 (1985).
2. B. Burton, Mater. Sci. Eng. 10, 9 (1972).
3. E. Arzt, M. F. Ashby and R. A. Verrall, Acta Metall. 31, 1977 (1983).
4. F. B. Swinkels, D. S. Wilkinson, E. Arzt, and M. F. Ashby, Acta Metall. 31, 1829 (1983).
5. E. Arzt, Acta Metall. 30, 1883 (1982).
6. O. Molerus, Powder Metall. 12, 259 (1975).
7. E. Arzt, M. F. Ashby and K. E. Easterling, Metall. Trans. A 14, 211 (1983).
8. G. D. Scott, Nature 194, 956 (1962).
9. D. Mason, Nature 217, 733 (1968).
10. J. K. McCoy, Metall. Trans. 16A, 1903 (1985).

11. R. L. Coble, J. Appl. Phys. 41, 4798 (1970).
12. A. H. Cottrell and M. A. Jaswon, Proc. Roy. Soc. A199, 104 (1949).
13. A. H. Cottrell, Dislocations and Plastic Flow in Crystals. Oxford (1953).
14. J. K. McCoy, L. E. Muttart and R. R. Willis, Am. Ceram. Soc. Bull. 64, 1240 (1985).
15. E. Ryshkewitch, J. Am. Ceram. Soc. 34, 322 (1951).
16. G. Dahlquist and A. Bjorck, Numerical Methods, p. 346. Prentice-Hall, Englewood Cliffs, New Jersey (1974).
17. L. E. Muttart, private communication (1985).
18. R. Freer, J. Mater. Sci. 15, 803 (1980).
19. F. A. Mohamed and T. G. Langdon, Acta Metall. 22, 779 (1974).
20. D. M. Kotchick and R. E. Tressler, J. Am. Ceram. Soc. 63, 429 (1980).
21. A. E. Paladino and W. D. Kingery, J. Chem. Phys. 37, 957 (1962).

Table of symbols

a	average neck area
b_b	Burgers vector of grain boundary dislocation
b_n	component of Burgers vector of grain boundary dislocation normal to grain boundary
c	derivative of coordination number with respect to R'/R , $c = 15.5$
C_o	atom fraction of solute in bulk
C_1	constant, $C_1 = 0.5$
D	fractional density
D_o	fractional density of random dense packing, $D_o = 0.64$
D_s^o	diffusivity of solute at infinite temperature
D_s	diffusivity of solute
E_s	activation energy for diffusion of solute
F	force per unit length on dislocation
G	shear modulus
k	Boltzmann's constant
M	dislocation mobility
n	constant for neck area in initial stage, $n = 11.4$
n_b	effective number of grain boundaries meeting at a pore
p	external pressure
p^*	driving force for densification
P_s	contact pressure due to surface tension
P_{th}	threshold contact pressure for dislocation motion
R	particle radius
R'	current particle radius in Arzt's growing-sphere description

Table of symbols (continued)

R_s	shell radius
R	gas constant
r	pore radius
T	temperature
t	time
v	dislocation velocity
w	neck axial radius of curvature
x	neck radius
y	half particle center-to-center distance
Z	coordination number
Z_0	coordination number at D_0 , $Z_0 = 7.3$
α_0	constant, $\alpha_0 = 0.2$
β	ratio of solute concentration near dislocation to solute concentration in bulk
γ	surface tension
ρ	dislocation density
Ω	effective atomic volume of solute

Fig. 1. Neck geometry. The two particles are spherical, while the neck is part of a tangent circular torus.

Fig. 2. Comparison of two treatments of neck geometry. Solid curve is for the toroidal neck geometry of Fig. 1 with strict conservation of mass; dashed curve is for the approximation given in equation (5). (a) Relative neck radius (x/R) as a function of relative particle separation (y/R). (b) Relative neck axial radius of curvature (w/R) as a function of relative particle separation (y/R).

Fig. 3. (a) Pressure (solid curve) and temperature (dashed curve) histories. (b) Comparison of experimentally determined density (solid curve) with integration of kinetic equations for densification (dashed curve) with $f = 7. \times 10^4 \text{ KPa}^{-1} \text{ s}^{-1}$.

Fig. 4. (a) Pressure (solid curve) and temperature (dashed curve) histories. (b) Comparison of experimentally determined density (solid curve) with integration of kinetic equations for densification (dashed curve) with $f = 2.8 \times 10^4 \text{ KPa}^{-1} \text{ s}^{-1}$.

Fig. 5. (a) Pressure (solid curve) and temperature (dashed curve) histories. (b) Comparison of experimentally determined density (solid curve) with integration of kinetic equations for densification (dashed curve) with $f = 1. \times 10^4 \text{ KPa}^{-1} \text{ s}^{-1}$.

Fig. 6. (a) Pressure (solid curve) and temperature (dashed curve) histories. (b) Comparison of experimentally determined density (solid curve) with integration of kinetic equations for densification (dashed

curve) with $f = 1.5 \times 10^4 \text{ KPa}^{-1} \text{ s}^{-1}$.

Fig. 7. Effect of initial density on densification history. Temperature and pressure data from Fig. 3 were integrated with $f = 7. \times 10^4 \text{ KPa}^{-1} \text{ s}^{-1}$, but with initial densities of 0.641 (solid curve) and 0.7 (dashed curve).

Fig. 8. Effect of f on densification history. Temperature and pressure data from Fig. 5 were integrated with $f = 1. \times 10^4 \text{ KPa}^{-1} \text{ s}^{-1}$ (solid curve) and $f = 5. \times 10^4 \text{ KPa}^{-1} \text{ s}^{-1}$ (dashed curve).

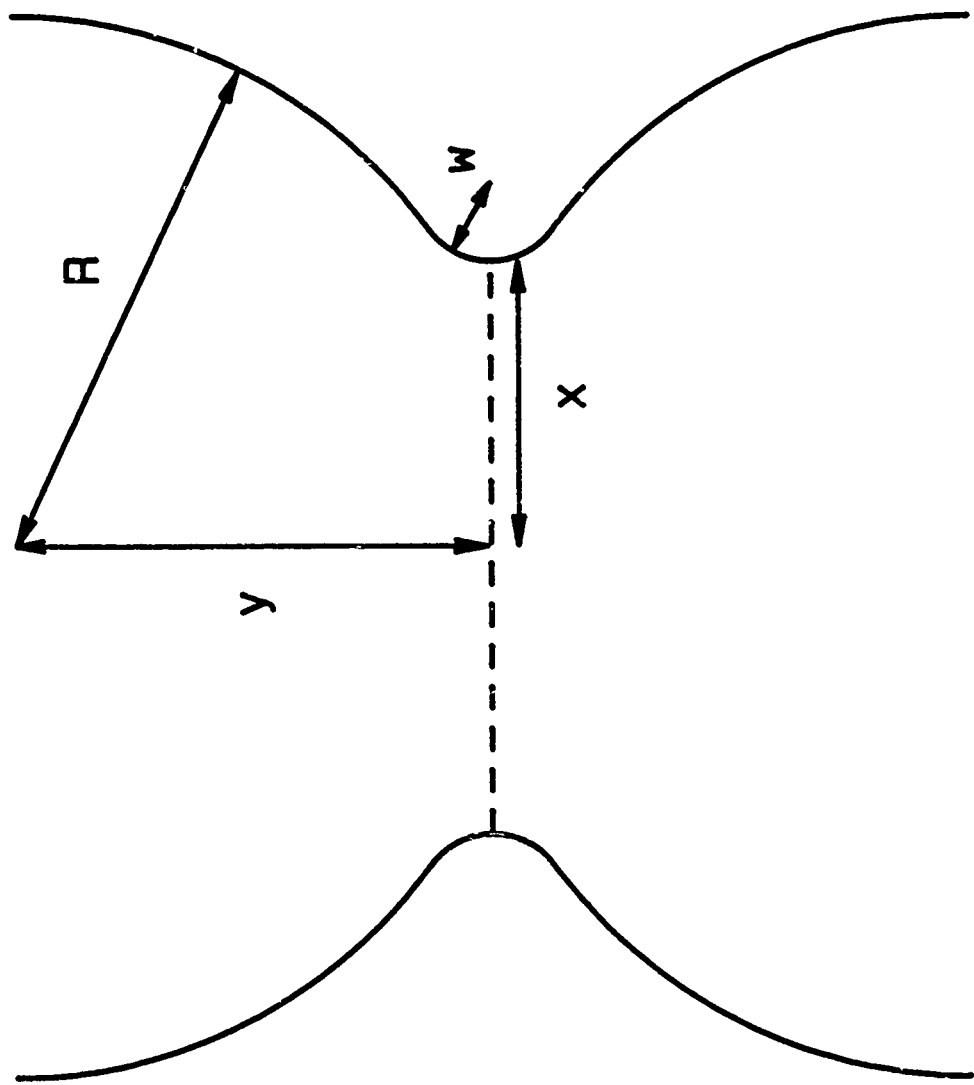


FIGURE 1.

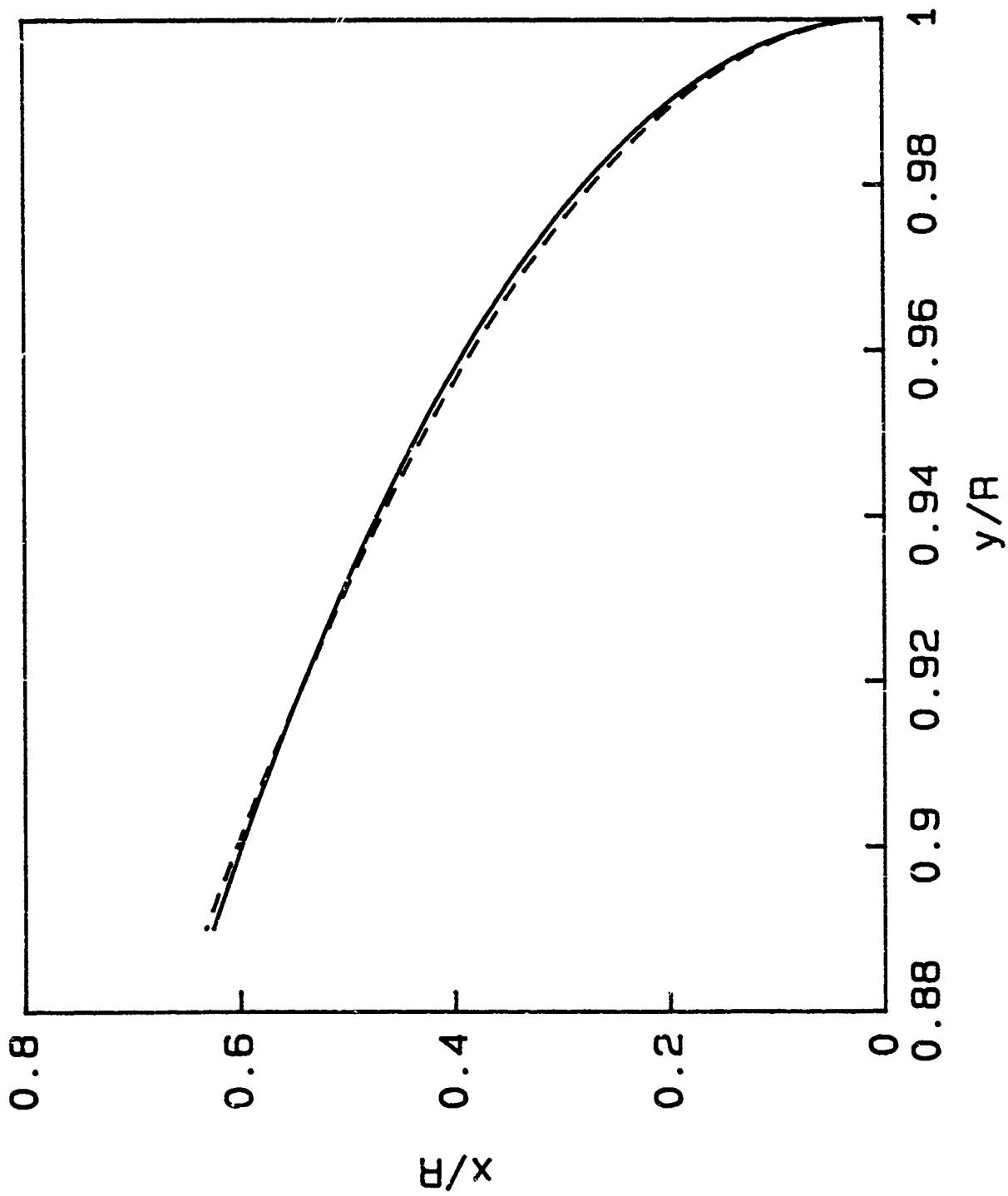


FIGURE 2a.

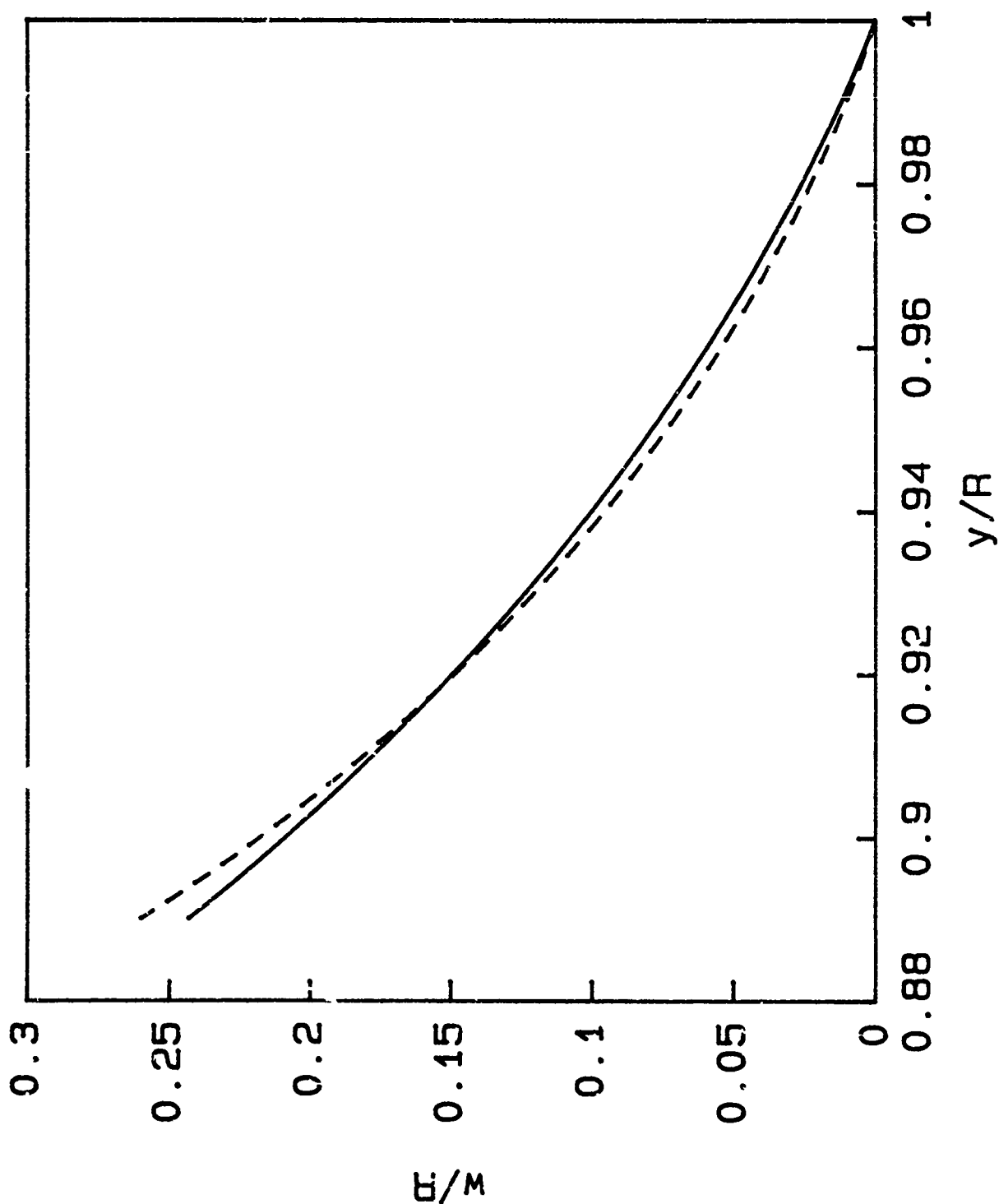


FIGURE 2b.

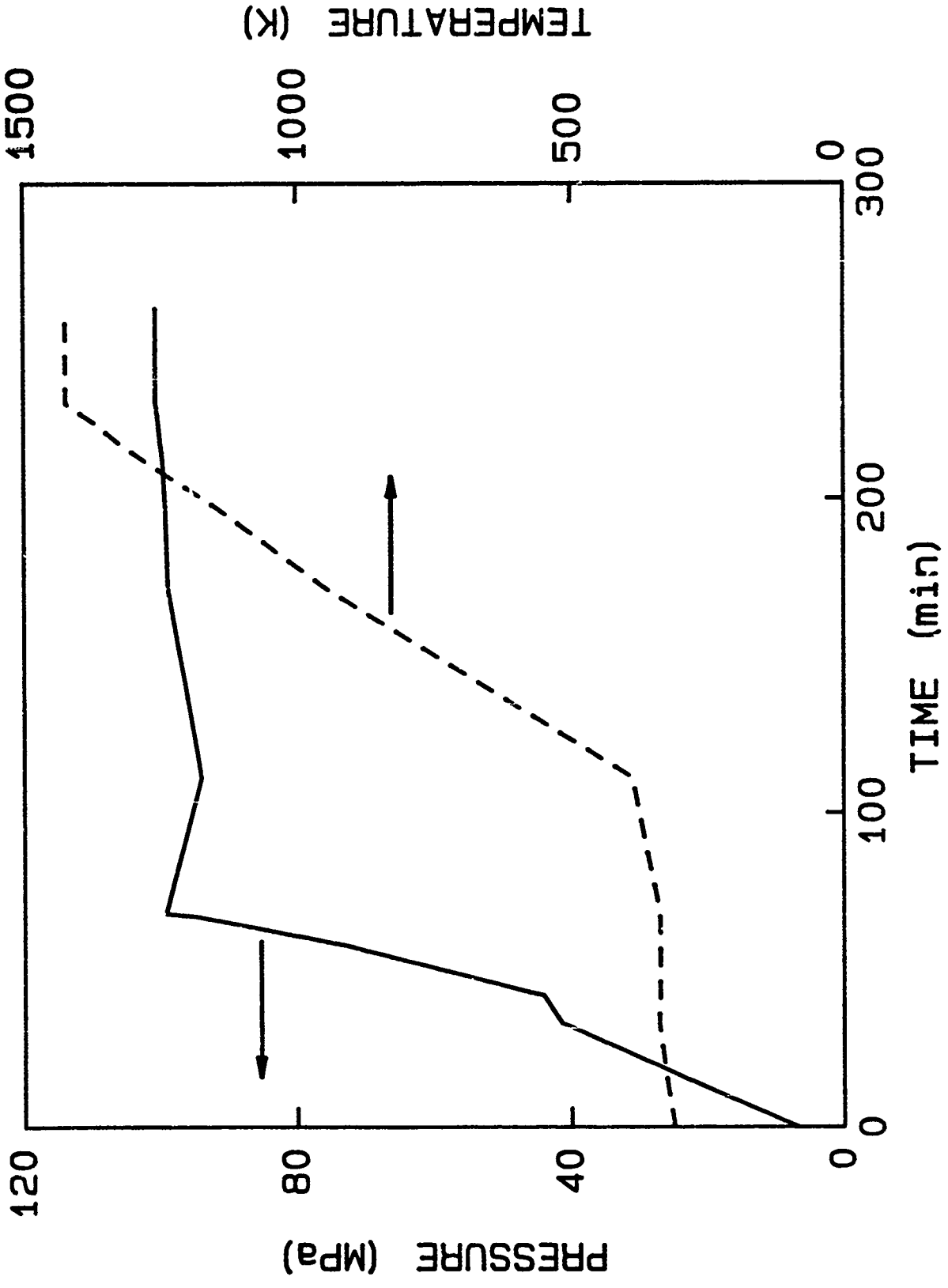


FIGURE 3a.

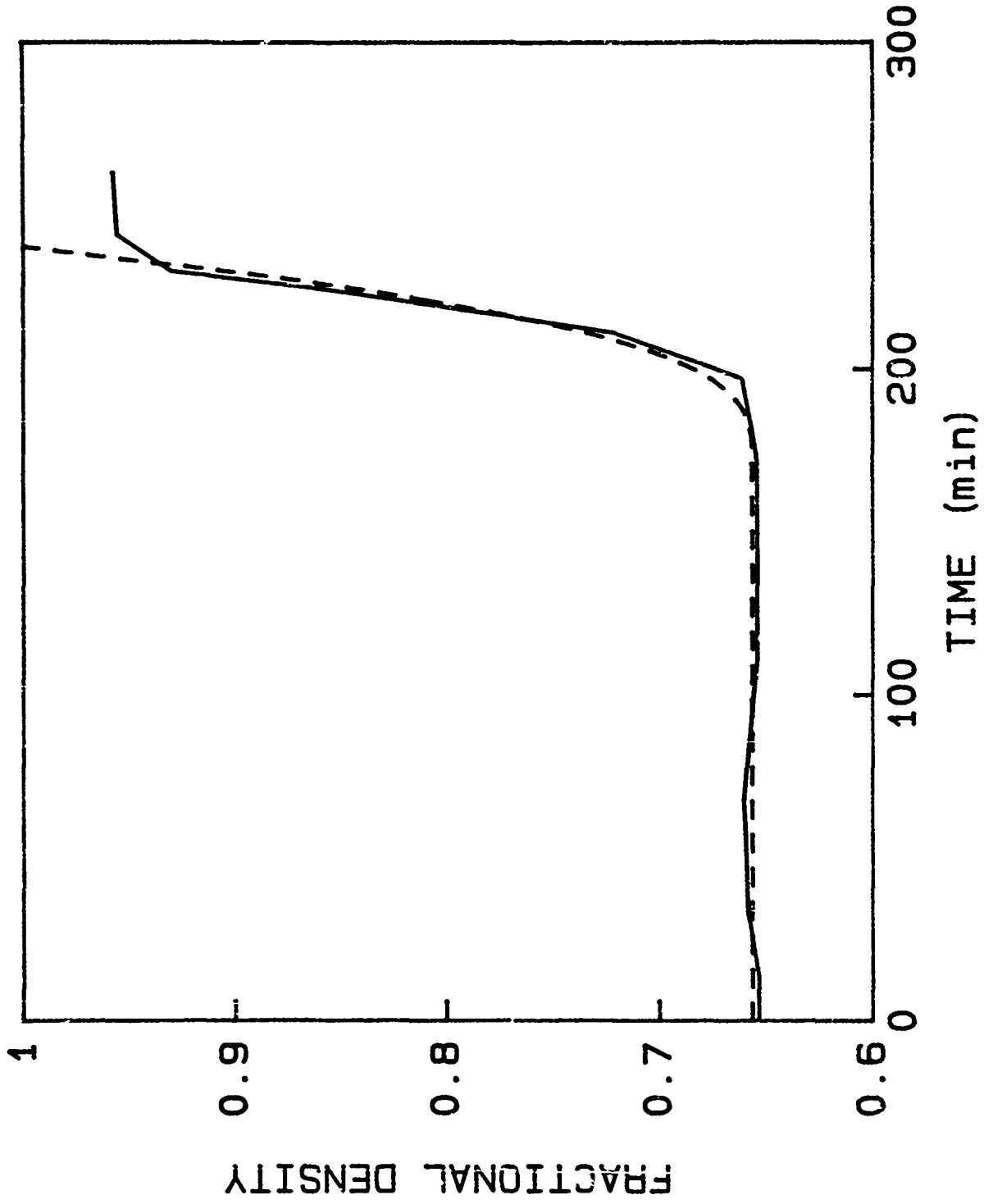


FIGURE 3b.

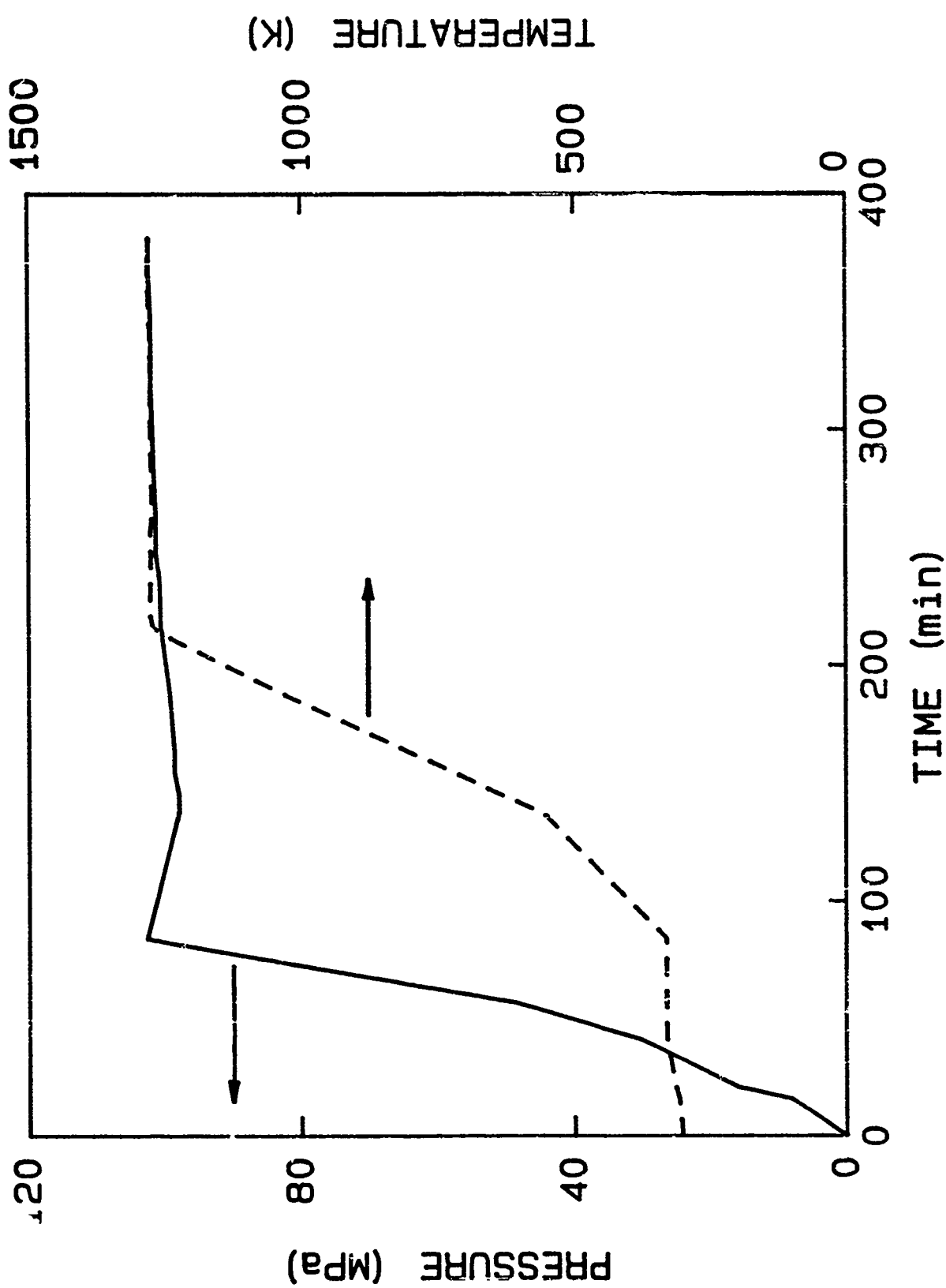


FIGURE 4a.

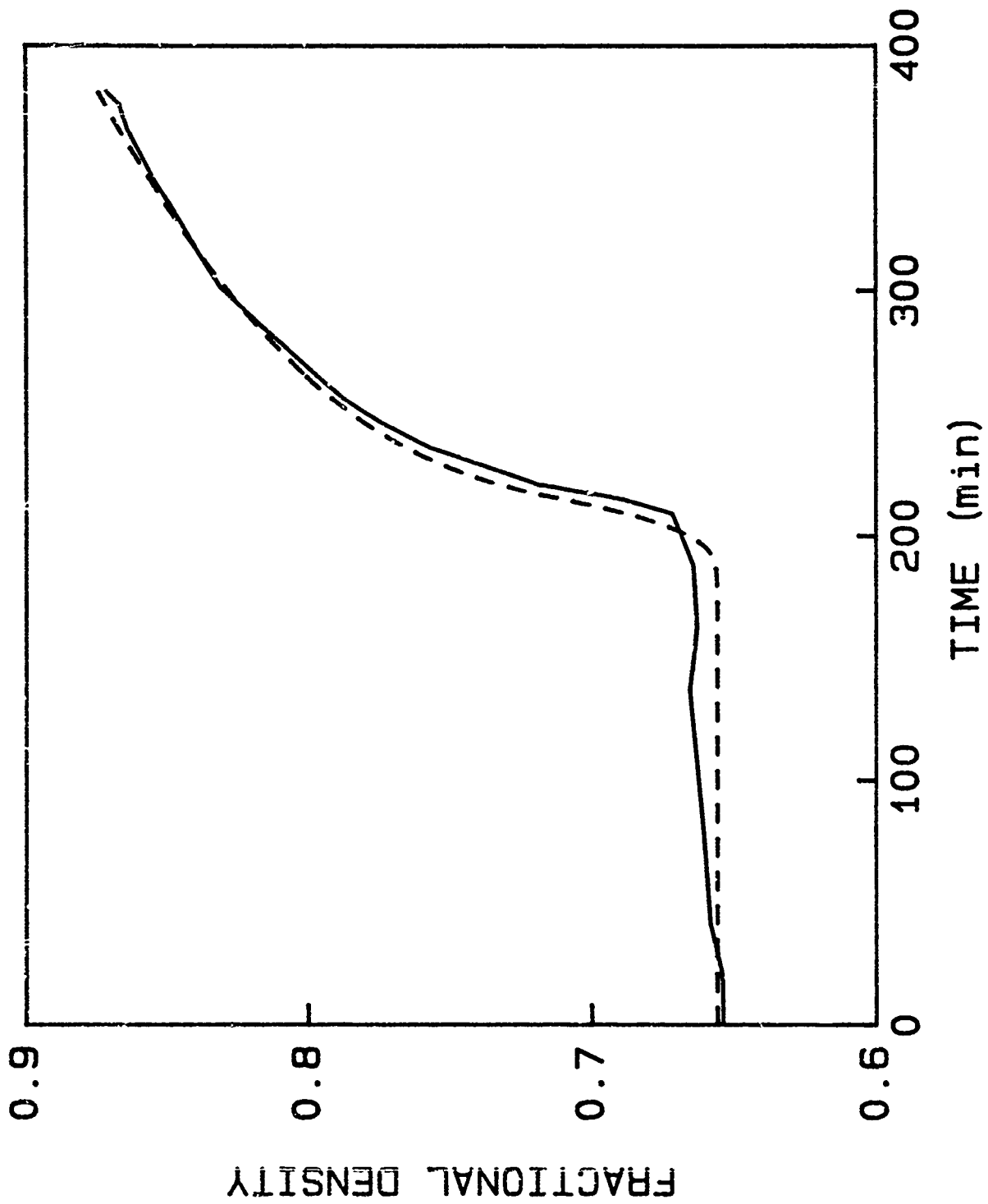


FIGURE 4b.

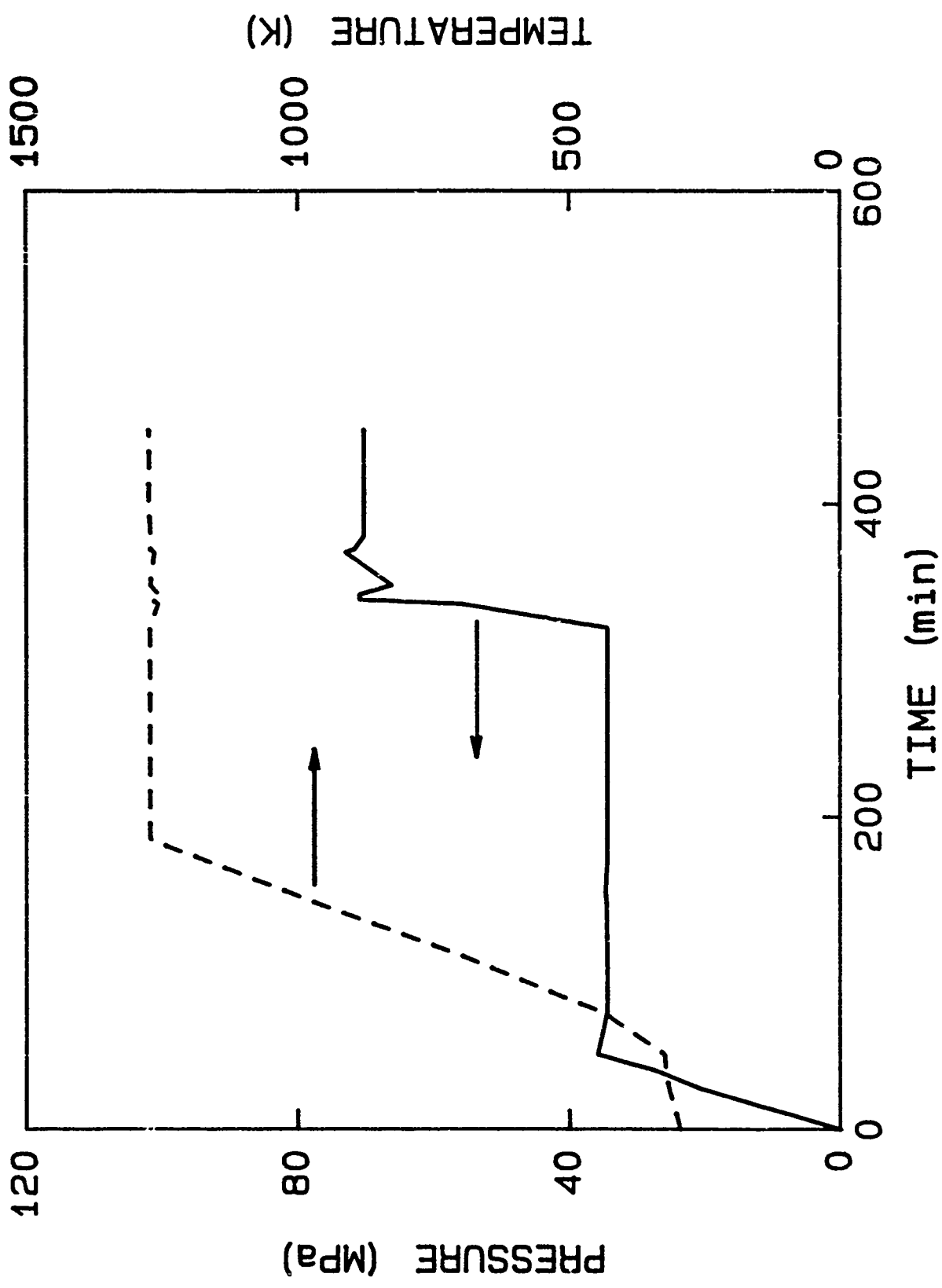


FIGURE 5a.

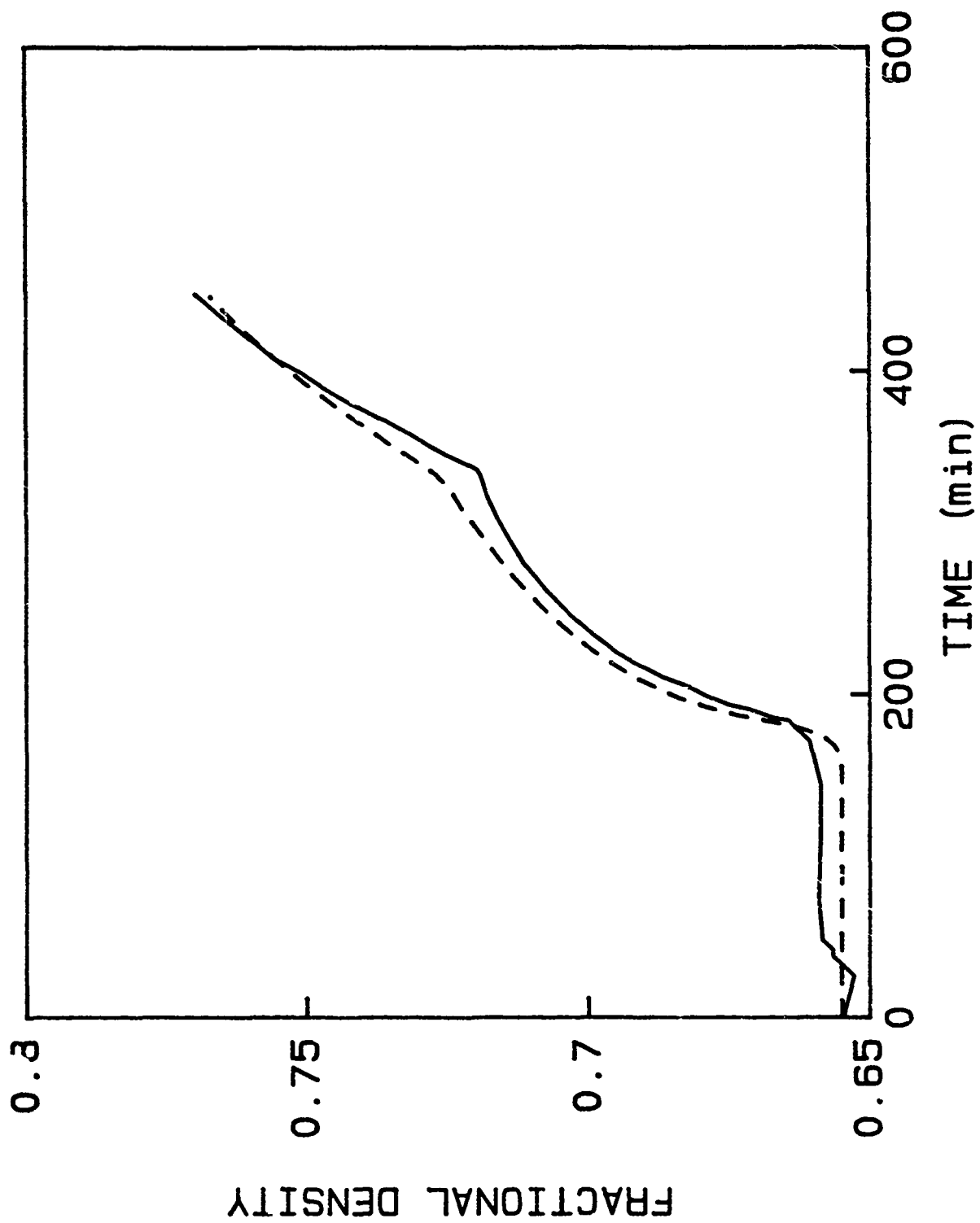


FIGURE 5b.

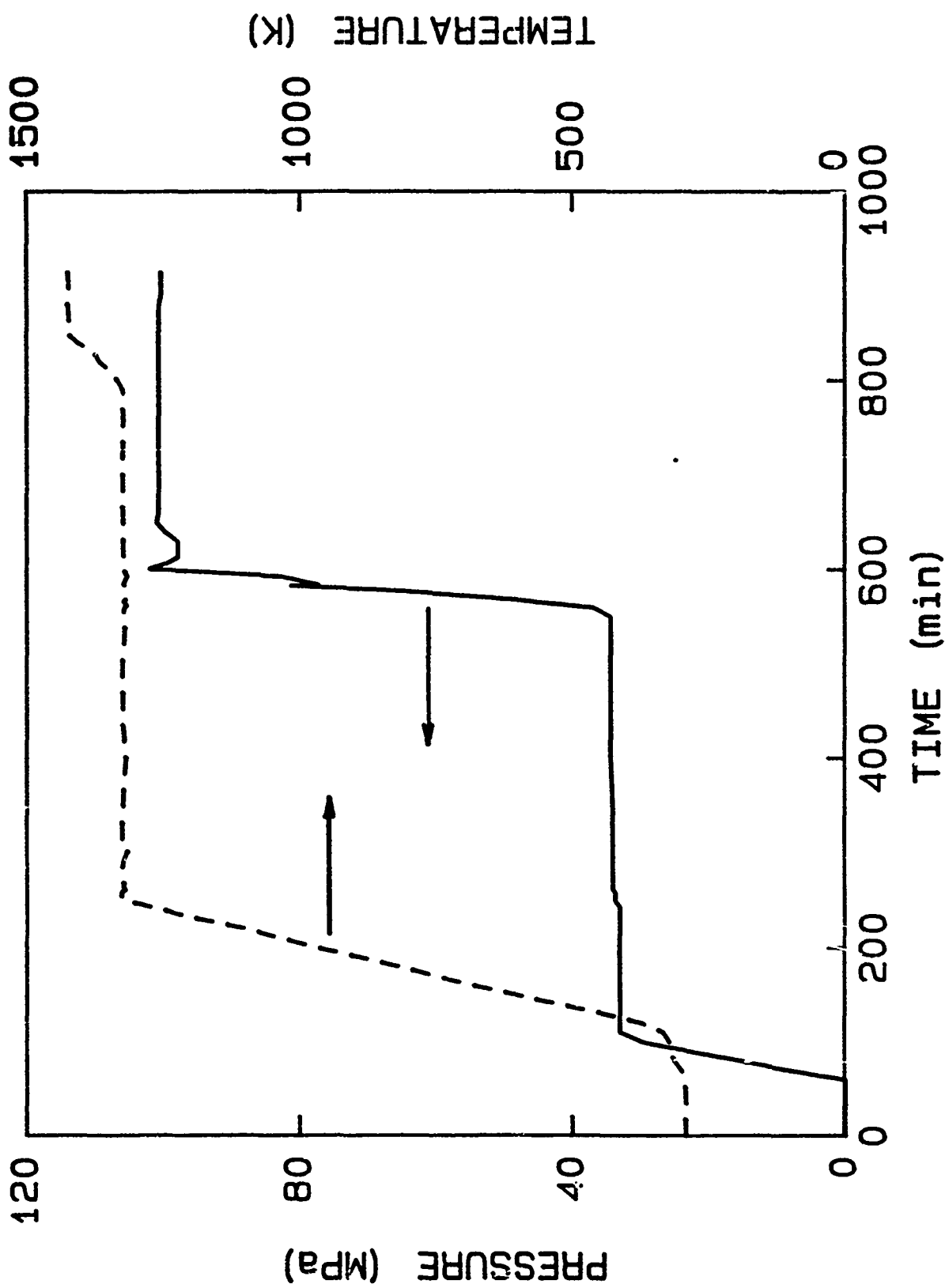


FIGURE 6a.

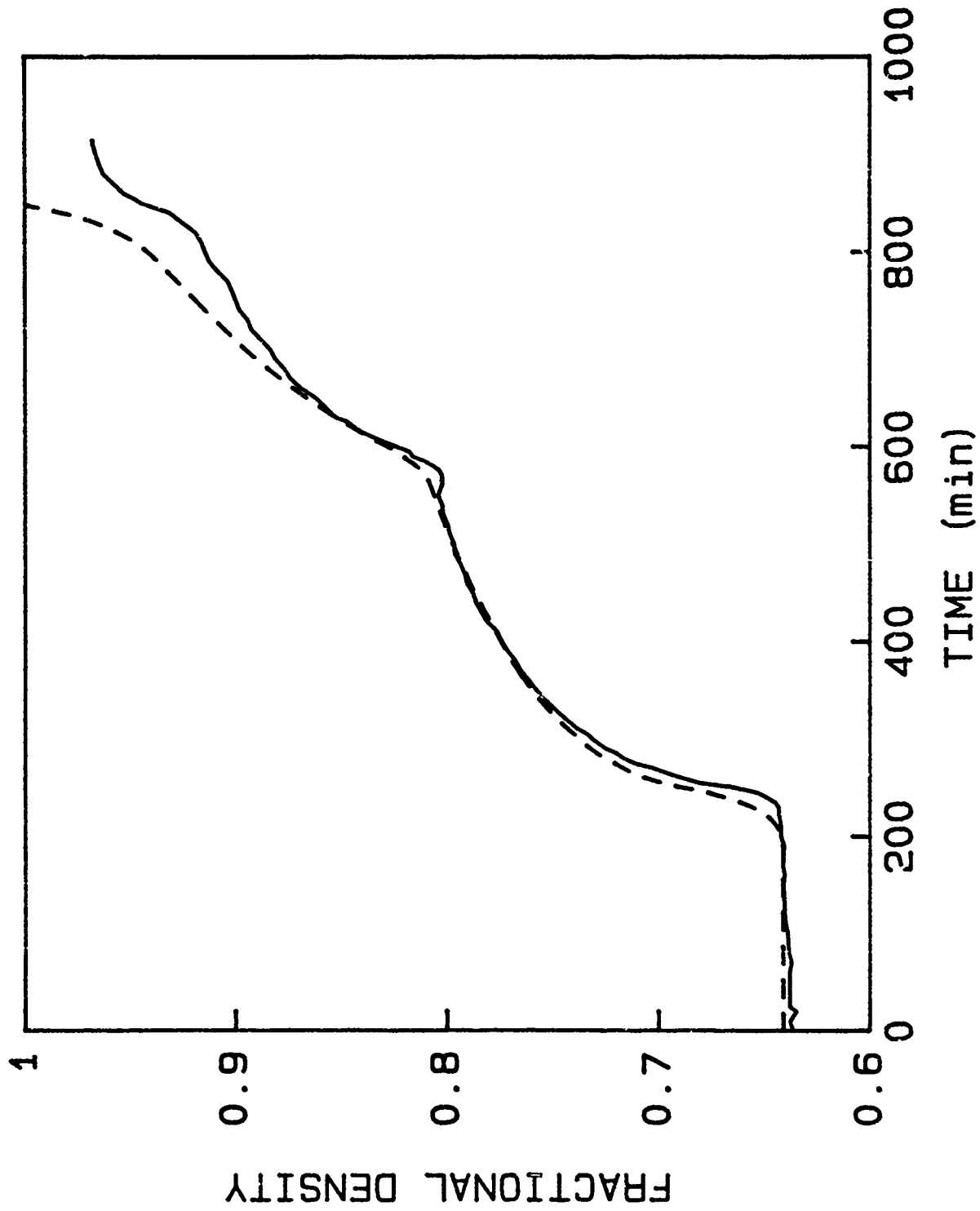


FIGURE 6b.

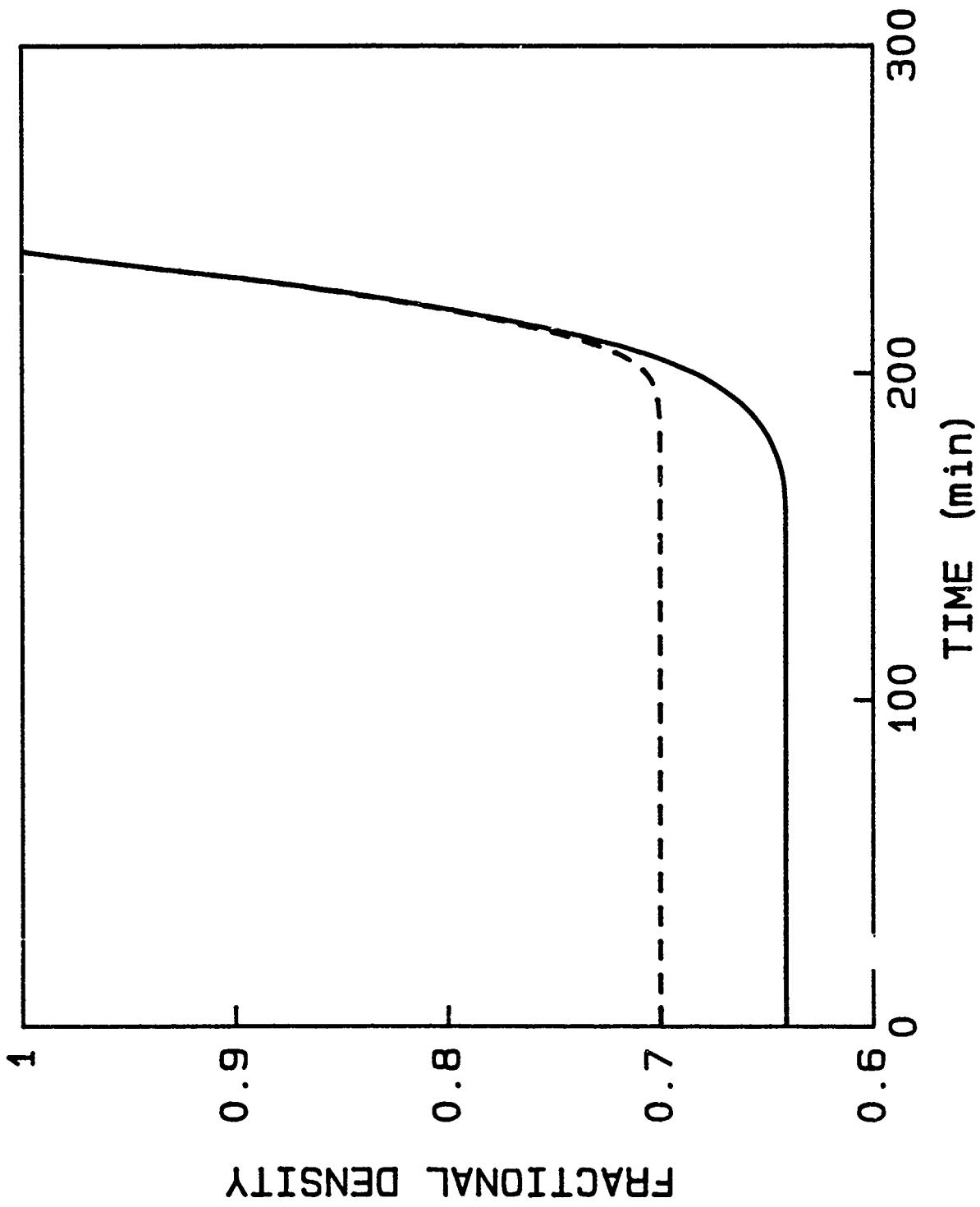


FIGURE 7a.

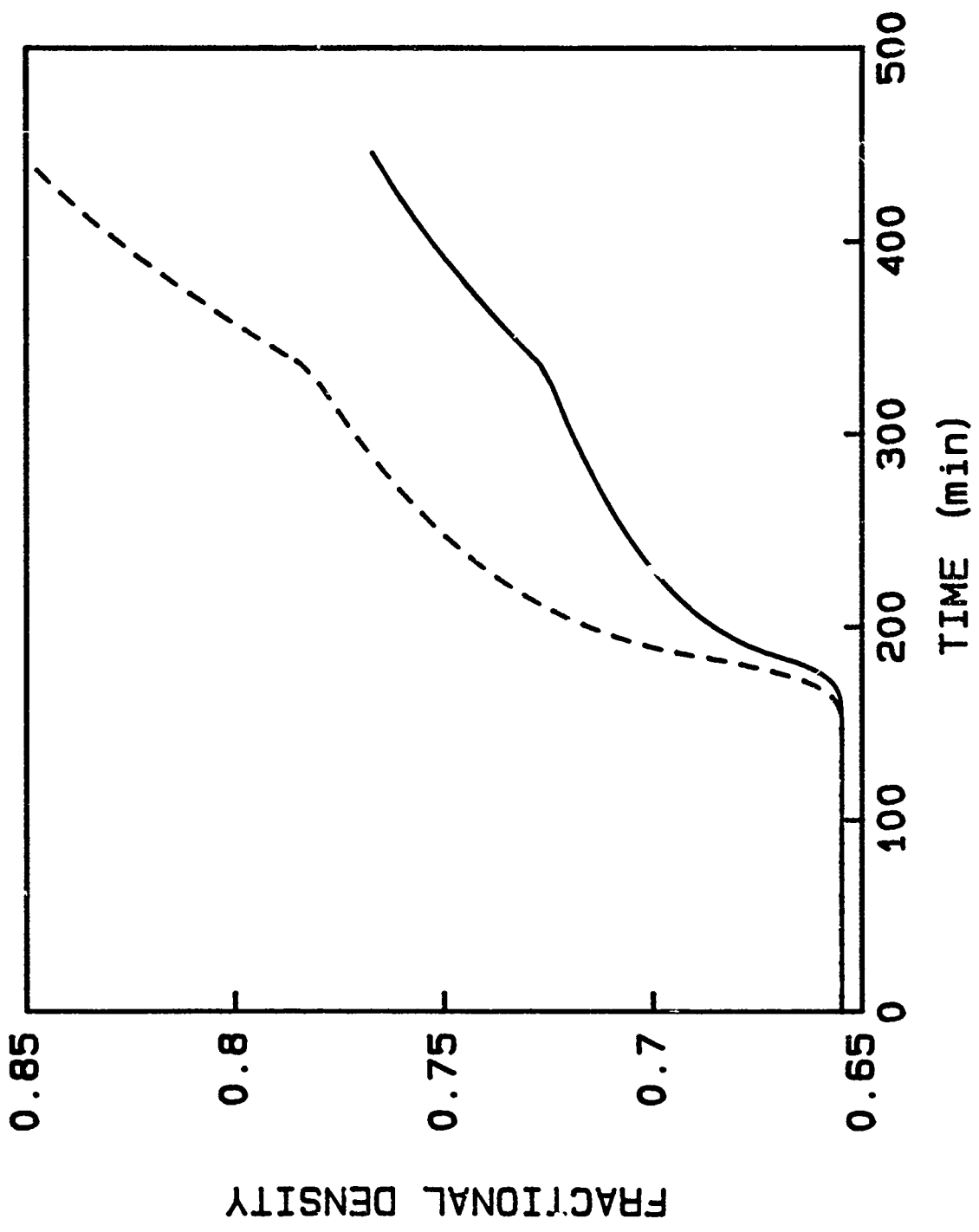


FIGURE 8.

APPENDIX G

COMPUTER SIMULATION OF EFFECTS OF THE PORE SIZE DISTRIBUTION ON THE
KINETICS OF PRESSURE-ASSISTED FINAL-STAGE DENSIFICATION OF A POROUS SOLID

Submitted to

Materials Science and Engineering

COMPUTER SIMULATION OF EFFECTS OF THE PORE SIZE DISTRIBUTION
ON THE KINETICS OF PRESSURE ASSISTED FINAL-STAGE DENSIFICATION

ALAN J. MARKWORTH and J. KEVIN McCOY

Battelle, 505 King Avenue, Columbus, Ohio 43201-2693, USA

Abstract

Most theoretical treatments of pressure-assisted densification of porous solids assume a single size for all pores. We remove this this assumption and consider a distribution of pore sizes. Dissolution of intragranular pores by volume diffusion and dissolution of intergranular pores by grain-boundary diffusion are both treated. The evolution with time of pore size distributions is calculated for distributions that are initially described by log-normal and Weibull functions, and differences in predicted behaviors are discussed. The pore size distribution is then related to two important quantities: porosity and number of pores per unit volume. The assumption of a distribution of pore sizes is found to avoid certain unrealistic predictions obtained from models with a single pore size such as abrupt disappearance of all pores and rapid approach to full density.

1. Introduction

It is frequently observed in studies of densification that full density is difficult to achieve. This is in direct conflict with predictions of rapid and complete densification derived from theoretical models of densification by diffusion. In this paper, we show that the models can be brought into agreement with experience by consideration of the effects of a distribution of pore sizes.

The importance of size-distribution effects in considerations of the evolution of a discrete second-phase species has long been recognized. The porosity within a solid body can be regarded as a particular type of second phase, and its variation with time, resulting from surface-energy and applied-pressure driving forces, can be treated as a type of phase transformation. In this case as well, size-distribution effects can play an important role, for example in considerations of the manner in which the overall volume fraction of porosity varies with time.

Presented below are the results of a modeling study of the dissolution kinetics of a distribution of discrete (i.e., non-overlapping), spherical pores contained within a solid body. Both intragranular and intergranular pores are considered, using well-established expressions for the size-dependent rate of pore dissolution resulting from volume diffusion and grain-boundary diffusion, respectively, of vacancies away from the pore surface. The evolution with time of the pore size distribution is calculated, starting

from various assumed initial distributions, and from this the corresponding variation of the overall porosity of the solid is calculated and related to size-distribution effects.

Because of the fact that both pore-surface-energy and applied-pressure driving forces are considered, the problem is not analytically tractable for either intragranular or intergranular pores. Consequently, solutions are generated numerically.

It is clear that the assumption of a system of discrete pores limits our consideration to a solid for which the amount of porosity is relatively low. This corresponds to what is commonly referred to as the "final stage" of densification. A quantitative evaluation of the probability that a given pore is actually discrete can be carried out, as, for example, has been done [1] for the case of a uniform size distribution of spheres distributed at random within three-dimensional space.

2. Pore-Dissolution Models

Over the years, many investigators have developed models for the growth and dissolution of pores contained within a solid body. (Actually, models for pore growth can be used to describe dissolution as well, if appropriate modification is made of the applied-stress term in the growth-rate expression, as has been discussed by Greenwood [2].) In addition, a variety of kinetic mechanisms has been considered. For purposes of the present analysis,

relatively simple models for pore dissolution are used which nevertheless serve well to illustrate the manner in which size-distribution effects can influence the overall kinetics of porosity reduction.

2.1. Intragranular Pores

For the volume-diffusion-controlled dissolution of an isolated, spherical, intragranular pore (i.e., neighboring pores are assumed not to influence one another), one can derive an expression for the rate of pore dissolution by assuming that the vacancy-concentration field within the solid outside the pore satisfies the Laplace equation. One thus obtains (e.g., [3,4]),

$$\frac{dR}{dt} = -\frac{\Omega D_v}{kTR} \left[P + \frac{2\gamma}{R} \right] \quad (1)$$

where R is the pore radius at time t , Ω , D_v , and γ are the atomic volume, the volume self-diffusivity, and the surface energy of the solid, P is the externally applied pressure, k is Boltzmann's constant, and T is the absolute temperature. Three assumptions inherent in Equation 1 are (a) that the vacancy supersaturation in the lattice is zero, (b) that the "effective" applied pressure inside the solid is unaffected by the presence of the porosity, and (c) that no gases exist inside the pores. Relaxation of assumption (a) has been considered by Geguzin and Lifshitz [3] and others; relaxation of (b) and (c) has been discussed by Markworth [4] and others.

In order to simplify the analysis which follows, we re-express Equation 1 in terms of dimensionless variables, i.e., a pore-size parameter ρ and a time parameter τ defined as

$$\rho \equiv \left[\frac{P}{2\gamma} \right] R \quad (2)$$

$$\tau \equiv \left[\frac{\Omega D_v P^3}{4\gamma^2 kT} \right] \tau \quad (3)$$

in terms of which Equation 1 assumes the much simpler form

$$\frac{d\rho}{d\tau} = -\frac{1}{\rho} \left[1 + \frac{1}{\rho} \right] . \quad (4)$$

2.2. Intergranular Pores

A number of models have been developed with which to describe the grain-boundary-diffusion-controlled and volume-diffusion-controlled growth or dissolution of an intergranular pore. For the present analysis, we consider an isolated spherical pore situated on an planar grain boundary and dissolving by the flow of vacancies away from the pore through the boundary. To describe this situation, we apply a model for grain-boundary-diffusion controlled growth of an intergranular pore developed by Trinkaus [5]. The above-noted modification suggested by Greenwood [2] is used to adapt the model to pore-dissolution kinetics. One thus obtains

$$\frac{dR}{dt} = -\frac{\Omega D_b \delta}{2kTR^2} \left[P + \frac{2\gamma}{R} \right] \quad (5)$$

where D_b is the grain-boundary self-diffusivity, δ is the effective

thickness of the grain boundary, and all other symbols are as defined for Equation 1. Again, it is assumed that the "effective" applied pressure inside the solid is unaffected by the presence of porosity and that no gases exist inside the pores. Effects of gases inside the pores could be considered [5] and are analogous the corresponding effects for intragranular pores.

It is again convenient to express Equation 5 in terms of dimensionless variables. We use the same size and time parameters, ρ and τ , given by Equations 2 and 3, but we define a new dimensionless factor, α , as

$$\alpha = \frac{P\delta}{2\gamma} \frac{D_b}{D_v} \quad (6)$$

and obtain the following simpler form for Equation 5:

$$\frac{d\rho}{d\tau} = -\frac{\alpha}{\rho^2} \left[1 + \frac{1}{\rho} \right] \quad (7)$$

The rate of pore shrinkage $-d\rho/d\tau$ as a function of pore radius ρ is plotted in Fig. 1 for both intergranular and intragranular pores, as calculated from Equations 4 and 7 with a value of $\alpha = 1$. From Fig. 1, it can be seen that the rate of pore shrinkage decreases as pore radius increases, and that the dependence of shrinkage rate on pore size is stronger for intergranular pores than it is for intragranular pores. Note that the shrinkage rate for intergranular pores is dependent on α , and that the corresponding curve in Fig. 1 would be raised or lowered if a different value of α had been chosen.

2.3. Other Pore-Dissolution Models

Clearly, pore-dissolution models other than those represented by Equations 4 and 7 could have been used. These two particular models were chosen because they are particularly amenable to the size-distribution analyses developed below while still containing a description of some essential features of the physics of the respective dissolution processes.

One interesting case not mentioned above is the oft-quoted model of Hull and Rimmer [6] for the stress-induced growth of grain-boundary voids. Using their model, and including only applied-pressure and surface-energy effects as driving forces for pore dissolution, one obtains an expression equivalent to Equation 4 as the dimensionless representation, noting that Equation 4 was derived for a model of intragranular pores. The only difference would be the replacement of D_v in Equation 1 with $D_b\delta/(2a)$ where a is the mean separation between pores. Consequently, the analysis of intragranular porosity based on Equation 1 is mathematically equivalent to that of intergranular porosity based on the Hull-Rimmer model [6]. It should be noted, however, that important corrections to the Hull-Rimmer model have been made, e.g., by Weertman [7].

3. Size-Distribution Kinetics

3.1. Evolution of the Pore Size Distribution

We define the size-distribution function for a system of pores as $f(R, t)$, such that $f(R, t)dR$ is the concentration of pores, at time t , having radius within the range R to $R + dR$. Clearly, it is assumed in this definition that the size distribution exhibits no spatial dependence, on the average. Assuming that no "sources" or "sinks" for pores exist, one can show that the function f satisfies the following continuity relation:

$$\frac{\partial f}{\partial t} + \frac{\partial}{\partial R}(vf) = 0 \quad (8)$$

where v is a function that describes the rate at which a given pore, which can be considered as a point existing in a one-dimensional pore-radius space, moves through that space. (Obviously, the definition of v is equivalent to dR/dt which is given in Equations 1 and 5 for the two models under consideration here.) Expressing Equation 8 in terms of the dimensionless parameters ρ and τ ,

$$\frac{\partial f}{\partial \tau} + \frac{\partial}{\partial \rho}(vf) = 0 \quad (9)$$

where now $f(\rho, \tau)d\rho$ is the concentration of pores, at time τ having radius within the range ρ to $\rho + d\rho$, and v is now equivalent to the "velocity", $d\rho/d\tau$, in ρ -space.

The "flux" of pores crossing a given point of the one-dimensional ρ -space is, in general, equal to $v(\rho, \tau)f(\rho, \tau)$. For

the pore-dissolution models under consideration here, v has explicit dependence only upon ρ (see Equations 4 and 7).

Let us examine the behavior of the pore flux with respect to a moving coordinate frame in our one-dimensional ρ -space. Specifically, let ρ' be a coordinate which moves along the ρ -axis at the same rate as a pore having instantaneous size ρ . Hence, ρ' is given through the relation

$$\tau - \tau_0 = \int_{\rho_0}^{\rho'} \frac{d\rho}{v(\rho)} \quad (10)$$

where ρ_0 is the size of the pore at some given initial time τ_0 and where we again take v to depend only upon ρ . From Equation 10 we obtain

$$\frac{d\rho'}{d\tau} = v(\rho') \quad (11)$$

It now follows that,

$$\begin{aligned} \frac{d}{d\tau} [v(\rho')f(\rho', \tau)] & \quad (12) \\ &= \left[\frac{dv(\rho')}{d\rho'} \frac{d\rho'}{d\tau} \right] f(\rho', \tau) \\ &+ v(\rho') \left[\frac{\partial}{\partial \rho'} f(\rho', \tau) \frac{d\rho'}{d\tau} + \frac{\partial}{\partial \tau} f(\rho', \tau) \right] . \end{aligned}$$

Combining Equations 11 and 12,

$$\begin{aligned} \frac{d}{d\tau} [v(\rho')f(\rho', \tau)] & \quad (13) \\ &= v(\rho') \left[\frac{dv(\rho')}{d\rho'} f(\rho', \tau) + \frac{\partial}{\partial \rho'} f(\rho', \tau) + \frac{\partial}{\partial \tau} f(\rho', \tau) \right] . \end{aligned}$$

Now, the continuity equation, Equation 9, must also be satisfied

with respect to the moving coordinate system, in which case the sum of the terms within brackets on the right hand side of Equation 13 is zero. Consequently,

$$\frac{d}{d\tau} [v(\rho')f(\rho', \tau)] = 0 . \quad (14)$$

An alternative way of expressing Equation 14 is the following:

$$v(\rho)f(\rho, \tau) = v(\rho)f(\rho_0, \tau) \quad (15)$$

where ρ (dropping the prime symbol) is understood to be the size of a pore, at time τ that had size ρ_0 at an earlier time τ_0 . Taking $\tau_0 = 0$ and $g(\rho_0) \equiv f(\rho_0, 0)$, we obtain

$$f(\rho, \tau) = \left[\frac{v(\rho_0)}{v(\rho)} \right] g(\rho_0) . \quad (16)$$

Equation 16 can be used to relate the size distribution at time $\tau = 0$ to that at some late time $\tau > 0$. An alternative derivation of Equation 15 is presented in the appendix.

In order to apply Equation 16 to cases of interest here, one can use Equation 10 (again, and from now on, dropping the prime symbol) together with the given expressions for $v(\rho)$. This can be done in closed form for the models under consideration here. In particular, substituting the right-hand side of Equation 4 for $v(\rho)$ into Equation 10 and integrating, one obtains the following expression for intragranular pores:

$$\tau = \frac{1}{2}(\rho_0 - \rho)(\rho_0 + \rho - 2) + \ln \left[\frac{1 + \rho_0}{1 + \rho} \right] . \quad (17)$$

Likewise, substituting the right-hand side of Equation 7 for $v(\rho)$ into Equation 10 and integrating, one obtains the following expression for intergranular pores:

$$\alpha\tau = \frac{1}{3}(\rho_0^3 - \rho^3) + (\rho_0 - \rho) - (\rho_0^2 - \rho^2) + \ln \left[\frac{1 + \rho}{1 + \rho_0} \right] . \quad (18)$$

Unfortunately, for given values of τ and ρ_0 , the value of ρ can be calculated from either Equation 17 or 18 only through some numerical procedure. Given this fact, however, the problem of calculating the evolution of the pore size distribution is, in principle, solved.

The above analysis can be cast in somewhat simpler form by taking

$$\rho_0 = \rho + \Delta \quad (19)$$

where $\Delta > 0$ since the pores are dissolving. In this form, Equations 16, 17 and 18, respectively, become

$$f(\rho, \tau) = \frac{v(\rho + \Delta)}{v(\rho)} g(\rho + \Delta) \quad (20)$$

$$\tau = \Delta(\rho - 1 + \frac{1}{2}\Delta) + \ln \left[\frac{1 + \rho + \Delta}{1 + \rho} \right] \quad (21)$$

$$\alpha\tau = \Delta(\rho^2 + \rho\Delta + \frac{1}{3}\Delta^2 + 1 - \rho - \frac{1}{2}\Delta) - \ln \left[\frac{1 + \rho + \Delta}{1 + \rho} \right] . \quad (22)$$

For given ρ and τ , Equations 21 and 22 can be solved numerically for the corresponding values of Δ for intragranular and intergranular pores, respectively.

3.2. Evolution of Distribution-Function Moments

Properties of physical interest are related to moments of the size-distribution function, rather than to the distribution function per se, defining the i -th algebraic moment (i.e., the i -th moment about $\rho = 0$) as

$$M_i(\tau) = \int_0^{\infty} \rho^i f(\rho, \tau) d\rho . \quad (23)$$

For example, $M_0(\tau)$ is the net concentration of pores within the solid, and the volume fraction occupied by porosity is linearly proportional to $M_3(\tau)$.

There are different ways in which $M_i(\tau)$ can be calculated (see, e.g., [8, 9]). As discussed below, the approach used here is to calculate $f(\rho, \tau)$ using a general approach described above, and then numerically integrating, using Equation 23 as a basis, to determine the moments of interest.

One case is of particular interest, namely, that involving M_0 . It can easily be shown that an alternative expression for M_0 is

$$M_0(\tau) = \int_{\Delta_0}^{\infty} g(\rho) d\rho \quad (24)$$

where the quantity Δ_0 in Equation 24 is the value of Δ , obtained from Equation 21 or 22, corresponding to $\rho = 0$. Thus, for intragranular and intergranular pores, respectively,

$$\tau = \Delta_0 \left(\frac{1}{2} \Delta_0 - 1 \right) + \ln(1 + \Delta_0) \quad (25)$$

$$\alpha\tau = \Delta_0 \left(\frac{1}{3} \frac{\Delta_0^2}{c} - \frac{1}{2} \Delta_0 - 1 \right) - \ln(1 + \Delta_0) . \quad (26)$$

The values of M_0 can be calculated, for a given value of τ , simply by numerically determining the pertinent value of Δ_0 from Equation 25 or 26, and then performing the integration indicated in Equation 24. The result obtained by this approach should yield the same result as that obtained from the approach previously described based on the use of Equation 23. In fact, comparison of the values of M_0 calculated using the two different approaches would serve as a useful check of the accuracy of the numerical procedures and was indeed used for this purpose in the examples described below.

4. Application to Specific Examples

The methods of calculating size-distribution kinetics described above may be applied to a wide variety of initial pore-size distributions. We have applied them to a Weibull distribution

$$g(\rho) = m\rho^{m-1}e^{-\rho^m} . \quad (25)$$

with $m = 2, 2.5,$ and $3,$ and to a log-normal distribution

$$g(\rho) = \frac{1}{\sqrt{2\pi}c\rho} \exp \left[\frac{-[\ln(\rho/b)]^2}{(2c^2)} \right] , \quad (26)$$

where we have taken $b = 0.8$ and $c = 0.5$. As will be seen from the figures below, these distributions are generally similar in appearance. The most important difference among them is that the log-normal distribution has a long large-radius tail, while the large-

radius tails of the Weibull distributions are smaller and decrease with increasing m .

All of these functions are normalized, that is, they have $M_0 = 1$. However, due to the differences between the functions, it is generally not possible to normalize the third moments simultaneously. For the Weibull distributions, we have $M_3 = \Gamma(1 + 3/m)$ while for the log-normal distribution, $M_3 = b^3 \exp(9c^2/2)$.

In Figs. 2-4 we present plots of the pore size distribution function for selected times and various initial distributions as calculated using Equation 4 for the kinetics of dissolution of intragranular pores. Results for the Weibull distribution with $m = 2.5$ are not plotted but were intermediate between the results for $m = 2$ and $m = 3$. From Fig. 2, it will be noted that the position of the peak of the distribution function moves toward larger radii as time progresses. A similar but smaller effect can be seen in Fig. 3, while in Fig. 4, position of the peak clearly shifts toward smaller radii. This behavior is in marked contrast to that of standard models in which all pores are the same size and all pores shrink together: for densification to occur, the pore radius must shrink. If there is a distribution of pore sizes, however, the peak of the distribution may move in either direction, depending on the shape of the distribution and the velocity function. The influence of the velocity function may be seen in Figs. 5-7, which differ from Figs. 2-4 only in that the velocity for intergranular pores was

used. For all calculations with intergranular pores, we took $\alpha = 1$. As seen in Figs. 5-7, the peak shifts strongly to higher radii for the log-normal distribution, somewhat less strongly for the Weibull distribution with $m = 2$, and only slightly for the Weibull distribution with $m = 3$. It is clear from the figures that, qualitatively, if the magnitude of the velocity function decreases strongly with increasing radius and the initial distribution has a long large-radius tail, the peak of the distribution function will shift toward the right, since the small pores disappear quickly, leaving the larger pores almost unchanged. Conversely, if the velocity function depends weakly on radius and the initial distribution is narrow, the pores will shrink together and the peak of the distribution will move to the left.

While the pore size distribution functions would be difficult to determine experimentally, two quantities that are more easily measured are the number of pores per unit volume and the porosity. These two quantities are proportional to M_0 and M_3 , respectively. The moments are plotted as functions of time for all four distributions and both velocity functions in Figs. 8-11. For comparison, we have also plotted the third moments for a distribution in which all pores are the same size. An initial pore radius of $r = (3/4\pi)^{1/3}$ was used.

If it is assumed that all pores have the same size, all pores vanish simultaneously, and M_0 changes discontinuously. A more

realistic picture is seen in Figs. 8 and 10: the number of pores gradually decreases toward zero. At times up to $\tau = 0.2$, the number of pores decreases at comparable rates for all four distributions, reflecting the general similarity of the central portion of the distributions. By $\tau = 1$, however, the distributions are dominated by what was originally the large-radius tail of the distribution, and, for both velocity functions, the log-normal distribution has the largest number of pores, followed by the Weibull distributions in order of increasing m .

From Figs. 9 and 11, we note again the unrealistic results obtained by assuming a single pore size: densification proceeds rapidly to completion. At short times, the rates of change of the third moment as obtained by assuming a distribution of pore sizes agree relatively well with those for a single pore size and with each other. However, the results soon begin to diverge. For a single size of intragranular pores, it is predicted that all porosity will vanish at $\tau = 0.247$, but all of the calculations with a distribution of sizes give significant remaining porosity at this time. The contrast is even stronger in the case of intergranular pores. The calculation with a single pore size shows all porosity vanishing at $\tau = 0.196$, but, for the log-normal distribution and Weibull distribution with $m = 2$, more than half of the original porosity remains. For both velocity functions, the calculations on a log-normal distribution give significant remaining porosity at $\tau = 1$.

5. Discussion

Size-distribution effects associated with pores in solids have been studied by other investigators as well. For example, Tomandl [10] considered pore shrinkage resulting from sintering without any externally applied pressure. The expression he used to describe the rate of pore dissolution by diffusion along grain boundaries was

$$\frac{dR}{dt} = -\frac{c_p}{R^2} \quad (27)$$

where c_p is a parameter that is dependent upon temperature. Clearly, Equation 27 is mathematically equivalent to Equation 1 if P is set equal to zero in the latter. They then differ only in the form of the coefficient of the R^{-2} term. For this limiting case, the time-dependent size-distribution function can be derived in closed form, as Tomandl has shown [10]. In other studies [11, 12], the evolution of a cavity size distribution under an applied tensile stress was studied. The rate of change of pore size was here described by an expression equivalent to our Equation 5, with P replaced with $-\sigma$, where σ is the tensile stress at and perpendicular to the grain boundary. It was assumed that σ is equal to the externally applied tensile stress, an assumption which (as was pointed out [12]) is not generally valid. The evolution of the cavity size distribution was evaluated numerically using an approach that was analogous to that used here.

It is a common experience in sintering and hot isostatic pressing to observe that it is difficult to achieve full density. This is in marked contrast to the predictions of rapid and complete densification obtained from standard models derived under the assumptions of diffusional control and a single pore size. We have shown that more realistic results may be obtained by assuming that a distribution of pore sizes exists in the material. We have also shown that the most likely pore size can increase even as densification proceeds and all pores shrink.

It is beyond the scope of this paper to relate pore size distributions to particle size distributions and particle packings. However, it is clear from this work that behavior in the limit of long time (and high density) is controlled by large pores. It is expected that these large pores would be found near large initial particles or fully densified agglomerates.

Acknowledgement

Support of this work by the Air Force Office of Scientific Research under Grant No. 82-0238 is gratefully acknowledged.

Appendix: Alternative Derivation of Equation 15

In this appendix, we present an alternative derivation of Equation 15, one that is perhaps simpler than that developed in the text, but which nevertheless is mathematically rigorous.

Consider a pore that has size ρ_0 as time τ_0 and size $\rho \geq 0$ at some later time τ . The relationship between ρ and τ is given by Equation 10 (dropping the prime symbol in Equation 10). Likewise, consider another pore that has size $\rho_0 + d\rho_0$ at time τ_0 and size $\rho + d\rho$ at time τ . For this case, Equation 10 becomes

$$\tau - \tau_0 = \frac{\rho + d\rho}{\rho_0 + d\rho_0} \int \frac{d\rho}{v(\rho)}. \quad (\text{A.1})$$

Subtracting Equation 10 from A.1,

$$0 = \frac{\rho + d\rho}{\rho_0 + d\rho_0} \int \frac{d\rho}{v(\rho)} - \int \frac{\rho}{\rho_0} \frac{d\rho}{v(\rho)}. \quad (\text{A.2})$$

or

$$\frac{\rho + d\rho}{\rho_0 + d\rho_0} \int \frac{d\rho}{v(\rho)} = \int \frac{\rho}{\rho_0} \frac{d\rho}{v(\rho)}. \quad (\text{A.3})$$

For infinitesimally small $d\rho_0$ and $d\rho$, Equation A.3 can be expressed as

$$\frac{d\rho}{v(\rho)} = \frac{d\rho_0}{v(\rho_0)}. \quad (\text{A.4})$$

The concentration of pores at time τ_0 within the interval ρ_0 to $\rho_0 + d\rho_0$ is $f(\rho_0, \tau_0)d\rho_0$ and that at time τ within the interval ρ to $\rho + d\rho$ is $f(\rho, \tau)d\rho$. Clearly, these must be equal, i.e.,

$$f(\rho, \tau)d\rho = f(\rho_0, \tau_0)d\rho_0. \quad (\text{A.5})$$

Eliminating $d\rho$ and $d\rho_0$ from Equation A.5 by application of Equation A.4, we find that

$$v(\rho)f(\rho, \tau) = v(\rho_0)f(\rho_0, \tau_0) \quad (\text{A.6})$$

and we see that Equations A.6 and 15 are identical.

References

1. A. J. MARKWORTH, *Scr. Metall.* 18 (1984) 1309.
2. G. W. GREENWOOD, in "Vacancies '76", edited by R. E. Smallman and J. E. Harris (The Metals Soc., London, 1977) p. 141.
3. Ya. E. GEGUZIN and I. M. LIFSHITZ, *Soviet Phys.--Solid State* 4 (1962) 971.
4. A. J. MARKWORTH, *Scr. Metall.* 6 (1972) 957.
5. H. TRINKAUS, *Scr. Metall.* 15 (1981) 825.
6. D. HULL and D. E. RIMMER, *Philos. Mag.* 4 (1959) 673.
7. J. WEERTMAN, *Scr. Metall.* 7 (1973) 1129.
8. A. D. RANDOLPH and M. A. LARSON, "Theory of Particulate Processes--Analysis and Techniques of Continuous Crystallization" (Academic Press, Inc., New York, 1971) pp. 53 ff.
9. A. J. MARKWORTH, in "Defects and Transport in Oxides", edited by M. S. Seltzer and R. I. Jaffee (Plenum Press, New York, 1974) p. 397.

10. G. TOMANDL, in "Science of Ceramics", vol. 9, edited by K. J. deVries (The Netherlands Ceramic Soc., 1977), p. 158.
11. G. SOULLARD, L. MARTINEZ, and J. OSEGUERA, *Scr. Metall.* 19 (1985) 581.
12. L. MARTINEZ and J. H. SCHNEIBEL, *Philos. Mag. A*, 51 (1985) L29.

List of Figures

Fig. 1. Normalized shrinkage rate as a function of normalized pore radius for two types of pores. Solid line: intragranular pores. Dashed line: intergranular pores.

Fig. 2. Pore size distribution function for intragranular pores at several times. Initial distribution is log-normal.

Fig. 3. Pore size distribution function for intragranular pores at several times. Initial distribution is Weibull with $m = 2$.

Fig. 4. Pore size distribution function for intragranular pores at several times. Initial distribution is Weibull with $m = 3$.

Fig. 5. Pore size distribution function for intergranular pores at several times. Initial distribution is log-normal.

Fig. 6. Pore size distribution function for intergranular pores at several times. Initial distribution is Weibull with $m = 2$.

Fig. 7. Pore size distribution function for intergranular pores at several times. Initial distribution is Weibull with $m = 3$.

Fig. 8. Zeroth moment of the pore distribution function (proportional to number of pores) as a function of time for intragranular pores with four initial pore size distributions. Solid line: log-normal. Short-dashed line: Weibull, $m = 2$. Dot-dashed line:

Weibull, $m = 2.5$. Long-dashed line: Weibull, $m = 3$.

Fig. 9. Third moment of the pore distribution function (proportional to porosity) as a function of time for intragranular pores with five initial pore size distributions. Solid line: log-normal. Short-dashed line: Weibull, $m = 2$. Dot-dashed line: Weibull, $m = 2.5$. Long-dashed line: Weibull, $m = 3$. Dotted line: single pore size.

Fig. 10. Zeroth moment of the pore distribution function (proportional to number of pores) as a function of time for intragranular pores with four initial pore size distributions. Solid line: log-normal. Short-dashed line: Weibull, $m = 2$. Dot-dashed line: Weibull, $m = 2.5$. Long-dashed line: Weibull, $m = 3$.

Fig. 11. Third moment of the pore distribution function (proportional to porosity) as a function of time for intragranular pores with five initial pore size distributions. Solid line: log-normal. Short-dashed line: Weibull, $m = 2$. Dot-dashed line: Weibull, $m = 2.5$. Long-dashed line: Weibull, $m = 3$. Dotted line: single pore size.

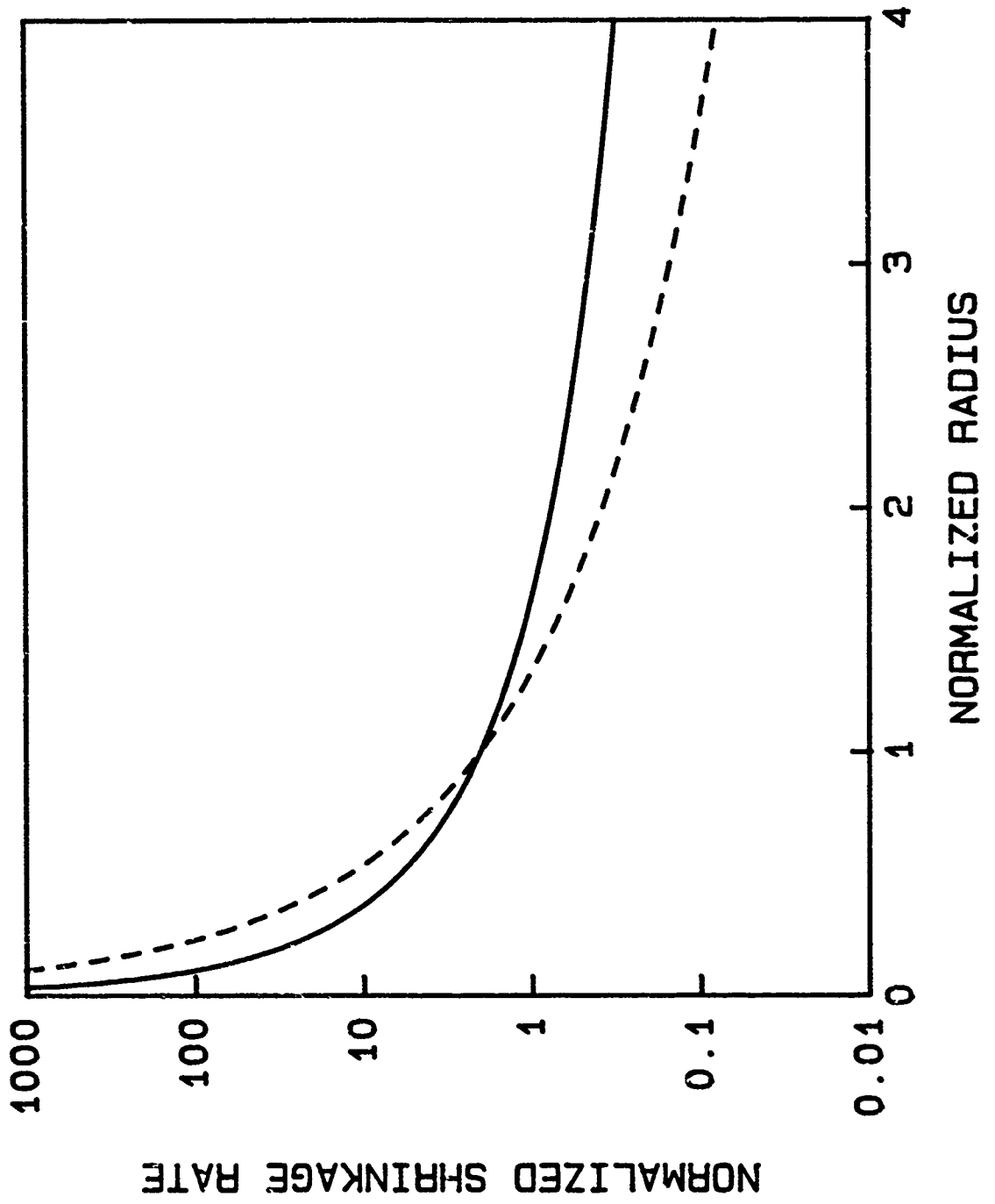
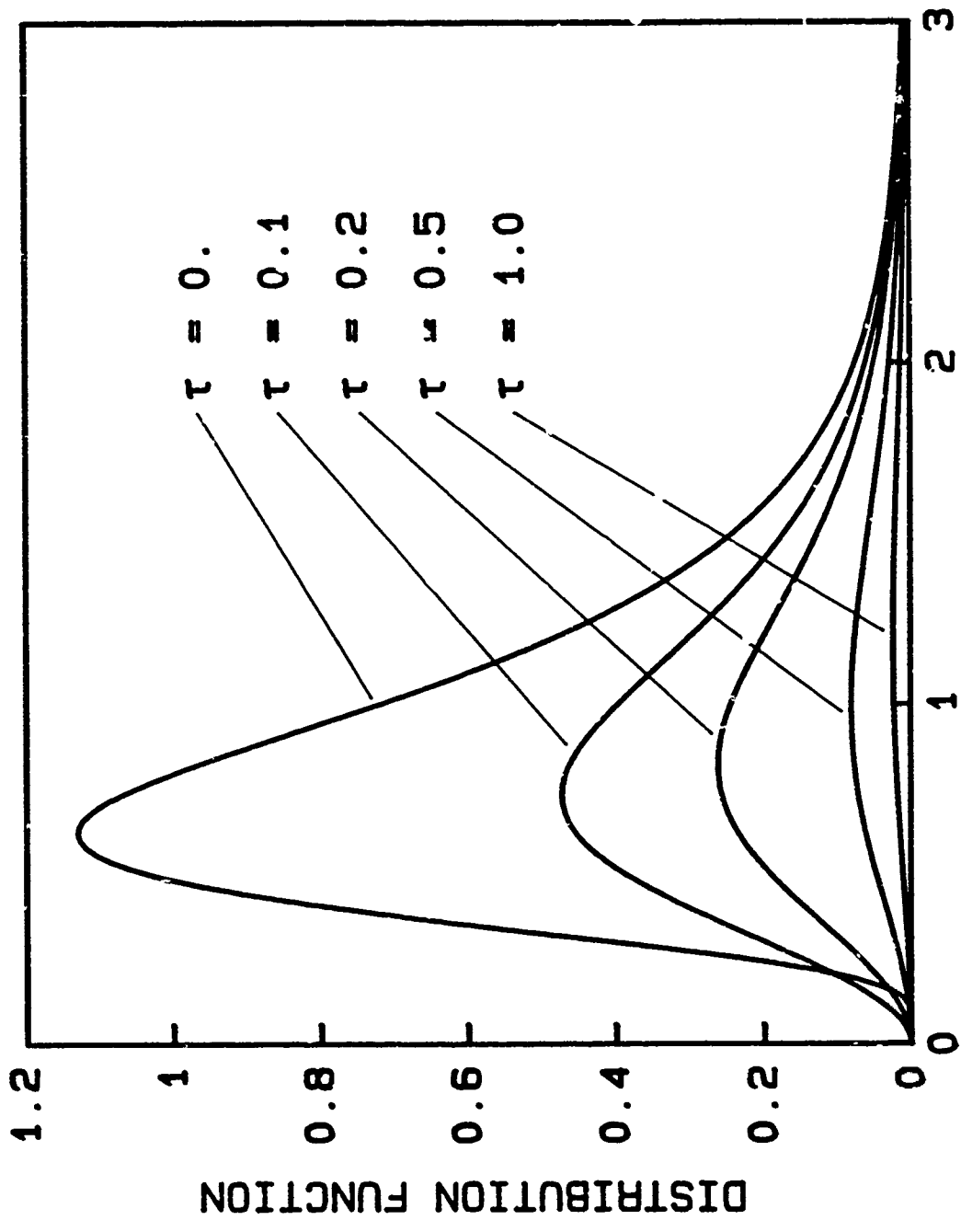


FIGURE 1.



NORMALIZED RADIUS

FIGURE 2

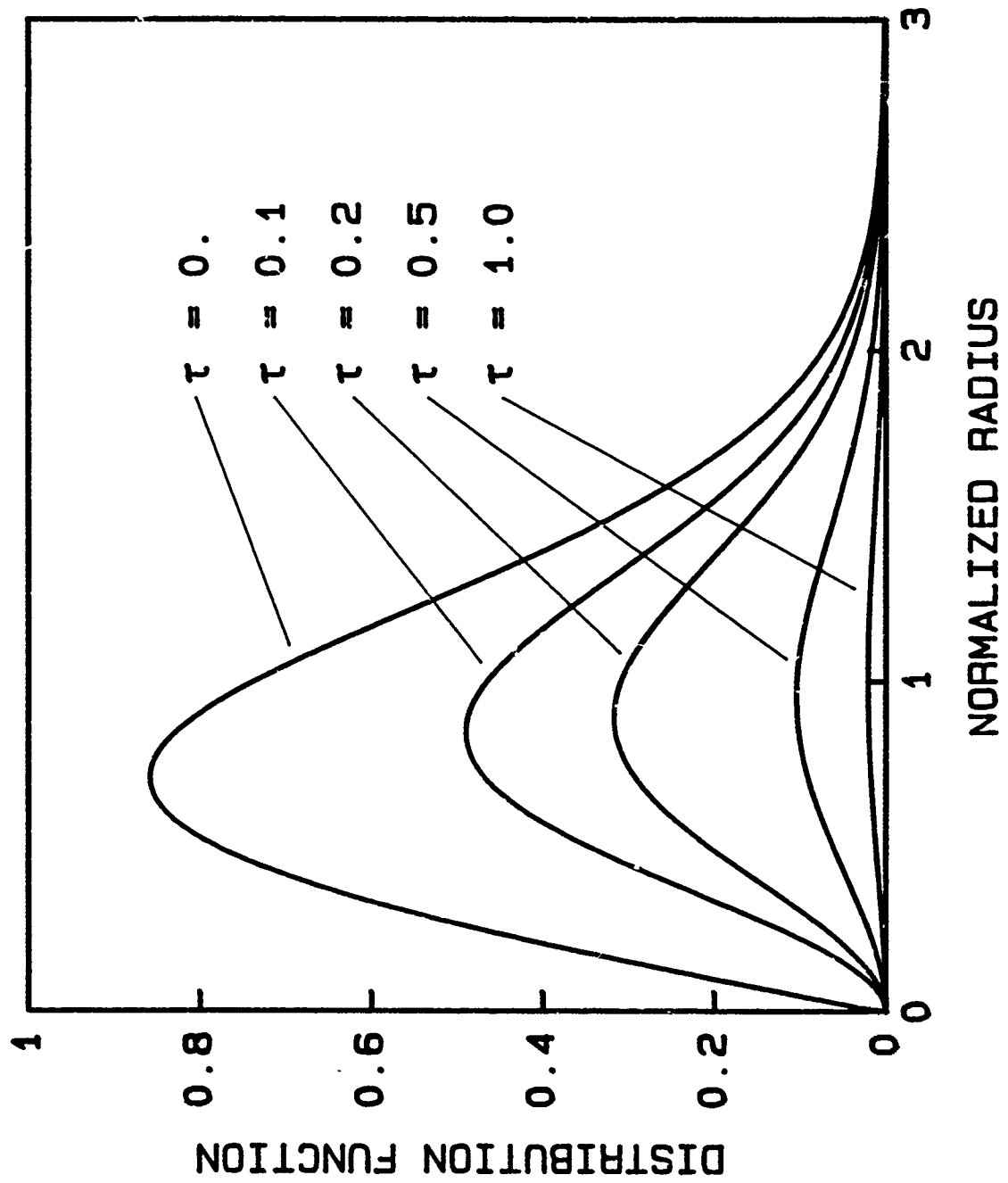


FIGURE 3.

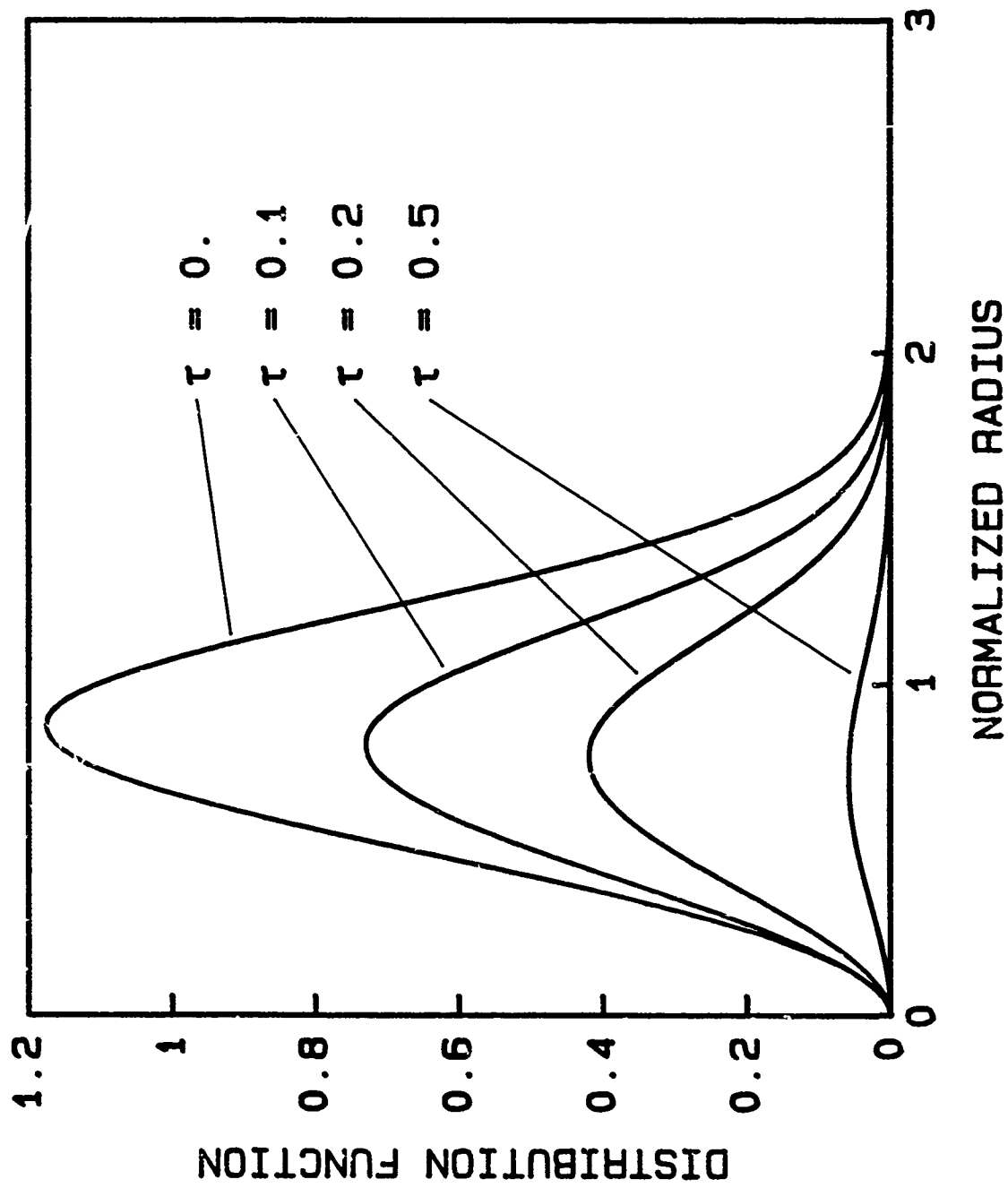
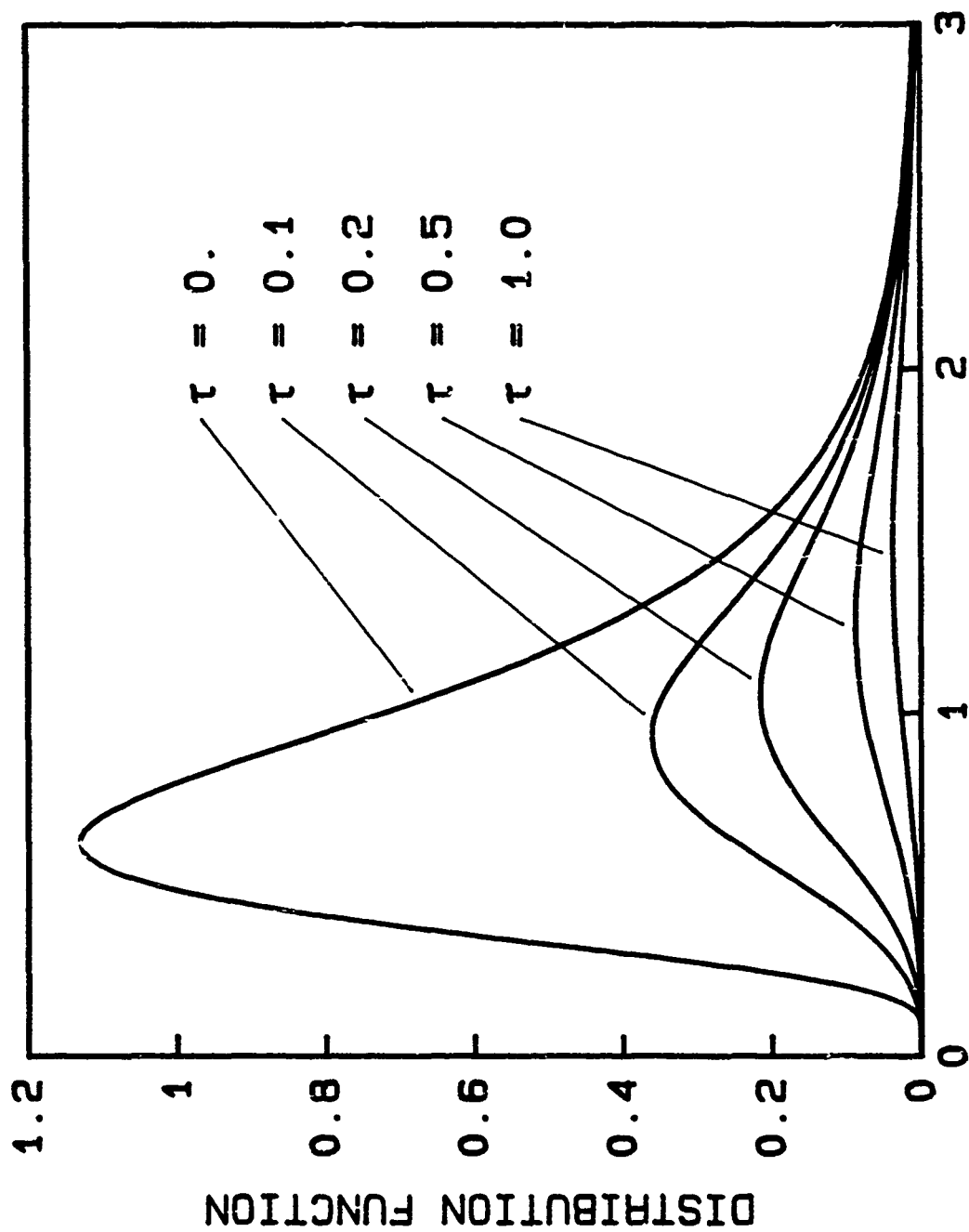


FIGURE 4.



NORMALIZED RADIUS

FIGURE 5.

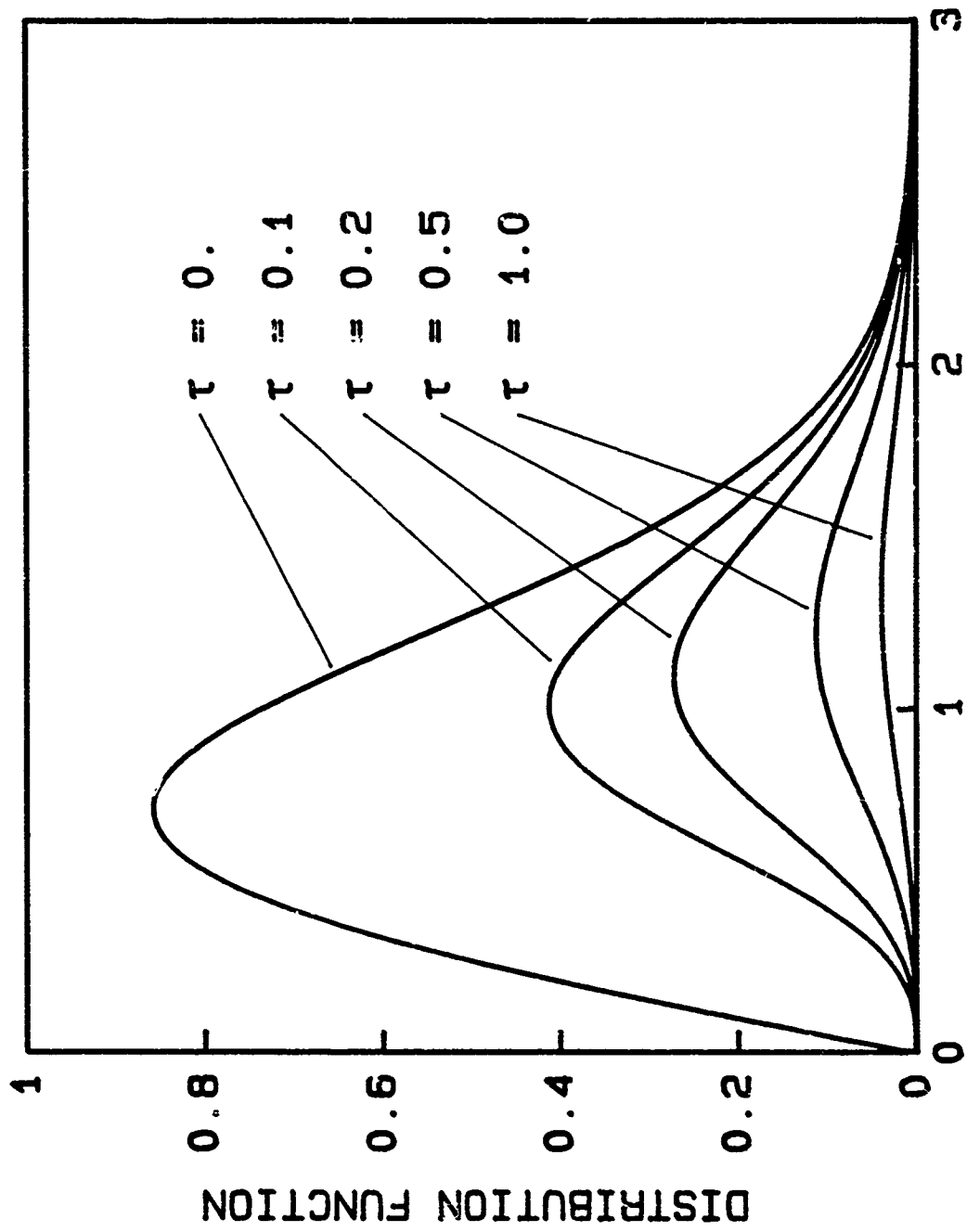


FIGURE 6.

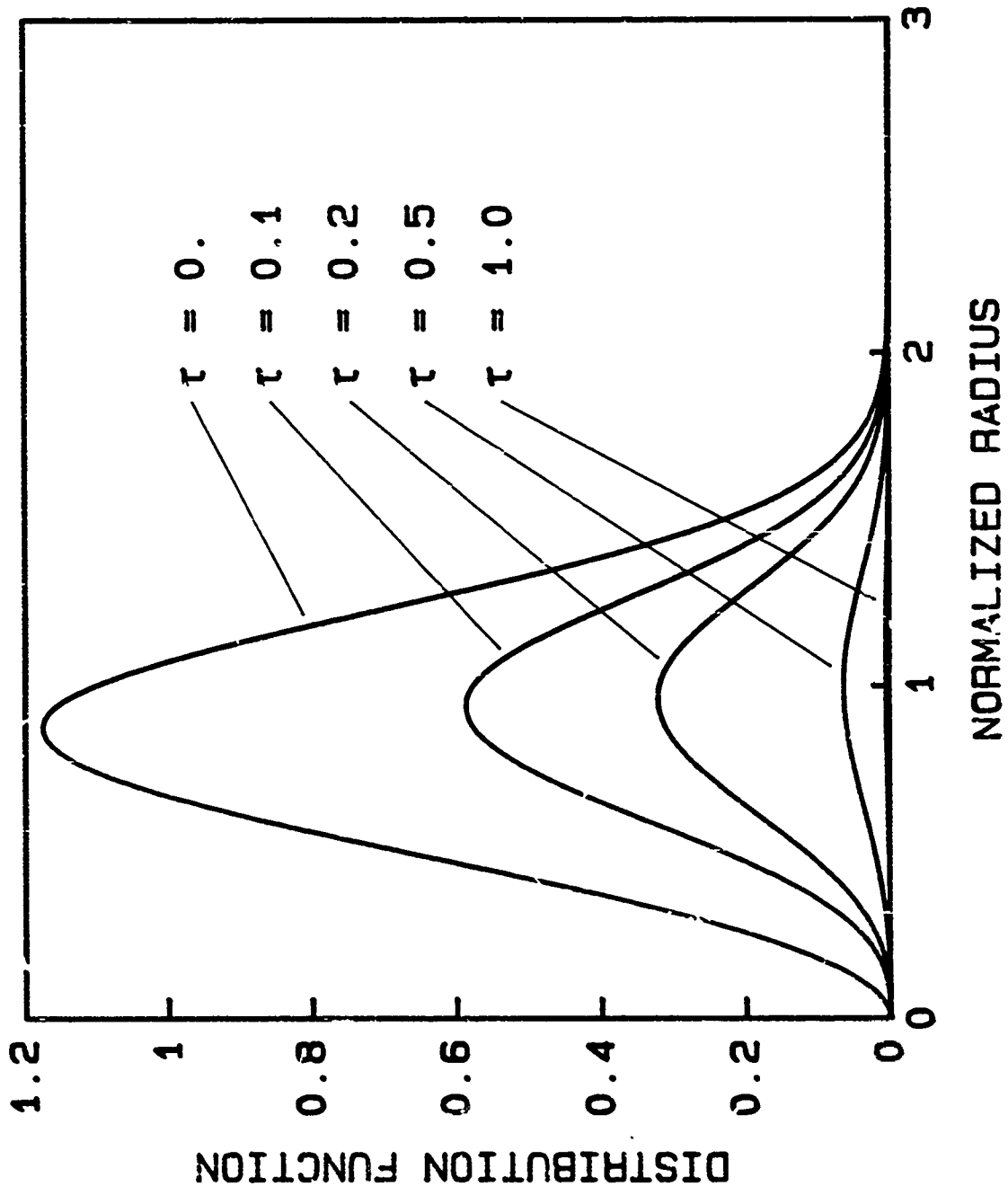


FIGURE 7.

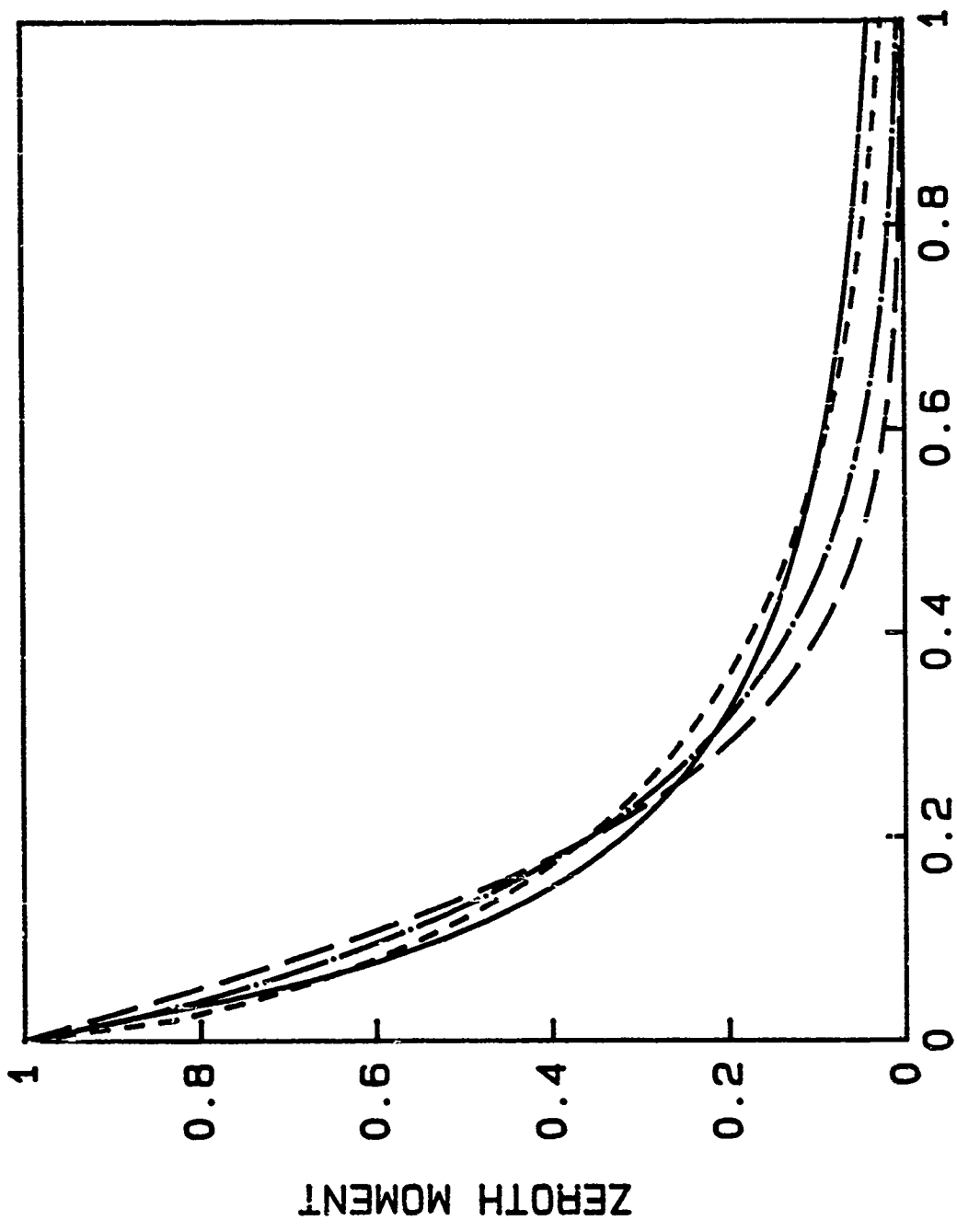


FIGURE 8.

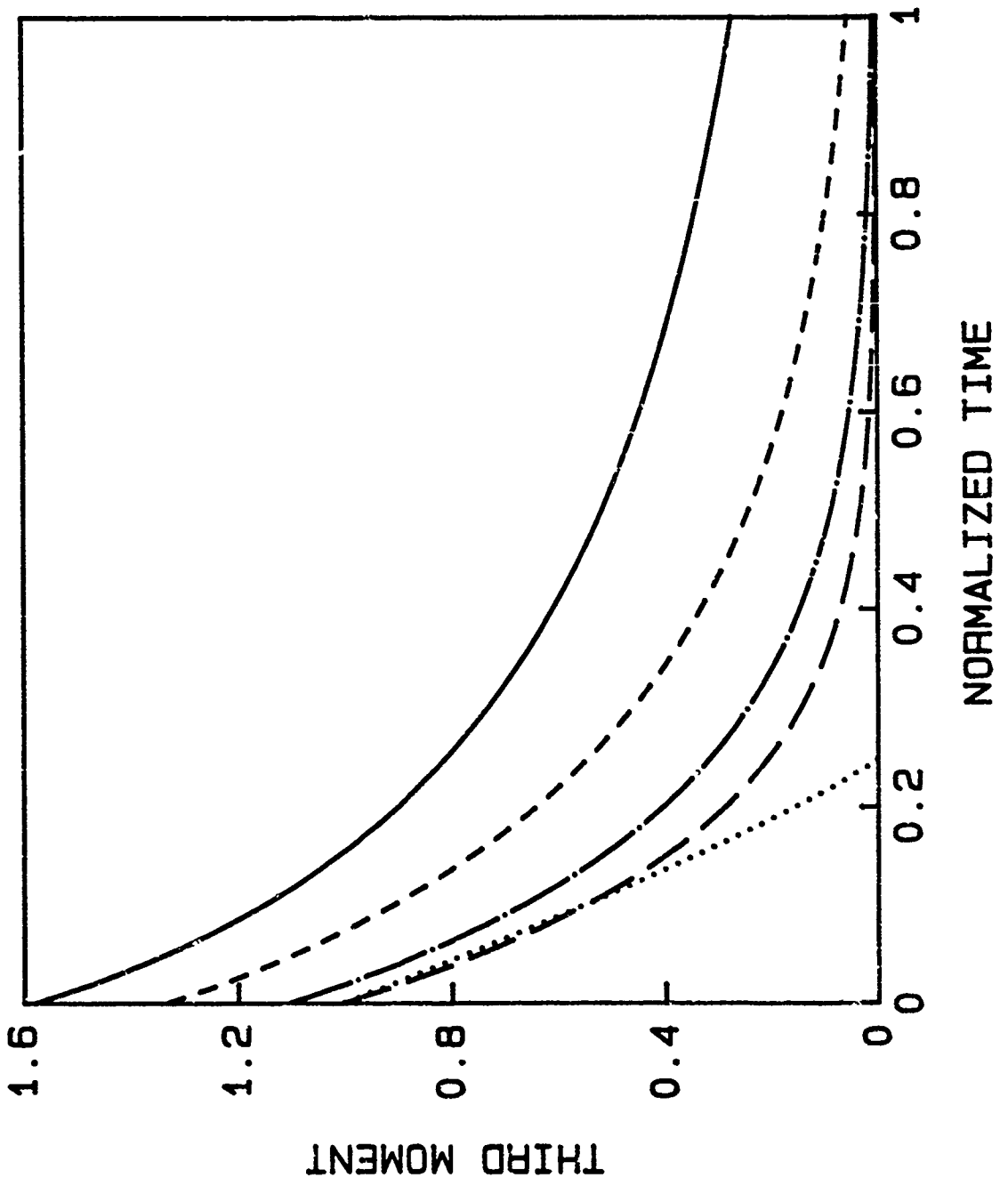


FIGURE 9.

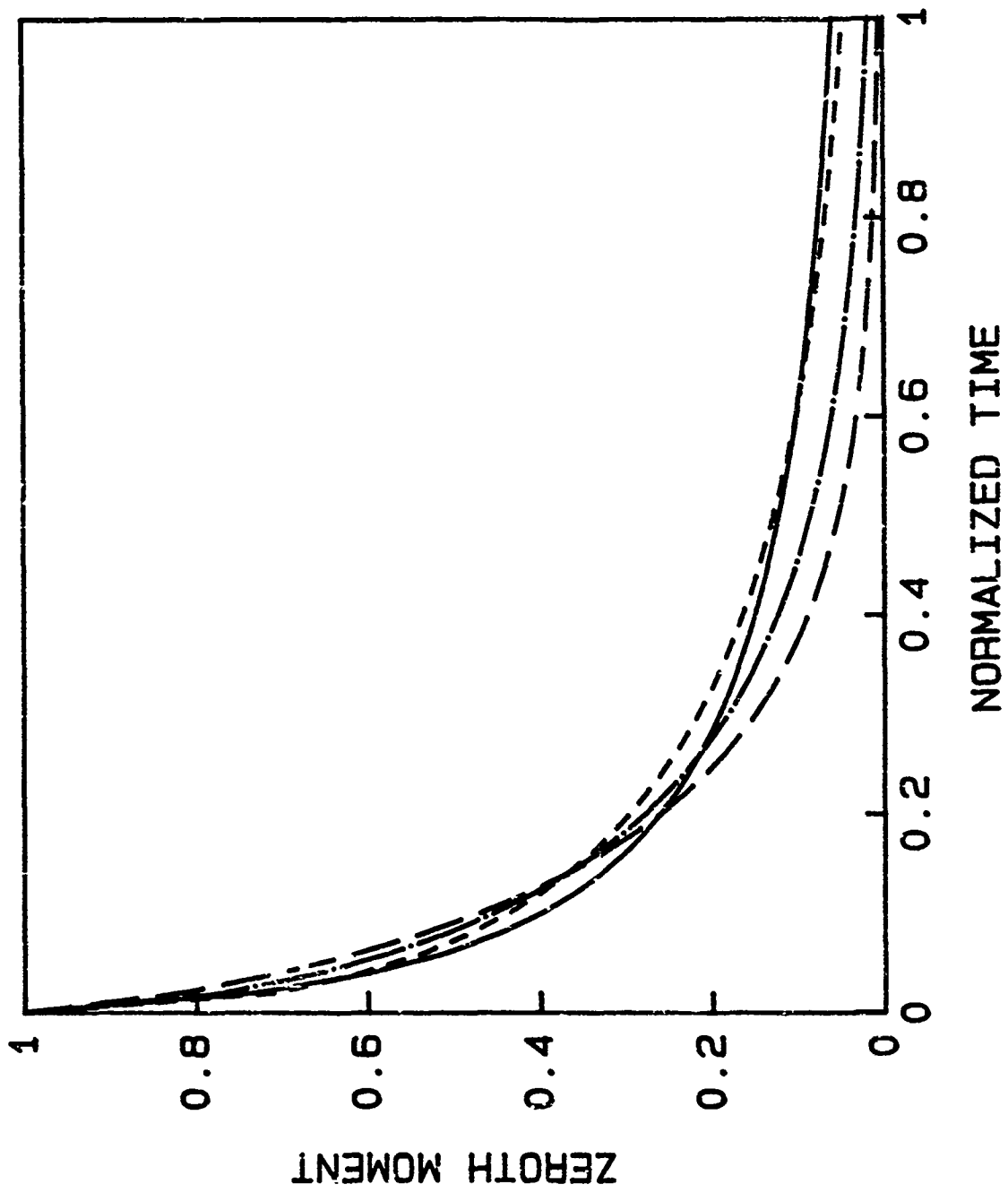
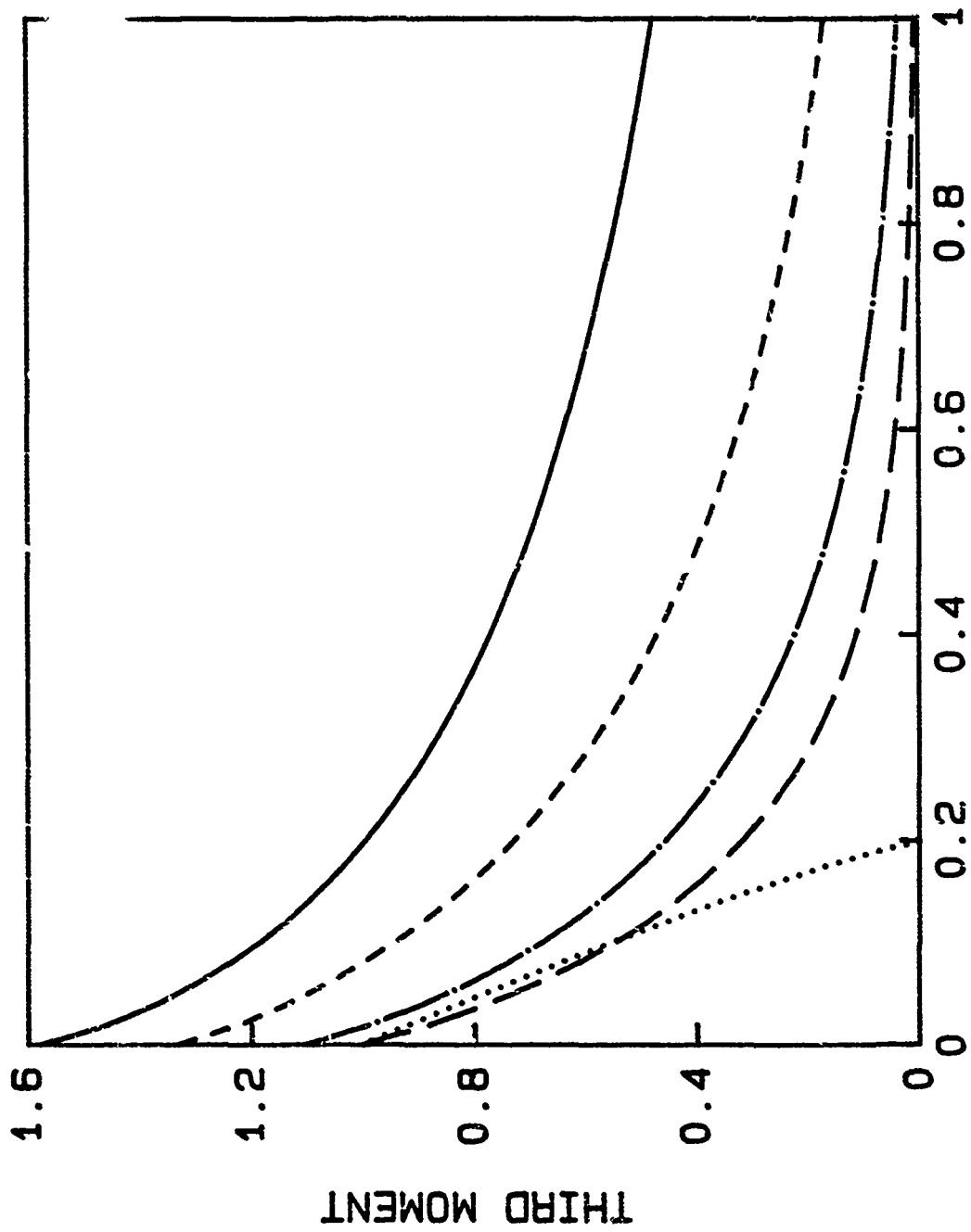


FIGURE 10.



NORMALIZED TIME

FIGURE 11.